Collective Behaviour of Model Microswimmers

Victor B. Putz

Merton College

Department of Physics,
The Rudolph Peierls Centre for Theoretical Physics

University of Oxford

Thesis submitted in partial fulfilment of the requirements for the degree of

Doctor of Philosophy

·Trinity Term 2010·

Collective Behaviour of Model Microswimmers

Victor B. Putz

Merton College

Department of Physics,
The Rudolph Peierls Centre for Theoretical Physics

University of Oxford

Thesis submitted in partial fulfilment of the requirements for the degree of

Doctor of Philosophy

·Trinity Term 2010·

Abstract

At small length scales, low velocities, and high viscosity, the effects of inertia on motion through fluid become insignificant and viscous forces dominate. Microswimmer propulsion, of necessity, is achieved through different means than that achieved by macroscopic organisms. We describe in detail the hydrodynamics of microswimmers consisting of colloidal particles and their interactions. In particular we focus on two-bead swimmers and the effects of asymmetry on collective motion, calculating analytical formulae for time-averaged pair interactions and verifying them with microscopic time-resolved numerical simulation, finding good agreement.

We then examine the long-term effects of a swimmer's passing on a passive tracer particle, finding that the force-free nature of these microswimmers leads to loop-shaped tracer trajectories. Even in the presence of Brownian motion, the loop-shaped structures of these trajectories can be recovered by averaging over a large enough sample size.

Finally, we explore the phenomenon of synchronisation between microswimmers through hydrodynamic interactions, using the method of constraint forces on a force-based swimmer. We find that the hydrodynamic interactions between swimmers can alter the relative phase between them such that phase-locking can occur over the long term, altering their collective motion.

Acknowledgements

I must express my deepest gratitude to my supervisor, Prof. Julia M. Yeomans, for accepting me as a student and providing the right mixture of guidance and freedom to pursue new tools, ideas, and avenues of research.

The soft matter group at Oxford has experienced a great deal of personnel flux during my stay, and it has been my pleasure to work with a wonderful mix of graduate students, postdoctoral researchers, and lecturers. I owe a debt of thanks to Matthew Blow and Ioannis Zacharoudiou, as well as Dr. Gareth Alexander, Dr. Halim Kusumaatmaja, Dr. Chris Pooley, Dr. Scott Edwards, and Dr. Ard A. Louis. In particular, Irwin Zaid and Dr. Jörn Dunkel have provided large numbers of ideas, assistance, support, and stimulating conversation about microswimmers.

Additionally, while it is a poor workman who blames his tools, it seems to be a rare one who thanks them (and their makers). With the exception of the CUDA runtime, all software used in this project was open-source, and I am deeply indebted to those who contributed. This list includes (but is not limited to) Guido Van Rossum for Python, Donald Knuth for TEX, Richard Stallman for Emacs, Andreas Kloeckner for PyCuda, Linus Torvalds for Linux, and the teams who produced gcc, LYX, Inkscape, Scribus, Numpy, Matplotlib, the computer algebra systems SymPy and Maxima, the Emacs plug-in imaxima, and the build system SCons which tied it all together. In a sense, they have all contributed to this research without ever knowing it existed, without me asking, and without remuneration. It is a glorious time for computational science.

I am indebted to my funding agency, the Air Force Institute of Technology. The views expressed in this thesis are those of the author and do not reflect the official policy or position of the United States Air Force, Department of Defense, or the U. S. Government.

Finally, and most importantly, I give deep and heartfelt thanks to my wife Jo; without her support I would never even have had the chance to pursue this research opportunity. She has provided patience, calm, encouragement, and guidance and I will never be able to communicate my appreciation adequately.

Publications

Portions of the work presented in this thesis have appeared in the following peer-reviewed publications:

- Victor B. Putz and J. M. Yeomans. Hydrodynamic Synchronisation of Model Microswimmers. *J. Stat. Phys.*, 137(5):1001-1013, 2009. doi:10.1007/s10955-009-9826-x

- Victor B. Putz, Jörn Dunkel, and Julia M. Yeomans. CUDA simulations of active dumbbell suspensions. To appear in *Chem. Phys.*, 2010. doi:10.1016/j.chemphys.2010.04.025

- Victor B. Putz and Jörn Dunkel. Low Reynolds number hydrodynamics of asymmetric, oscillating dumbbell pairs. To appear in *Eur. Phys. J. Special Topics*, 2010.

- Jörn Dunkel, Victor B. Putz, Irwin M. Zaid and Julia M. Yeomans. Swimmer-tracer scattering at low Reynolds number. *Soft Matter*, 2010. doi:10.1039/c0sm00164c.

Contents

Chapter 1

Introduction

1.1 Collective motion

The great swirls and wheels of a flock of starlings, the ebb and flow of cycle racers in a pack, the jets and eddies of bacteria in suspension–all of these exhibit patterns and behaviours where the motion of the group is more complex than the motion of a single individual, and represent fascinating problems in statistical physics [1].

But how does the complexity and beauty of group motion come about? In [2], Potts describes the motion of avian flocks as analogous to waves propagating from a point source (an initiating individual) at a speed faster than an individual's mean response time, implying that the constituent members of a flock were actively watching for cues and responding to them. This anticipation leads to propagation speeds achieved "in much the same way as they are a human chorus line: individuals observe the approaching manoeuvre wave and time their own execution to coincide with its arrival." Reynolds [3] implemented a model with three rules (separation, alignment, cohesion) which resulted in complex group behaviour of simulated "boids" useful in visual simulation, and Vicsek [4] examined phase transitions in the group motion of particles with similar ad hoc rules.

Figure 1.1: The collective motion of a flock of starlings, though qualitatively different from that of a swarm of bacteria, shows analogous features such as swirls and jets. (a) A flock of starlings over Rome, from [17]. (b) Bacterial turbulence in a sessile drop, from [6].

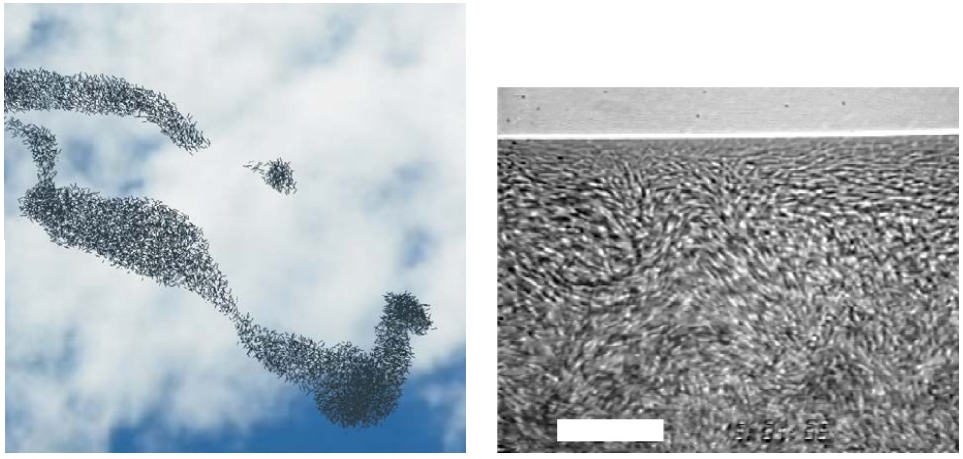

(a) (b)

But Potts' "chorus line" hypothesis for flocks, or ad hoc rules for simulations, can not explain the collective motion observed in bacteria [5, 6] or vibrated masses of rods [7, 8], which show alignment, swirls, and jets not dissimilar to those in flocks of birds. Different biological microswimmers can form bands [9, 10], vortices [11], plumes [12, 13], or other structures [14, 15, 16] when placed in suspensions, yet it is difficult to imagine a simple bacterium watching its neighbors for self-alignment cues, and impossible for an inert rod to do so. In [7], Ginelli et al. show that nematic alignment of polar particles can arise simply from inelastic collisions of rods, leading to complex patterns of banding, but such an explanation seems incomplete for dilute suspensions of self-motile bacteria in fluid.

Where then does the collective motion of microswimmers such as bacteria come from? If not through conscious behaviour, perhaps through simple mechanisms such as chemotaxis [18, 19, 20]–or perhaps through purely physical interaction, using fluid as the medium through which individual motions are communicated. Each tiny swimmer may disrupt its environment in such a way as to slightly rotate and/or translate other swimmers around it, leading to collective motion. By examining how an in-

dividual swimmer changes its geometry to swim, and how those changes may be communicated through the fluid surrounding it to influence the motion of its neighbors, perhaps we can see how collective behaviour can arise through hydrodynamic interaction.

1.2 Low Reynolds number

The motion of an incompressible fluid is governed by the Navier-Stokes equations

$$\nabla \cdot \boldsymbol{v} = 0, \tag{1.1a}$$

$$\rho\left(\frac{\partial \boldsymbol{v}}{\partial t} + \boldsymbol{v} \cdot \nabla \boldsymbol{v}\right) = -\nabla p + \mu \nabla^2 \boldsymbol{v} + \boldsymbol{f}, \tag{1.1b}$$

where ρ is the density of the fluid, $\boldsymbol{v}$ its velocity field, p a pressure field, μ the viscosity of the fluid and $\boldsymbol{f}$ the influence of applied body forces. Eqn. (1.1a) is the mass continuity equation with constant density, a statement of the conservation of volume, while Eqn. (1.1b) describes the relation of fluid velocity to pressures and forces. Each term in (1.1b) has units of force per unit volume. The terms on the left of (1.1b) represent accelerations; $\partial \boldsymbol{v}/\partial t$ is *unsteady* (time-dependent) acceleration, and $\boldsymbol{v} \cdot \nabla \boldsymbol{v}$ is *convective* acceleration such as that produced by steady-state flow through a narrowing pipe, with fluid accelerating as it moves through tighter and tighter constrictions. The terms on the right of (1.1b) represent the effects of any pressure gradient, viscosity, and other body forces on the fluid respectively.

To compare different flows, it is useful to rescale (1.1b) to be nondimensional. Since each term has units of force per unit volume, we can rewrite (1.1b) in terms of some length scale L and speed scale V by multiplying both sides of (1.1b) by $L/\rho V^2$, replacing each term with a nondimensional version ($\boldsymbol{v}' = \boldsymbol{v}/V$, $\nabla' = L\nabla$, etc.) to find

$$\frac{\partial \boldsymbol{v}'}{\partial t'} + \boldsymbol{v}' \cdot \nabla' \boldsymbol{v}' = \nabla' p' + \frac{\mu}{\rho V L} \nabla'^2 \boldsymbol{v}' + \boldsymbol{f}', \tag{1.2}$$

where the coefficient of the nondimensional viscosity term measures the ratio of the inertial terms to the viscous term. The inverse of this coefficient,

$$\mathcal{R} = \frac{\rho V L}{\mu}, \tag{1.3}$$

is termed the Reynolds number, and characterizes the flow such that any two flows with the same Reynolds number are comparable. A 30m blue whale cruising at 50km/h experiences flow with $\mathcal{R} \sim 4 \times 10^8$; it dines on krill moving at $\mathcal{R} \sim 2.5 \times 10^4$, which have been filtering phytoplankton living at $\mathcal{R} \sim 1 \times 10^{-5}$. The two ends of the food chain thus experience very different ratios of inertial versus viscous forces. The swimming mechanisms of the whale rely on inertial components and are very different from those of the phytoplankton, which are dominated by viscosity.

In this thesis, we shall examine the group motion of microswimmers such as bacteria for which the characteristic speed and lengths V and L are both very small, thus leading to low Reynolds number. In the regime of very low Reynolds number, as $\mathcal{R} \to 0$, the viscous components entirely dominate; the inertial terms in (1.1b) may be neglected, and the motion of the fluid is described by the Stokes equations

$$\nabla \cdot \boldsymbol{v} = 0, \tag{1.4a}$$

$$\mu \nabla^2 \boldsymbol{v} - \nabla p + \boldsymbol{f} = 0, \tag{1.4b}$$

where, significantly, the time dependence of the inertial terms has vanished. This lack of explicit time dependence leads to issues of time reversibility and reciprocality in swimming [21], while unique properties of the zero Reynolds number limit lead to long-range effects, both of which contribute to collective swimming behaviour at low $\mathcal{R}$.

1.2.1 Time reversibility and reciprocality

To an outside observer, an isolated swimmer in fluid at rest is *force-free* and *torque-free*, meaning that all forces and torques applied must be internal to the swimmer. As a result, a swimmer can only deform its body, applying forces on the fluid in order to move. But the lack of time dependence in Eqns. (1.4) means that the flow of a fluid is determined only by the fluid's instantaneous state (its velocity and pressure fields plus applied body forces). If a swimmer retraces its path in configuration space under time reversal, it cannot move, as performing the identical series of steps in reverse simply unwinds the motion. Each step, performed backwards, reverses the magnitude of forces applied to the fluid in the forward direction, thus moving it exactly opposite the way it was moved in the forward step.

This fact, noted by Purcell [21] is commonly known as the Scallop Theorem. With only one degree of freedom, the single-hinged scallop can only open and close, thus being obliged to retrace its path in configuration space. As a result, a scallop could not swim at low Reynolds number. This sort of motion, where a swimmer exactly retraces its path in configuration space under time reversal, is termed a *reciprocal* motion.

The Scallop Theorem has a number of ramifications, two of which will be important here. The first, noted above, is that motion of a swimmer (or a *collection* of swimmers, an important distinction) must be nonreciprocal in order to move. The second is that in isolation the speed of the motion is unimportant; the distance a low Reynolds number swimmer moves in a stroke is unchanged whether the stroke is performed slowly or quickly. Only the path in configuration space matters, not how fast it is traversed [22, 23, 24]. Finally, in order that the swimmer move continuously we shall require that it move cyclically in some sort of periodic fashion.

1.2.2 Long-range effects

As the Stokes equations (1.4) are linear for incompressible Newtonian fluids, they can be solved to show that a force $\boldsymbol{f}_\alpha$ applied to a point at location $\boldsymbol{x}_\alpha$ will advect fluid at another location $\boldsymbol{x}_\beta$ as

$$\boldsymbol{v}\left(\boldsymbol{x}_\beta\right) = \mathcal{G}\left(\boldsymbol{x}_\beta - \boldsymbol{x}_\alpha\right)\boldsymbol{f}_\alpha, \tag{1.5}$$

where the Green's function $\mathcal{G}$ is the Oseen tensor [25],

$$\mathcal{G}_{(\alpha i)(\beta j)} \;=\; \frac{1}{8\pi\mu r_{\alpha\beta}}\left(\delta_{ij} + \frac{r_{\alpha\beta i} r_{\alpha\beta j}}{r_{\alpha\beta}^2}\right), \tag{1.6}$$

with α, β denoting the locations, i, j the spatial components of the tensors, and $\boldsymbol{r}_{\alpha\beta} = \boldsymbol{x}_\beta - \boldsymbol{x}_\alpha$ the vector pointing from the location of the applied force $\boldsymbol{f}_\alpha$ to the point $\boldsymbol{x}_\beta$ under consideration. The Oseen tensor is only valid for point sources; in the case of a force applied to a sphere of finite radius a_α advecting another sphere of radius a_β, Rotne and Prager [26] and Yamakawa [27] add a correction

$$\mathcal{G}^1_{(\alpha i)(\beta j)} = \mathcal{G}_{(\alpha i)(\beta j)} + \frac{a_\alpha^2 + a_\beta^2}{24\pi\mu r_{\alpha\beta}^3}\left(\delta_{ij} - 3\frac{r_{\alpha\beta i} r_{\alpha\beta j}}{r_{\alpha\beta}^2}\right), \tag{1.7}$$

making (1.7) the Rotne-Prager-Yamakawa (RPY) tensor. Further corrections are available for multi-particle interactions [28]. For simplicity, our analytics will use only the Oseen tensor (1.6), which is valid when $a_{\alpha,\beta} \ll r_{\alpha\beta}$, the regime discussed in this work. Our simulation programs, for robustness, include the RPY correction (1.7). Note that the Oseen (1.6) velocity field falls off as $1/r$. This is a very long-ranged interaction and means that the effects of an applied force can be felt very far from its origin. For swimmers unaffected by external forces such as gravity, this is mitigated somewhat by the force-free constraint; the swimmer can only apply forces to its environment in opposing pairs. An expansion of the Oseen tensor shows that

if a force-free swimmer produces a net or instantaneous flow, that flow should be no stronger than dipolar, falling off at least as fast as $1/r^2$ [29, 30, 31, 32]. Even so, the incompressible fluid and favorable scaling means that the effects of one swimmer at low Reynolds number can be communicated to other swimmers in the suspension. We shall show that these effects can give rise to collective motion.

1.3 Colloidal model swimmers

The Oseen tensor allows us to describe the motion of a group of colloidal particles with positions $\boldsymbol{x}_\alpha$ and applied forces $\boldsymbol{f}_\beta$ in terms of a symmetric positive definite system hydrodynamic tensor $\boldsymbol{\mathcal{H}}_{\alpha\beta}$ [33], such that

$$\dot{\boldsymbol{x}}_\alpha = \boldsymbol{\mathcal{H}}_{\alpha\beta}\boldsymbol{f}_\beta, \tag{1.8}$$

$\mathcal{H}_{(\alpha i)(\alpha j)} = \delta_{ij}/\left(6\pi\mu a_\alpha\right)$, from the Stokes formula for the velocity of a sphere of radius a_α under the influence of an external force, and $\mathcal{H}_{(\alpha i)(\beta j)}$, $\alpha \neq \beta$ is the Oseen tensor (1.6) or more accurate approximation [28]. This formulation resembles a subset of Stokesian Dynamics [34] without rotation of individual particles or consideration of lubrication forces when particles are in close proximity. The relative simplicity of the model makes it easier to reason analytically about various colloidal model swimmers; once a method of analysis and simulation has been established, it can be applied to multiple models. All that is necessary is the determination of the forces required to move the colloidal particles through the sequence of shapes describing the swimming stroke.

We construct a colloidal model swimmer by positing a collection of spheres which move cyclically in such a way that the swimmer experiences no net force or torque, whether by specifying a series of shape changes or by specifying the forces involved explicitly. This is often easiest to visualize by joining pairs of spheres with links that

expand and contract, moving the spheres in a sequence of shapes that define the swimming stroke.

Fig. 1.2 shows two oft-cited minimal colloidal model swimmers, where a represents a bead radius, ℓ a leg length, and λ, ξ the change in radius or leg length. Fig. 1.2 (a) depicts the three-sphere swimmer of Najafi and Golestanian, which has been widely analyzed [37, 38, 39, 40, 41] and forms the basis of our study of synchronisation between swimmers in Chapter 6. Fig. 1.2 (b) shows Avron's pushmepullyou swimmer [36, 42] which accomplishes locomotion by changing the radii of its constituent colloids. In both cases, the motion of the beads results in propulsion of the swimmer and also flow of the surrounding fluid. This flow field can often be often be described in broad terms as extensile (pushing fluid in the sides and out the ends) or contractile (in from the ends and out the sides), as shown in Fig. 1.3. The flow field produced is tied to the swimmer's geometry and stroke; for example, the three-sphere swimmer can be made to produce a contractile dipolar (varying as $1/r^2$) flow field if $\xi_r < \xi_f$ or an extensile dipolar flow field if $\xi_r > \xi_f$. In the special case where $\xi_r = \xi_f$, there is no dipolar flow field at all and the three-sphere swimmer's net field is then quadrupolar, varying as $(1/r^3)$ [38]; graphic examples of these flow fields are shown in Fig. 5.5.

Other model swimmers have also been discussed. Purcell proposed a swimmer made of three links [21] which could could flap in a nonreciprocal fashion, producing movement. Ishikawa and Pedley analyzed a "squirmer" [43, 44, 45] modeled as a sphere with prescribed tangential surface fluid velocity; similarly, Avron et al. [46] described a swimmer which moved via "surface treadmilling" where surface was generated at the front end and consumed at the rear end. Evans, Spagnolie, and Lauga [47] suggested a bilayer vesicle which changed its shape in order to locomote. Taylor [48] analyzed the motion of an undulating sheet, and Lighthill [49] studied flagellar propulsion and rotating helical filaments.

In this thesis, we restrict our discussion to microswimmers composed of moving

Figure 1.2: Two minimal colloidal swimmers. (a) The "three linked spheres" swimmer described by Najafi and Golestanian [35] and its path in shape space. The two degrees of freedom provided by the independently moving front and back legs provide the nonreciprocal motion necessary for swimming. (b) The two-sphere "pushmepullyou" swimmer described by Avron [36]; the degree of freedom lost by having only one link is replaced by allowing the radii of the spheres to change.

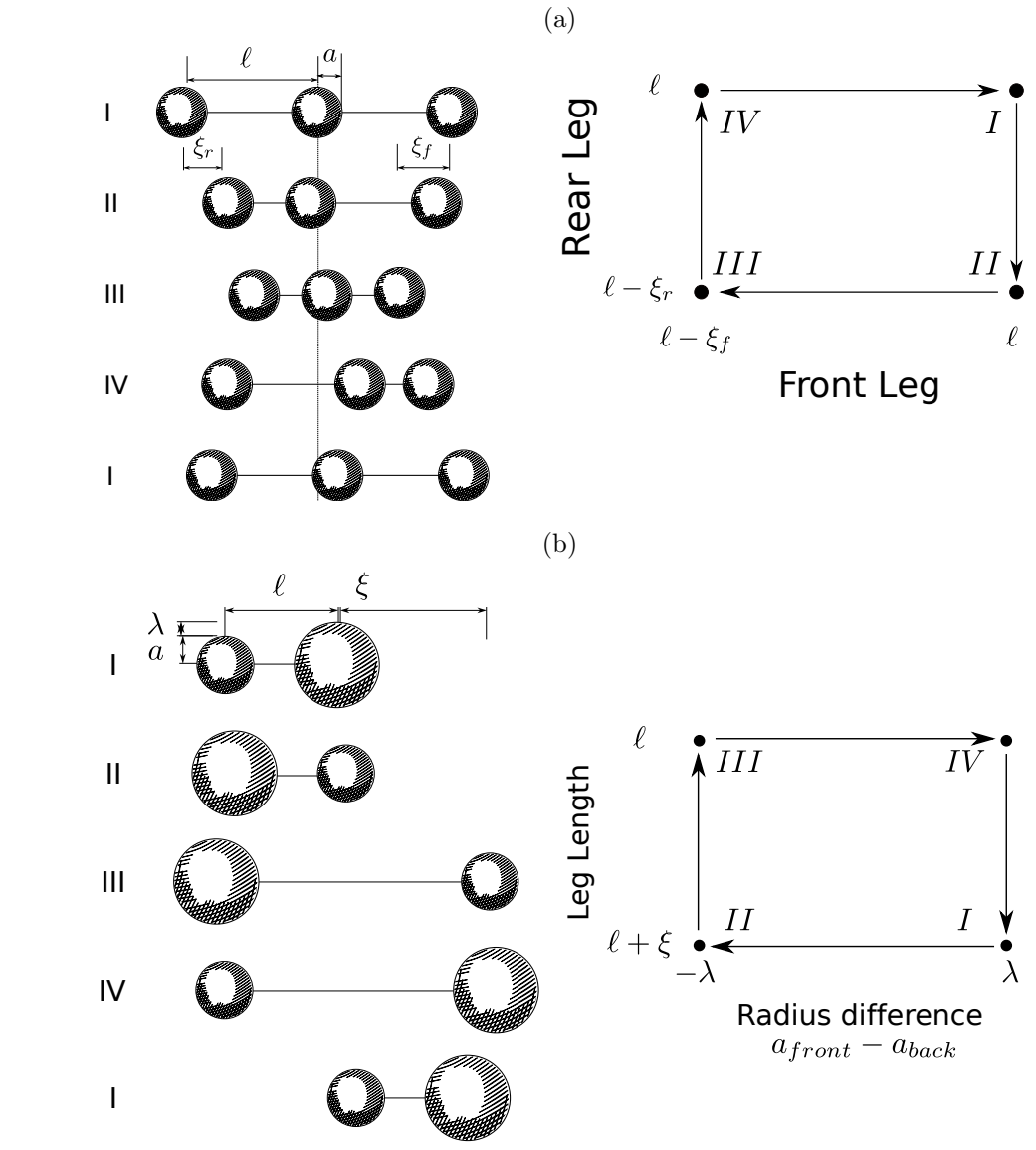

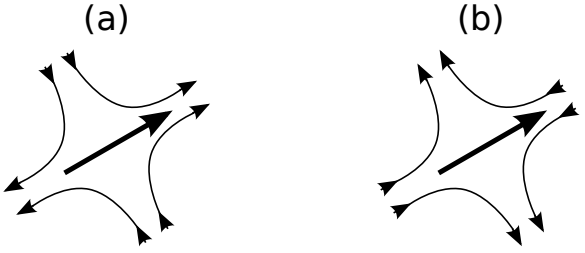

Figure 1.3: (a) Extensile and (b) contractile fluid flows from a model swimmer.

colloidal particles, and compare stroke-averaged analytics with time-resolved simulations. This is distinct from studies of collective motion such as those by Hernandez-Ortiz et al. [30, 50], who simulated large numbers of self-swimming particles as two joined beads with a "phantom flagellum" and having no microscopic stroke at all. A similar construct was used by Baskaran and Marchetti [51]. While these models are very good at allowing large numbers of swimmers in a simulation, it is not obvious when the details of the stroke are important in swimmer interactions, as they are with the three-bead swimmer [38, 40], and when they can be become negligible.

It is of considerable interest that experiments with colloidal particles have resulted in artificial swimmers, both via forced motion of beads [52] or an artificial flagellum actuated by oscillating magnetic fields [53]. Additionally, Kotar et al. [54] have recently demonstrated hydrodynamic synchronisation between colloidal particles held in optical traps, and Tierno et al. [55, 56] have created colloidal dimers which move through fluid when rotated near a surface by external fields, showing a desirable direct link from theory to experiment.

1.4 Thesis outline: a tale of three swimmers

First, in Chapter 2, we examine the simplest model: two identical beads joined by a link which expands and contracts sinusoidally. By the Scallop Theorem, these symmetric dumbbells cannot move individually, but can move as a group. We use a multivariate expansion of the Oseen tensor to extend the results of [57, 58] showing that groups of these swimmers can indeed exhibit collective motion through pair interactions which affect their rotation and translation. We then confirm our stroke-averaged analytics using time-resolved numerical simulation of first swimmer pairs, and then many-swimmer suspensions.

In Chapter 3 we perturb the symmetry of these apolar particles by allowing one

sphere to be larger than the other. Using the same approach as in Chapter 2, we show that the asymmetry causes lower-order terms to appear, making the interactions between dumbbells significantly stronger for comparable parameters.

In Chapter 4 we allow phased variation of the sphere radii, breaking reciprocality within the swimmer and allowing our two-sphere swimmers to move similarly to Avron's pushmepullyou swimmer [36] but with a richness of behaviour which allows the swimmers to move in either direction and to generate extensile or contractile flow fields simply by varying phases. The introduction of net flow introduces more lower-order "passive" terms for swimmer pair interaction which dominate much of swimmer phase space.

We pursue the effects of these passive terms in Chapter 5, where we examine the effects of a swimmer's flow field on an inert tracer particle as the swimmer passes, and return to the active terms (those depending on relative phase) in Chapter 6, where we harness the classical mechanics tool of constraint forces to examine the effects of hydrodynamics on synchronisation between swimmers.

Chapter 2

Collective motion of symmetric dumbbells

2.1 Motivation

If we are to explain the collective behaviour of a suspension of swimmers which propel themselves by quasi-periodic swimming mechanisms [59, 21], one significant task is the approximation of the explicit time-dependent microscopic dynamics with a set of coarse-grained time-averaged equations of motion. However, while the simplified time-averaged equations are valuable, techniques used for simplification often involve severe approximations, and it is not always clear how qualitatively accurate the resultant equations are. To this end, we pursue a detailed comparison between the microscopic dynamics of actively-driven, spring-based dumbbells and those of a time-averaged analytic model derived from far-field expansions similar to those discussed in [57, 58]. We continue this theme in the following chapters, addressing the effects of asymmetry on interactions as well as the introduction of self-swimming and net flow. For now, we restrict the discussion to purely symmetric dumbbells.

Because dumbbells cannot swim or generate flow by themselves due to their re-

ciprocal motion [21], they constitute an excellent model for examining the active components of collective swimming at zero Reynolds number, $\mathcal{R} = 0$, and thus have come under examination by several authors [57, 58, 51]. Any effective motion in deterministic dumbbell systems must only be caused by hydrodynamic interactions between dumbbells.

In a recent paper, Alexander and Yeomans [58] derived analytical expressions for effective far-field interactions of symmetric active dumbbells in three dimensions, showing that the effective hydrodynamic pair interaction decays with distance $|\boldsymbol{D}|$ as $|\boldsymbol{D}|^{-4}$ where $\boldsymbol{D}$ is the vector between dumbbells' centres. While these studies have led to insights into interplay between the symmetry and the scaling of the effective long-distance interaction, a detailed comparison of microscopic and stroke-averaged models was still lacking.

To explore this, we derive time-averaged equations of motion for pair interactions of symmetric dumbbells, then verify them against microscopic time-resolved numerical simulations, finding good agreement. After verifying the accuracy and applicability of the time-averaged pair interactions, we then compare analytics to simulations of 3-D arrays of symmetric dumbbells. Again, we find that the stroke-averaged dynamics equations yield a relatively accurate description of the microscopic model down to distances of only a few times the dumbbells' length, remarkable in view of the fact that the stroke-averaged model is based on a far-field expansion.

2.2 Model

We consider a system of S identical dumbbells consisting of two spheres with radius a as shown in Fig. 2.2. At very low $\mathcal{R}$, inertia is negligible and the state of the system at any time t is completely described by the positions of the spheres $\{X_\alpha\} = \{X_{(\alpha i)}(t)\}$, where $\alpha = 1, \ldots, 2S$ labeling spheres and $i = 1, 2, 3$ the spatial dimension (adopting

Figure 2.1: A symmetric dumbbell, with only one degree of freedom: expansion and contraction along its length. By the Scallop Theorem, a lone dumbbell cannot swim, but multiple dumbbells can exhibit collective motion.

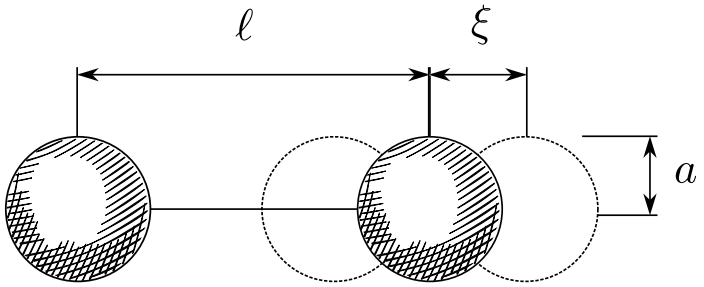

$$L(t) = \ell + \xi \sin(\omega t + \phi)$$

the Einstein summation convention for repeated lower Latin indices).

Neglecting rotation of the spheres, the dynamics is governed by the Ito-Langevin equations [60, 61, 62, 63]

$$\begin{aligned} \dot{X}_{(\alpha i)} = & \sum_{\beta} \mathcal{H}_{(\alpha i)(\beta j)} F_{(\beta j)} + \\ & \sum_{\beta} \left(k_B \mathcal{T}\right)^{1/2} \mathcal{C}_{(\alpha i)(\beta k)} \zeta_{(\beta k)}\left(t\right), \end{aligned} \tag{2.1}$$

where k_B denotes the Boltzmann constant and $\mathcal{T}$ the temperature of the surrounding fluid ($\dot{X} = \mathrm{d}X/\mathrm{d}t$). $\mathcal{H}_{(\alpha i)(\beta j)}$ is the system hydrodynamic interaction tensor (1.8), and $\mathcal{C}_{(\alpha i)(\beta k)}$ is the Cholesky decomposition of $\mathcal{H}_{(\alpha i)(\beta j)}$. Equation (2.1) corresponds to the overdamped limit of Stokesian dynamics [34]. For this discussion we disregard the second line of (2.1) and examine the case of purely deterministic swimming, reintroducing noise in Chapter 5.

To completely specify the model, we must define the internal time-resolved forces applied to the beads. To this end, consider the dumbbell σ formed by spheres $\alpha = 2\sigma$

and $\beta = 2\sigma + 1$, and denote its length by

$$d^{\sigma}(t) := |\boldsymbol{X}_{\beta}(t) - \boldsymbol{X}_{\alpha}(t)|. \tag{2.2}$$

In the analytic stroke-averaged case, we can calculate the internal forces for an isolated swimmer directly. For the numeric simulations, however, we shall assume the two spheres are connected by a harmonic spring of variable length $L^{\sigma}(t)$, thus $F^{\sigma}_{(\beta i)} = -\partial_{(\beta i)} U^{\sigma}$, where

$$U^{\sigma}(t, d^{\sigma}) = \frac{k_0}{2}\left[d^{\sigma} - L^{\sigma}(t)\right]^2, \tag{2.3}$$

with $L^{\sigma}(t) = \ell + \xi \sin(\omega t + \phi^{\sigma})$ denoting the time-dependent equilibrium spring length, and ℓ the mean length such that $\ell > 2a + \xi$. If $\xi = 0$, the dumbbell is called *passive*, while if $|\xi| > 0$ it is termed *active*. The phase parameter ϕ^{σ} becomes significant for the interactions between two or more dumbbells.

For this overdamped description (2.1) to remain valid, the dumbbell must be driven sufficiently slowly; more precisely, we must impose the relation between time scales such that $T_{\gamma} \ll T_D \ll T$, where $T := 2\pi/\omega$ is the driving period, $T_D := 2\pi/\sqrt{k_0/M}$ the oscillator period for a sphere of mass M, and $T_{\gamma} := M/\gamma$ the characteristic damping time. In this limit, the dumbbells behave similarly to shape-driven swimmers, i.e., $d^{\sigma} \simeq L^{\sigma}(t)$ is a useful approximation in analytical calculations. Additionally, imposing these time constraints (in particular, choosing a good value for k_0 and ω) becomes important in the stability of the numerical integration of the equations of motion.

2.3 Analysis

As discussed in Subsection 1.2.1, low $\mathcal{R}$ swimmers with one degree of freedom can only exhibit reciprocal motion, and so a single isolated dumbbell is subject to the Scallop Theorem and cannot swim. However, two or more dumbbells, out of phase, constitute a system which traces a closed but nonreciprocal path in configuration space and can thus exhibit group motion through hydrodynamic interactions [57, 58]. We now turn to the task of analytically calculating pair interactions between dumbbells.

To do this, we shall use the dumbbells' changing shapes to determine the relative positions of their spheres with respect to their centres, and the time-varying forces applied to each. With this information, we can use an expansion of the Oseen tensor to calculate induced velocities at the position of a target dumbbell's spheres at each point during a period of oscillation. Integrating over a full cycle and dividing by the period, we find time-averaged equations of motion for these pair interactions.

2.3.1 General stroke-averaging procedure

For an arbitrary suspension of S microswimmers, we can view the rotation and translation of each microswimmer as the sum of one-body, two-body, ...S-body contributions, where "one-body" refers to the ability of each swimmer to translate or rotate in isolation. In the case of symmetric dumbbells, there are no one-body contributions, and we turn instead to the two-body contributions.

To examine the effect on some "target" dumbbell σ from an arbitrary "source" dumbbell ρ, we denote the position of the spheres of dumbbell ρ by $\boldsymbol{X}_s^\rho$, $s = 1, 2$. We

then introduce centre-of-mass and relative coordinates by

$$\boldsymbol{R}^{\rho} = \frac{1}{2}\left(\boldsymbol{X}_1^{\rho} + \boldsymbol{X}_2^{\rho}\right), \tag{2.4a}$$

$$\boldsymbol{S}^{\rho} = \boldsymbol{X}_2^{\rho} - \boldsymbol{X}_1^{\rho}, \tag{2.4b}$$

$$\hat{\boldsymbol{N}}^{\rho} = \left(\boldsymbol{X}_2^{\rho} - \boldsymbol{X}_1^{\rho}\right) / \left|\boldsymbol{X}_2^{\rho} - \boldsymbol{X}_1^{\rho}\right|, \tag{2.4c}$$

where $\boldsymbol{R}^{\rho}$ represents the *geometric centre* of the dumbbell and $\hat{\boldsymbol{N}}^{\rho}$ its *unit orientation vector*. Thus $\boldsymbol{S}^{\rho} = L^{\rho}(t)\,\hat{\boldsymbol{N}}^{\rho}$, and given the geometric centre of a dumbbell, we calculate the position of its spheres as

$$\boldsymbol{X}_1^{\rho} = \boldsymbol{R}^{\rho} + h_1^{\rho}(t)\,\hat{\boldsymbol{N}}^{\rho}, \quad \boldsymbol{X}_2^{\rho} = \boldsymbol{R}^{\rho} + h_2^{\rho}(t)\,\hat{\boldsymbol{N}}^{\rho}, \tag{2.5}$$

where the scalar displacements $h_{1,2}^{\rho} = \mp L^{\rho}(t)/2$ are the symmetric variations of the beads' positions about the swimmer's geometric centre. The force-free constraint on dumbbell ρ can be written as

$$F_1^{\rho} = -F_2^{\rho} = f^{\rho}, \tag{2.6}$$

where F_s^{ρ} denotes the internal forces acting on the first and second sphere during a swimming stroke. That force is always directed along $\hat{\boldsymbol{N}}^{\rho}$ and in isolation moves the two ends of the dumbbell as

$$\frac{\mathrm{d}}{\mathrm{dt}}\boldsymbol{X}_1^{\rho} = f^{\rho}\left(\frac{1}{6\pi a\mu} - \frac{2\kappa}{L^{\rho}(t)}\right)\hat{\boldsymbol{N}}^{\rho}, \tag{2.7a}$$

$$\frac{\mathrm{d}}{\mathrm{dt}}\boldsymbol{X}_2^{\rho} = -f^{\rho}\left(\frac{1}{6\pi a\mu} - \frac{2\kappa}{L^{\rho}(t)}\right)\hat{\boldsymbol{N}}^{\rho}, \tag{2.7b}$$

where $\kappa = (8\pi\mu)^{-1}$. This takes into account the Stokes velocity of each sphere due to its applied force as well as the Oseen approximation for the velocity contribution at that sphere's location produced by the opposing force applied at the opposite end

of the dumbbell. Knowing L^ρ, we can solve for the time-varying force

$$f^\rho = -\frac{6\pi a\mu\omega\cos\left(\phi^\rho+\omega t\right)\xi\left(\sin\left(\phi^\rho+\omega t\right)\xi+\ell\right)}{2\sin\left(\phi^\rho+\omega t\right)\xi+2\ell-3a}. \tag{2.8}$$

Now knowing the time-varying position of the dumbbell's spheres, and the time-varying force applied to the spheres during their travel, we are positioned to use a double expansion of the Oseen tensor to determine the motion of the ends of dumbbell σ caused by the swimming stroke of dumbbell ρ.

2.3.2 A double expansion of the Oseen tensor

In the dilute limit, where the positions of dumbbells σ and ρ are separated by a vector connecting their centres

$$\boldsymbol{D}^{\sigma\rho} := \boldsymbol{R}^\sigma - \boldsymbol{R}^\rho, \tag{2.9a}$$

$$\hat{\boldsymbol{D}}^{\sigma\rho} := \boldsymbol{D}^{\sigma\rho}/\left|\boldsymbol{D}^{\sigma\rho}\right| \tag{2.9b}$$

such that $\ell \ll |D|$, we can view the effects of force f^ρ at sphere position $\boldsymbol{X}_n^\rho$ advecting the fluid at position $\boldsymbol{X}_m^\sigma$ (where $m, n = 1, 2$) as a double expansion of the Oseen tensor about both endpoints, using scalar displacements along the lengths of $\hat{\boldsymbol{N}}^\sigma$ and $\hat{\boldsymbol{N}}^\rho$ as parameters for the expansion, as shown in Fig. 2.2.

To do this, we replace $r_{\alpha\beta}$ in the Oseen tensor (line 1 of (1.6)) with $r_{\alpha\beta} \to d^{\sigma\rho}\hat{\boldsymbol{D}}^{\sigma\rho} + h^\sigma\hat{\boldsymbol{N}}^\sigma - h^\rho\hat{\boldsymbol{N}}^\rho$, leaving the expression in terms of the scalar displacements $d^{\sigma\rho}, h^\sigma, h^\rho$ and the unit vectors $\hat{\boldsymbol{D}}^{\sigma\rho}, \hat{\boldsymbol{N}}^\sigma, \hat{\boldsymbol{N}}^\rho$; the resulting expressions will thus be in terms of these quantities as well as the projections

$$\hat{\boldsymbol{N}}^\rho\hat{\boldsymbol{D}}^{\sigma\rho} := r, \quad \hat{\boldsymbol{N}}^\sigma\hat{\boldsymbol{D}}^{\sigma\rho} := s, \quad \hat{\boldsymbol{N}}^\sigma\hat{\boldsymbol{N}}^\rho := q. \tag{2.10}$$

Knowing that the force f on the spheres of dumbbell ρ will always be applied along

Figure 2.2: The geometry of the two-dumbbell interaction problem. For the Oseen expansion to be valid, $|D^{\sigma\rho}|$ must be much greater than dumbbell length ℓ, allowing expansion of the Oseen tensor about small perturbations along each swimmer's orientation vector.

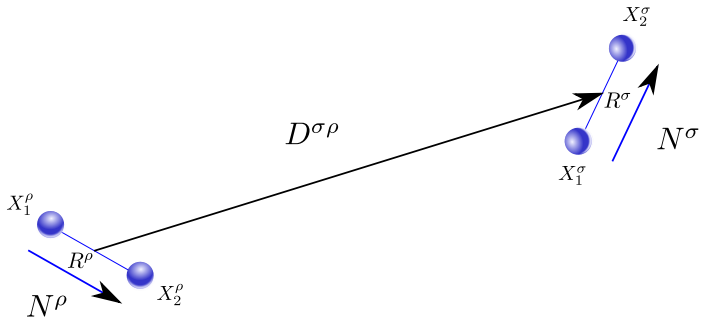

the direction vector $\hat{\boldsymbol{N}}^\rho$, we multiply and contract to give the velocity at sphere m of dumbbell σ, produced by force f on sphere n of dumbbell ρ, as

$$
\begin{aligned}
u(\boldsymbol{X}_m^\sigma) &= f\mathcal{H}_{mn}^{\sigma\rho} \\
&= \frac{f}{8\pi\mu} \times \\
&\quad \Big\{ \hat{\boldsymbol{N}}^\rho \left((d^{\sigma\rho})^2 + 2sh_m^\sigma d^{\sigma\rho} - 3rh_n^\rho d^{\sigma\rho} + (h_m^\sigma)^2 - 3qh_m^\sigma h_n^\rho + 2\,(h_m^\sigma)^2 \right) \\
&\quad + d^{\sigma\rho}\hat{\boldsymbol{D}}^{\sigma\rho} \left(rd^{\sigma\rho} + qh_m^\sigma - h_n^\rho \right) + h_m^\sigma \hat{\boldsymbol{N}}^\sigma \left(rd^{\sigma\rho} + qh_m^\sigma - h_n^\rho \right) \Big\} \\
&\quad / \left((d^{\sigma\rho})^2 + 2sh_m^\sigma d^{\sigma\rho} - 2rh_n^\rho d^{\sigma\rho} - (h_m^\sigma)^2 - 2qh_m^\sigma h_n^\rho + (h_n^\rho)^2 \right)^{3/2}, \quad (2.11)
\end{aligned}
$$

where h_m^σ and h_n^ρ are the displacements of spheres m and n along the dumbbell orientation vectors $\hat{\boldsymbol{N}}^\sigma$ and $\hat{\boldsymbol{N}}^\rho$ respectively. Eqn. (2.11) is a complex expression to treat analytically, but it is very useful here because the scalar displacements $h_{m,n}^{\sigma,\rho}$ about the endpoints of the displacement vector are small with respect to $|\boldsymbol{D}|$, lending (2.11) to Taylor expansion about $h_{m,n}^{\sigma,\rho} = 0$. The first several terms of this expansion are given in Appendix A.

We can use (2.11) to obtain tensor expressions $\mathcal{H}_{mn}^{\sigma\rho}$ for each of the four bead-bead

interactions between the two swimmers, giving expressions for $\frac{\mathrm{d}}{\mathrm{dt}}\boldsymbol{X}_{1,2}^{\sigma}$,

$$\frac{\mathrm{d}}{\mathrm{dt}}\boldsymbol{X}_{1}^{\sigma} = \mathcal{H}_{11}^{\sigma\rho} f - \mathcal{H}_{12}^{\sigma\rho} f, \tag{2.12a}$$

$$\frac{\mathrm{d}}{\mathrm{dt}}\boldsymbol{X}_{2}^{\sigma} = \mathcal{H}_{21}^{\sigma\rho} f - \mathcal{H}_{22}^{\sigma\rho} f, \tag{2.12b}$$

where the terms $\mathcal{H}_{mn}^{\sigma\rho} f$ can be interpreted as the velocity produced by force f applied to sphere n of swimmer ρ at the position of sphere m of swimmer σ.

Using (2.4a) and (2.4c) the translation and rotation of dumbbell σ can be written as

$$\frac{\mathrm{d}}{\mathrm{dt}}\boldsymbol{R}^{\sigma} = \frac{f}{2}\left(\mathcal{H}_{11}^{\sigma\rho} - \mathcal{H}_{12}^{\sigma\rho} + \mathcal{H}_{21}^{\sigma\rho} - \mathcal{H}_{22}^{\sigma\rho}\right), \tag{2.13a}$$

$$\frac{\mathrm{d}}{\mathrm{dt}}\hat{\boldsymbol{N}}^{\sigma} = \frac{f}{\ell^{\sigma}}\left(\mathcal{H}_{21}^{\sigma\rho} - \mathcal{H}_{22}^{\sigma\rho} - \mathcal{H}_{11}^{\sigma\rho} + \mathcal{H}_{12}^{\sigma\rho}\right). \tag{2.13b}$$

Each tensor expression can be expanded about the scalar displacements $h_{m,n}^{\sigma,\rho}$ and the resulting expression simplified. Next, we substitute the time-varying bead displacements $h_{1,2}^{\sigma,\rho}$ from (2.5) and applied forces from (2.8). The resulting expression is then simplified by expansion in powers of small parameters such as a/ℓ and ξ/ℓ until it is in an easily integrable form. We next integrate t over a full period and divide by a period to time-average, simplifying again if necessary by expansion in powers of small parameters. Details of derivation of the translation term for symmetric dumbbells can be found in Appendix B as an example of the process. We find, for symmetric dumbbells, effective equations of motion of the form

$$\dot{R}_{i}^{\sigma} = \sum_{\rho\neq\sigma} J_{i}^{\sigma\rho}, \tag{2.14}$$

$$\dot{\hat{N}}_{i}^{\sigma} = -\left(\delta_{ik} - \hat{N}_{i}^{\sigma}\hat{N}_{k}^{\sigma}\right)\sum_{\rho\neq\sigma} K_{k}^{\sigma\rho}, \tag{2.15}$$

where the projector $\left(\delta_{ik} - \hat{N}_i^\sigma \hat{N}_k^\sigma\right)$ is in place to remove changes parallel to $\hat{\boldsymbol{N}}^\sigma$. The stroke-averaged hydrodynamic interaction terms to leading order in ξ/ℓ are given by

$$\begin{aligned} J_i^{\sigma\rho} =& a\omega \sin\left(\phi^\sigma - \phi^\rho\right) \frac{9}{64} \left(\frac{\xi}{\ell}\right)^2 \left(\frac{\ell}{|D^{\sigma\rho}|}\right)^4 \times \\ & \left\{\hat{N}_i^\sigma \left(2s + 4qr - 10sr^2\right)\right. \\ & \left. + \hat{D}_i^{\sigma\rho} \left(1 + 2q^2 - 5s^2 - 5r^2 - 20qsr + 35s^2r^2\right)\right\}, \end{aligned} \tag{2.16}$$

$$\begin{aligned} K_k^{\sigma\rho} =& \omega \sin\left(\phi^\sigma - \phi^\rho\right) \frac{15}{64} \left(\frac{a}{\ell}\right) \left(\frac{\xi}{\ell}\right)^2 \left(\frac{\ell}{|D^{\sigma\rho}|}\right)^5 \times \\ & \hat{D}_k^{\sigma\rho} \left(3s + 6rq + 6sq^2 - 7s^3 - 21sr^2 - 42qs^2r + 63s^3r^2\right). \end{aligned} \tag{2.17}$$

One readily observes the following prominent features: (i) the effective translational interactions scale as $|\boldsymbol{D}^{\sigma\rho}|^{-4}$; (ii) the effective rotational interactions scale as $|\boldsymbol{D}^{\sigma\rho}|^{-5}$, (iii) the stroke-averaged interaction terms J, K vanish if the phases ϕ^σ and ϕ^ρ differ by multiples of π [58]. This illustrates the importance of phase (de)tuning in the collective swimming at zero $\mathcal{R}$.

2.4 Simulation

Verifying such analytics against numerical simulation poses several challenges. A number of techniques for simulation of microswimmers have been suggested, such as using Lattice-Boltzmann [64, 65, 66], Stochastic Rotation Dynamics [64, 67], or Smooth Particle Hydrodynamics [68] to simulate the fluid, with swimmers providing boundary conditions. This is effective, but the assumptions necessary for our analytics require large separations between particles and swimmers. These models are more computationally intensive in that regime, as they must model a large amount of liquid for a comparatively small number of swimmers.

It is also possible to simulate only the interactions between colloidal particles [64,

34, 69], and we favor this approach here. Earl et al. [64] advocate a method which calculates swimming motion purely based on shape changes, but we found this method became unusable with large numbers of swimmers and could not iterate to a solution. We instead calculate required forces by means of variable-length harmonic springs and construct the hydrodynamic interaction tensor from the particles' locations. The velocities can then be calculated directly via (1.8).

Since hydrodynamic interactions are long-ranged, simulations of full time-resolved dynamics of $S = N/2$ dumbbells (each consisting of two spheres) scale as $\mathcal{O}(N^2)$ using a straightforward algorithm. While the scaling is unfortunate, the dynamics is well-suited to parallel computation, and recent innovations in Graphics Processing Units (GPUs) allow tremendous speedups (up to hundreds of times) for many problems versus a CPU-only solution [70, 71, 72, 73]. We thus implement a straightforward $\mathcal{O}(N^2)$ solution of the equations of motion, achieving a speedup of greater than a hundredfold compared with CPU-only code and making simulation of suspensions feasible. This allows us to explore the effects of spacing and density on these suspensions.

Most $\mathcal{O}(N^2)$ problems such as these N-body simulations with pair interactions involve enough data communication that they are difficult to distribute efficiently or are costly enough that they must be recast into more numerically tractable forms such as Ewald summation [74, 34, 75, 76, 77, 78, 79, 69]. For cases of a few hundred swimmers, CUDA-based implementations of straightforward $\mathcal{O}(N^2)$ problems present an excellent method for numerical simulation.

Our algorithm is a simplified form of Stokesian Dynamics [34], as we neglect lubrication and rotation of individual spheres. Each iteration of the algorithm runs in an ordered series of steps:

1. The current positions of the spheres are used to calculate a vector of forces based on the time-varying dumbbell lengths and spring parameters (2.3). Since the forces are always applied in opposing pairs, the force-free nature of the

swimmers is preserved.

2. A large system interaction matrix $\mathcal{H}$ is calculated for each bead-bead interaction, with entries defined as in Section 1.3. While the analytics are based on the Oseen approximation, the simulations use the Rotne-Prager-Yamakawa correction, which is more accurate at close separations of beads. The suspensions examined here are dilute enough that the two are approximately equal.

3. The interaction matrix is multiplied by the applied force vector, resulting in a vector of velocities.

4. The velocities are then scaled by the time step according to the active integration method, and the simulation proceeds.

Each step in an iteration can be subject to multiple variations, so it is possible to, for example, apply external forces or model different swimmers simply by replacing or extending the software objects used in step 1, or to run multiple cases with additive noise by modifying the tensor calculation used in step 2 and using a different integrator. The parts of the computational pipeline are assembled at runtime, giving a great amount of flexibility without writing customized code for every possibility. Since the forces are determined at each timestep and the strokes of the swimmers are resolved at a very fine level, the implementation is a microscopic time-resolved simulation, completely separate from the analytics, making it a good comparison.

However, the computational time is dominated by step 2, where the $\mathcal{O}(N^2)$ calculation of the interaction matrix $\mathcal{H}$ consumes the most processor time. As the interactions between dumbbells are extremely weak, and the time scales demanded by stiff springs very small, the simulations must be run for many timesteps to achieve measurable results, so speed of computation becomes a paramount concern.

CUDA (Compute Unified Device Architecture) is a proprietary technology by Nvidia corporation which allows parallel numerical simulations to be run on consumer-

level graphics processing units (GPUs). Though still a relatively new technology at the time of this writing, it has been shown that GPU algorithms may yield significant speedups (up to factors of a few hundreds) whenever a problem can be naturally parallelized [70, 71, 72, 73], on relatively low-cost consumer-grade hardware. In cases where the problem is small enough to fit on a single device, the resulting software is simpler, easier to test, less costly to implement, and much faster than that written using traditional cluster-based methods. This is the case for deterministic many-swimmer simulations, for stochastic single-swimmer simulations, and also for stochastic many-swimmer simulations with purely additive noise, corresponding to a constant matrix $\mathcal{C}$ in (2.1). A more open standard, OpenCL, is approaching, but is still relatively untested and thus was not used for these studies.

Initial testing of a similar but simpler problem (colloids moving under constant applied force, using Oseen interactions and single precision) showed very large benchmarked speed-ups compared with a C-based CPU simulation. For example, with ~ 2000 particles, we measured up to a $\sim 450\times$ speed-up when calculating the full hydrodynamic interaction tensor and $\sim 800\times$ speed-up using an un-optimized version of the elegant tiled method described in [80] as shown in Fig. 2.3. We did not benchmark the current simulation, but estimate the speed-up, while still being significant, to be considerably less due to the complexity of the multi-swimmer problem, additional data transfers from the GPU, and the use of double precision.

Despite the speed advantage of the tiled method, we decided to compute the full hydrodynamic interaction tensor in our simulations, primarily to maintain congruence with existing C code in a battery of automated unit tests and to keep the code as simple as possible. Future implementations will likely reintroduce the tiled calculation to further improve computational efficiency. Generally, it is encouraging that even a relatively straightforward CUDA simulation of the multi-swimmer problem exhibits compelling speed advantages over a CPU-based solution.

Figure 2.3: Performance of a simple Oseen-tensor sedimentation simulation showing simulation frames per second versus number of particles in the simulation. (a) Traditional single-CPU methods (Python and C) immediately show N^2 scaling; both CUDA-based methods (calculating the full tensor or using the tiled method in [80]) show much-improved performance, reaching N^2 scaling only as the simulation approaches several hundred particles. (b) Use of the tiled method versus calculation of the full hydrodynamic interaction tensor shows a noticeable speedup with fluctuating performance depending on number of particles and subdivision of the problem into computing units.

(a)

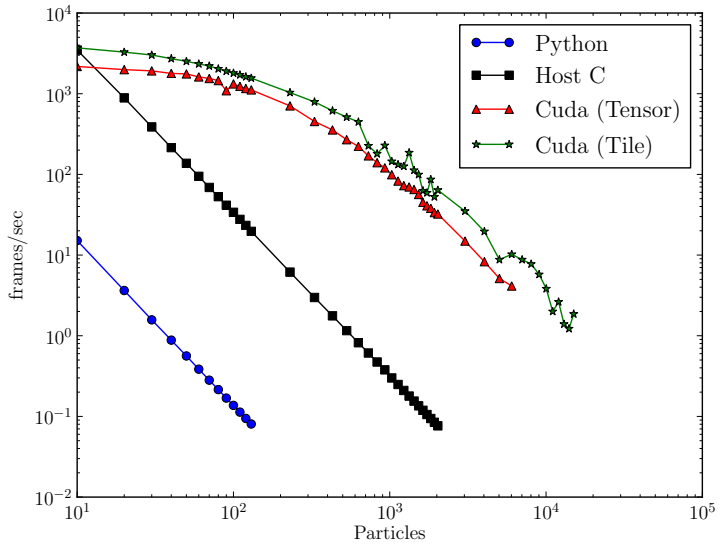

(b)

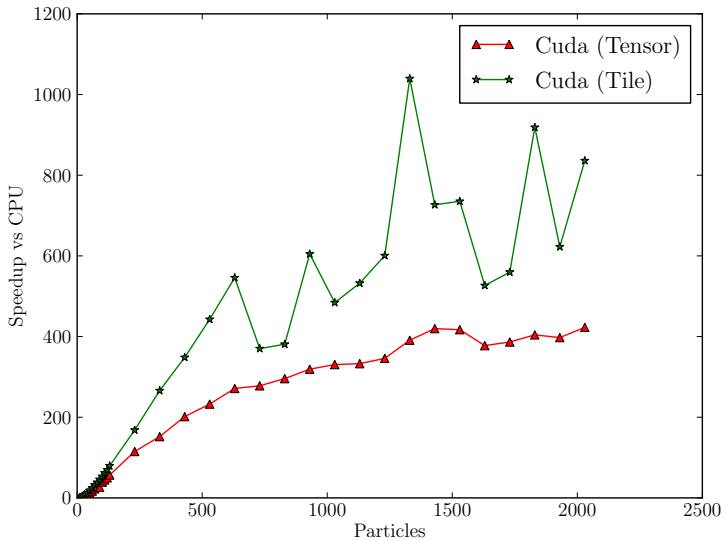

The use of double precision is unfortunate in that single precision calculations on CUDA processors show significant performance increases due to better hardware support and memory considerations. However, in the case of collective dumbbell motion, the distance moved in each time-step is very small compared to the length of the dumbbells or their position, which caused initial calculations using single precision to fail, as the position increment during a single timestep fell below the threshold of machine precision. To allow for standardized testing, we elected to use double precision and to accept decreased performance rather than implementing a better accumulation algorithm (such as Kahan summation) based on single precision. For reasons of accuracy, we also chose not to enable Nvidia's fast-math optimizations. The latter can significantly accelerate the computation of certain numeric functions (particularly trigonometric functions) but this gain comes at the cost of some precision. However, this might represent another opportunity for performance optimization in the future.

Another important issue is the choice of the integrator due to accumulation of errors and the stiffness of the problem. A variety of methods were tested, including Euler [81, 82], Adams-Bashforth-Moulton [81, 83, 84], and Runge-Kutta [85, 86, 87, 88] integrators. The approach eventually used was a one-step Heun predictor-corrector method [82], which produced satisfactory results compared to analytically tractable test cases and can easily incorporate additive noise for stochastic simulations. The time step for the simulations was chosen based on the smallest dynamical time scale in the problem (given by the spring frequency $T_0 = 2\pi/\sqrt{k_0/M}$, see discussion in Section 2.2) and then manually reduced until numerical errors were acceptable by ensuring that single dumbbells did not translate and numeric fluctuations were orders of magnitude below the expected motion caused due to hydrodynamic interactions. The choice of integrator in related simulations became increasingly important as asymmetry was added; see Section 3.2.

The use of a spring-based model created an additional complication: After pre-

scribing the initial positions, orientations, and phases of the dumbbells, we initially placed the spheres centred at the potential minima. However, numerical integration and finite potential strengths caused the sphere positions to lag very slightly behind the potentials once they began moving periodically. Since the hydrodynamically induced dumbbell motion is very small compared to the dumbbell size, this initial settling caused a large anomalous motion during the first period of simulation. To rectify this, it was necessary to discard the first period and begin measurements after the lag was established and dumbbell translation was approximately linear. This did cause miniscule deviations of the dumbbells' mean length ℓ, amplitude ξ, and phase ϕ from the values specified by the initial conditions, but tuning the potential spring constant to be sufficiently stiff reduced these deviations to acceptable values of a few percent.

While the results shown here are purely deterministic, incorporating noise is relatively straightforward, as the system hydrodynamic tensor $\mathcal{H}$ may be numerically decomposed via Cholesky decomposition [89, 90]. However, even with GPU acceleration this decomposition is prohibitively expensive; in the case of slender dumbbells and dilute suspensions, we advocate a simple additive noise with a constant matrix $\mathcal{C}$ as a reasonable approximation in the dilute limit, as the off-diagonal terms in (1.8) are negligible. We compared the full Cholesky decomposition and an additive-noise approximation in various test runs and found that the results for the collective mean square displacement differed by only a few percent.

2.5 Testing dumbbell pair interactions

To compare the analytic solutions (2.14)-(2.15) with simulations, we first consider the translational motion of aligned dumbbell pairs similar to those studied by Lauga and Bartolo [57], then examine rotational interaction of dumbbell pairs at various

orientations. Finally, we study the collective motion of 3D grids of dumbbells. In all cases, the swimmers are assumed to be in an infinite body of fluid initially at rest, i.e. no additional boundary conditions, periodic or otherwise, are imposed.

2.5.1 Aligned dumbbell pairs

So long as thermal fluctuations are negligible, aligned dumbbells do not change their orientation, and (2.14) reduces to

$$\dot{\boldsymbol{R}}^{\sigma} = \frac{9}{16} a\omega \sum_{\rho \neq \sigma} \sin\left(\phi^{\sigma} - \phi^{\rho}\right) \left(\frac{\xi}{\ell}\right)^{2} \left(\frac{\ell}{|\boldsymbol{D}^{\sigma\rho}|}\right)^{4} \hat{\boldsymbol{D}}^{\sigma\rho}, \tag{2.18}$$

where $\boldsymbol{R}^{\sigma}$ and $\boldsymbol{D}^{\sigma\rho}$ are vectors along a common axis. The lines in Figs. 2.4 (a) and 2.4 (b) represent the dynamics of aligned dumbbell pairs as predicted by (2.18). Symbols were obtained from microscopic simulations of the corresponding spring-based model described in Section 2.2. Following Lauga and Bartolo [57], we quantify collective motion of the dumbbell pairs in terms of their mean collective displacement (solid lines/filled symbols in Fig. 2.4),

$$\overline{R^{21}}\left(t\right) = \frac{1}{2}\left[R^{2}\left(t\right) + R^{1}\left(t\right)\right], \tag{2.19}$$

and their mean relative distance (dashed lines/unfilled symbols in Fig. 2.4),

$$\Delta R^{21}\left(t\right) = R^{2}\left(t\right) - R^{1}\left(t\right). \tag{2.20}$$

The quantity $\overline{R^{21}}\left(t\right)$ characterizes the net motion of the dumbbell pair, whereas $\Delta R^{21}\left(t\right)$ indicates whether the dumbbells move towards or away from each other.

As is evident with Fig. 2.4 (a), symmetric dumbbells move in the same direction with identical speeds; the direction of the motion is determined by the phase difference $\phi^{2} - \phi^{1}$. As predicted by (2.18), the collective displacement over a swimming stroke

varies as $|D^{\sigma\rho}|^{-4}$ with the distance between the dumbbells, as shown in Fig. 2.4 (b). Even though the stroke-averaged equations (2.18) are based on a far-field expansion, they describe the microscopic dynamics of aligned dumbbells well down to distances of only a few body lengths.

While the stroke-averaged equations are relatively insensitive to the expansion parameter $\ell/|D^{\sigma\rho}|$, it is worthwhile to note that the quantitative difference between the stroke-averaged dynamics (solid lines) and microscopic simulations (symbols) in Figs. 2.4 (a) and 2.4 (b) is due to the relatively large parameter ratio $a/\ell = 0.2$ used in these simulations. To make Eqns. (2.14) and (2.15) more tractable, the formulae were taken to only leading order in a/ℓ and thus become more accurate in the limit $a/\ell \to 0$. This is confirmed by the numerical results shown in Fig. 2.4 (c), which depicts the ratio of the average collective swimming speeds (i.e. the collective displacements after a stroke period) obtained by either method for different values of a/ℓ at constant stroke amplitude ξ. We readily observe that this ratio approaches unity in the limit $a/\ell \to 0$. However, in view of the fact that the collective swimming speed is approximately proportional to the sphere radius a (see (2.18)), we opted for a moderate value $a/\ell = 0.2$ in our simulations in order to better observe noticeable swimming effects.

2.5.2 Two-dimensional rotation of dumbbell pairs

Dumbbells arranged in aligned 1D configurations as in Subsection 2.5.1 do not change their orientation. For non-aligned configurations where the dumbbells are free to move in three dimensions, hydrodynamic pair interactions can induce rotations. To test the accuracy of the stroke-averaged equation (2.15) for rotational motion, we conducted a series of simulations with two dumbbells.

The first dumbbell (labelled by ρ) was placed at the origin oriented along the x-axis, and a second dumbbell (σ) was placed such that the geometric centres were

Figure 2.4: Comparison of exact microscopic motion and effective stroke-averaged dynamics for an aligned dumbbell pair. Lines were obtained by numerical integration of the stroke-averaged equation (2.18) whereas symbols show the simulation results for the microscopic spring-based dumbbell model described in Section 2.2. Solid lines/filled symbols depict the mean displacement $\overline{R^{21}}(t) - \overline{R^{21}}(0) = \{[R^2(t) + R^1(t)] - [R^2(0) - R^1(0)]\}/2$ of the geometric centres. Dashed lines/unfilled symbols indicate the change in relative separation $\Delta R^{21}(t) - \Delta R^{21}(0) = [R^2(t) - R^1(t)] - [R^2(0) - R^1(0)]$. (a) Symmetric dumbbells do not change their relative separation and move linearly in time depending on the phase difference $\Delta\phi = \phi^2 - \phi^1$. Simulation parameters are comparable to those of Lauga and Bartolo [57]: initial separation $\Delta R^{21}(0) = R^2(0) - R^1(0) = 10\ell$, mean dumbbell length $\ell = 5\mu$m, driving frequency $\omega = 500\text{s}^{-1}$ (time on the x-axis is given in units of the stroke period $T = 2\pi/\omega$), stroke amplitude $\xi = 0.1\ell$, $a = 0.2\ell$, phase difference $\phi^2 - \phi^1 = \pi/2$. For the microscopic model: spring constants $k_0 = 0.001\text{kg/s}^2$, viscosity $\mu = 10^{-3}\text{kg/(ms)}$, particle mass density $\varrho = 10^3\text{kg/m}^3$, simulation time step $\Delta t \approx 10^{-4}T$. (b) Distance dependence of the collective motion and separation for aligned dumbbell pairs during a stroke period T. Line styles and symbols correspond to the same configurations and simulation parameters as used in (a). Remarkably, the stroke-averaged far-field equation (2.18) describes the microscopic dumbbell dynamics well down to distances of a few body lengths; however, the deviations from the time-resolved microscopic dynamics accumulate over time, as evident from (a). The difference between the stroke-averaged dynamics (solid lines) and microscopic simulations (symbols) in (a) and (b) is largely due to the choice of a relatively large parameter ratio $a/\ell = 0.2$ in these simulations; the results of both methods agree in the limit $a/l \to 0$ as illustrated in diagram (c), which shows the ratio of mean swimmer displacements obtained from the microscopic (Mic) and stroke-averaged (SA) dynamics at constant $\xi = 0.1\ell$ and various choices of a/ℓ.

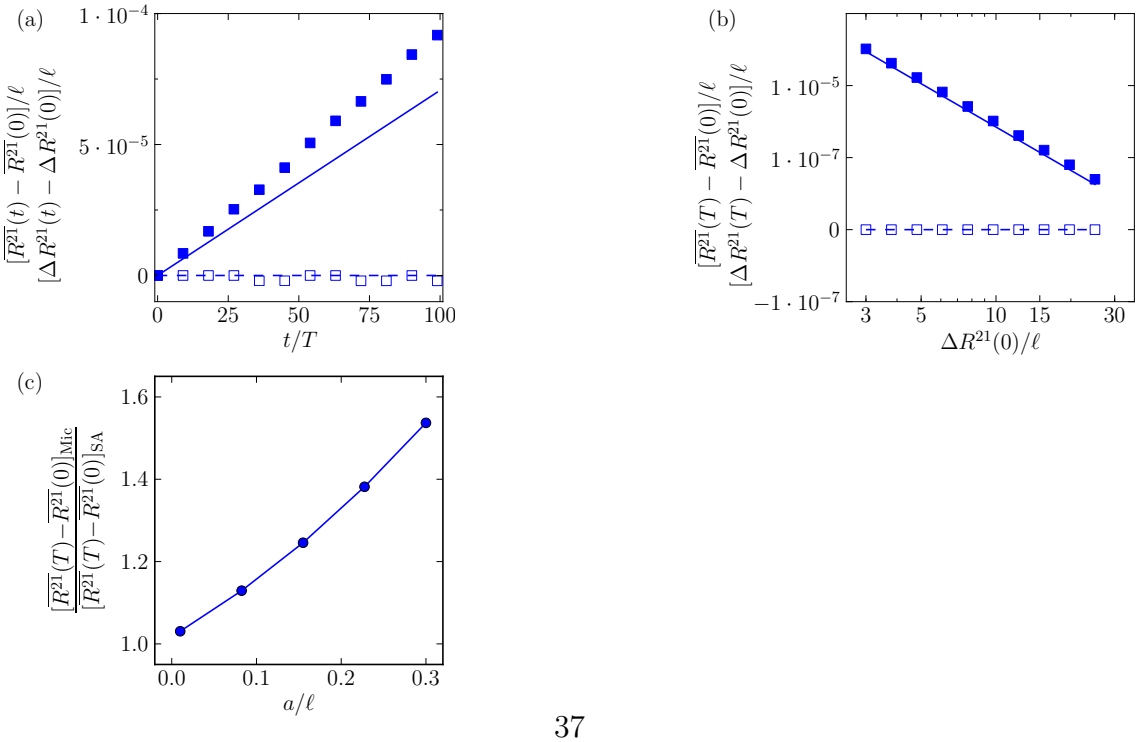

separated by a distance of 5ℓ. By varying the starting position of the second dumbbell around a circle while keeping the initial projection constant, we compared numeric and analytic results for various projections $s(t)$, $r(t)$, $q(t)$ as defined in (2.10).

Fig. 2.5 depicts the change of the dumbbells' relative orientation

$$\Delta q(t) := q(t) - q(0), \qquad q(t) := N_j^{\sigma}(t) N_j^{\rho}(t) \tag{2.21}$$

after five swimming strokes ($t = 5T$) for two different initial projections (Fig. 2.5 (a), $q(0) = 0$, and Fig. 2.5 (b), $q(0) = 1$). As evident from the diagrams, in both cases the stroke-averaged description (2.15) correctly reproduces the rotational dynamics of the microscopic spring-based model.

The good agreement between the stroke averaged equations and simulations corroborates that stroke-averaged equations of the form (2.14)-(2.17) can provide a convenient mesoscopic description which could be used as, for example, a starting point for derivation of coarse-grained macroscopic field theories [51]. Conversely, the good agreement between the averaged dynamics and the microscopic simulation provides a helpful confirmation that our CUDA algorithm works correctly even at relatively low densities when hydrodynamic interaction effects are relatively weak and algorithms may become prone to numerical instabilities. With these concerns satisfied, we focus on 3D many-swimmer simulations.

2.6 Three-dimensional dumbbell arrays

We now compare the predictions of the stroke-averaged far-field equations with simulations of spring-based dumbbells in larger-scale, 3D dumbbell configurations.

In our simulations, the dumbbells' geometric centres $\boldsymbol{R}^{\sigma}(0)$ were initially placed on a cubic lattice with equidistant spacing $\rho^{-1/3}$, where ρ is the number density of the configuration. Initial orientations $\hat{\boldsymbol{N}}^{\sigma}(0)$ were sampled uniformly from the unit

Figure 2.5: Rotational motion of dumbbell pairs; symbols indicate numerical data, while lines represent analytics. $\theta_{\hat{D}}$ is the angle between a line connecting the dumbbells' geometric centres and the $x-$axis; $\Delta q\,(5T) = q\,(5T) - q\,(0)$ where $q\,(t)$ is the projection of the swimmer orientations $q\,(t) = N_j^1\,(t)\,N_j^2\,(t)$. Initial configurations: (a) $q\,(0) = 0$ and (b) $q(0) = 1$ with an initial radial separation of 5ℓ; one readily observes good agreement between microscopic simulations and the analytics.

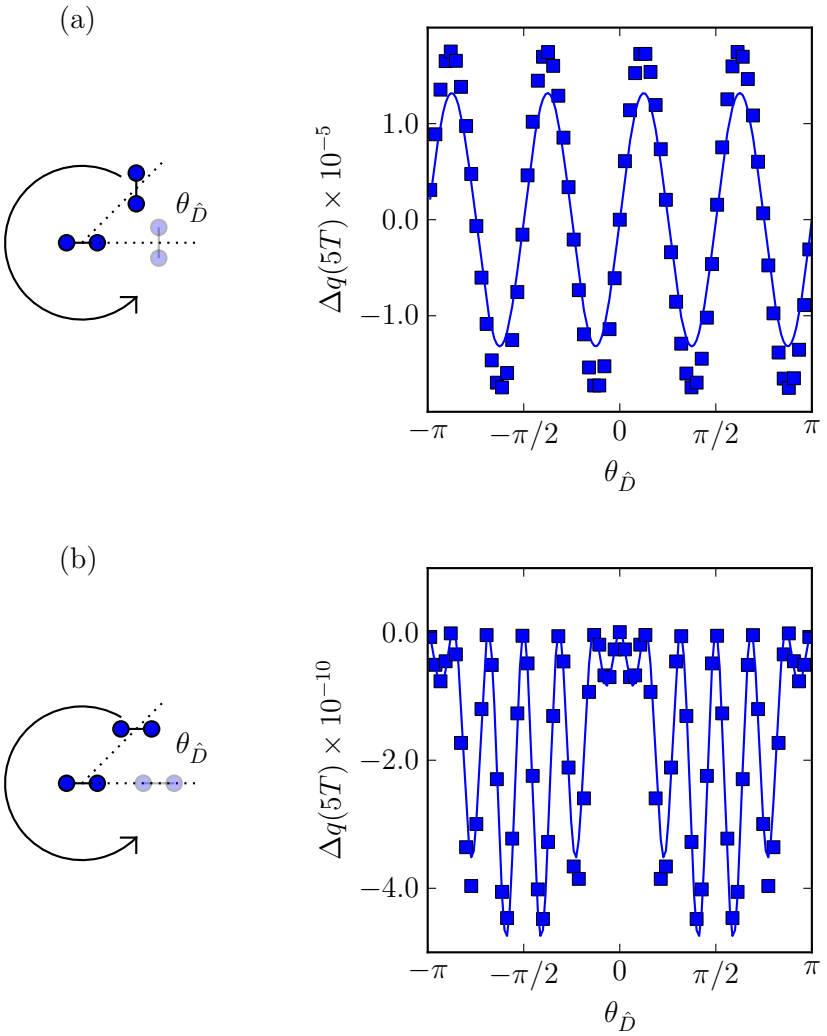

sphere. For the lattice size, we considered values $x = 3, 5, 7, 9$ corresponding to a total dumbbell number $S = 3^3, 5^3, 7^3, 9^3$ respectively. To characterize collective motion, we measured the mean square displacement per particle averaged over different initial configurations,

$$\langle\langle R\left(t\right)^2\rangle\rangle := \frac{1}{W}\sum_{w=1}^{W}\frac{1}{S}\sum_{\sigma=1}^{S}\left[R^{\sigma}\left(t;w\right)-R^{\sigma}\left(0;w\right)\right]^2, \tag{2.22}$$

where the variable $w = 1, \ldots, W$ labels sets of different initial conditions. We distinguish two classes of initial conditions:

1. An "optimized" phase distribution: phases were set such that each dumbbell had a phase of 0 or $\pi/2$ with all nearest neighbors having the alternate phase in the manner of a 3D checkerboard. The corresponding results for the microscopic simulation and stroke-averaged model are indicated by filled symbols and solid lines in Figs. 2.6 and 2.7 respectively.

2. A randomized phase distribution: phases were set to random values evenly distributed on the interval $[0, 2\pi)$ with a different distribution for each run. The corresponding results are indicated by unfilled symbols and dashed lines in Figs. 2.6 and 2.7 respectively.

Fig. 2.6 illustrates how the mean square displacement over a period, $\langle\langle R\left(T\right)^2\rangle\rangle$, varies with density ρ (or equivalently with grid spacing) for an array of $(5 \times 5 \times 5) = 125$ dumbbells. As evident from the diagram, the prediction from the stroke-averaged model is in good agreement with the scaling behaviour measured by microscopic simulation. Furthermore, by comparing filled with unfilled symbols and solid with dashed lines, we note that the collective displacement $\langle\langle R\left(T\right)^2\rangle\rangle$ is generally smaller for the randomized phase distribution, corroborating the fact that optimizing phase distributions can considerably enhance the effectiveness of collective motions [91].

Figure 2.6: (a) Scaling of the mean square displacement per particle (measured over a period) with number density for two different phase distributions. The diagram depicts the simulation results for a cubic array of $(5 \times 5 \times 5) = 125$ dumbbells, averaged over $W = 100$ different runs, each with random initial orientations. Symbols refer to the spring-based model and lines to the stroke-averaged model (2.14)-(2.17). The collective mean square displacement is proportional to $\left(\ell\rho^{1/3}\right)^{2\nu}$ with an exponent $\nu = -4$. (b) Mean square displacement rescaled (i.e., multiplied) by $\rho^{-8/3}$. We observe that for an "optimized" phase distribution (filled symbols/solid lines the effective mean square displacement is larger than for a uniformly random phase distribution (empty symbols/dashed lines). On this scale, statistical error bars (not shown) are smaller than the size of the symbols. The shift between lines and symbols, caused by the relatively large parameter ratio $a/\ell = 0.2$ used in these simulations, is consistent with the value expected from Fig. 2.4 (c).

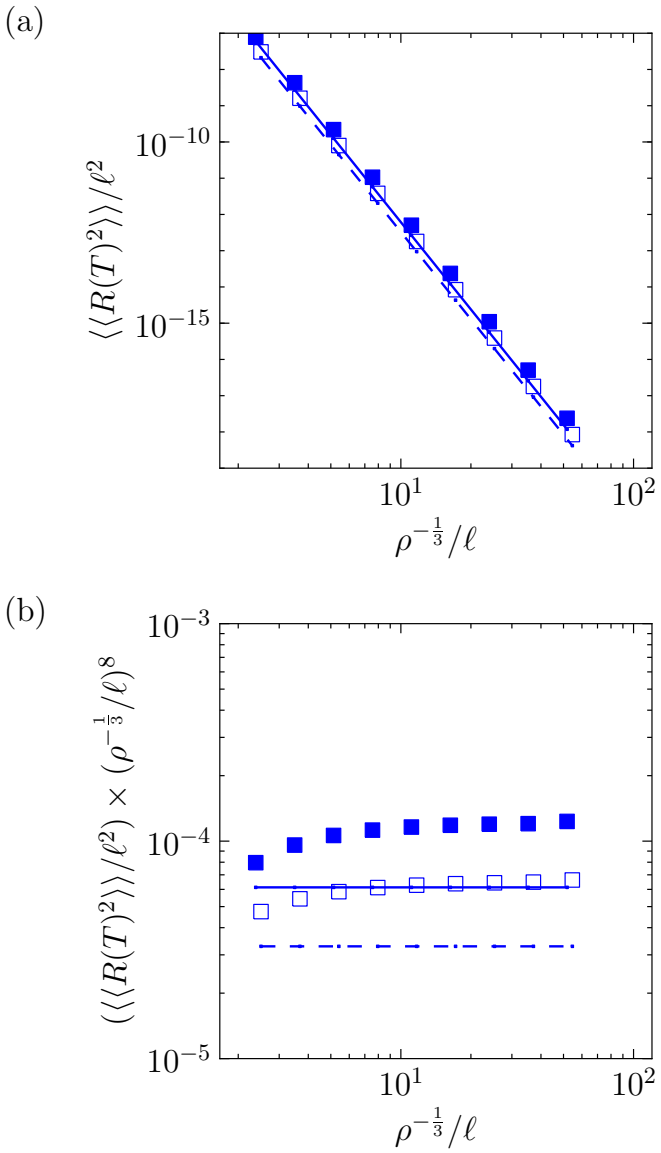

Figure 2.7: Scaling of the mean square displacement per particle over a period with dumbbell number S at constant density. The diagram depicts the simulation results for collections of dumbbells arranged on a cubic $(x \times x \times x)$-lattice with $x = 3, 5, 7, 9$ and spacing 10ℓ averaged over $W = 10$ random orientations. Symbols refer to the spring-based model and lines to the far-field stroke-averaged model (2.14)-(2.17), beginning from the same initial conditions. Increasing the number of swimmers while keeping number density constant produces only minimal gains in translational speed. The collective mean square displacement is smallest for $(3 \times 3 \times 3) = 27$ swimmers, which is due to the relatively large number of swimmers with an incomplete set of "nearest neighbours" in this case. We also observe that for an "optimized" phase distribution (filled symbols/solid lines) the effective mean square displacement is larger than for a uniformly random phase distribution (empty symbols/dashed lines). Again, the shift between lines and symbols, caused by the relatively large parameter ratio $a/\ell = 0.2$ used in these simulations is consistent with the value expected from Fig. 2.4 (c).

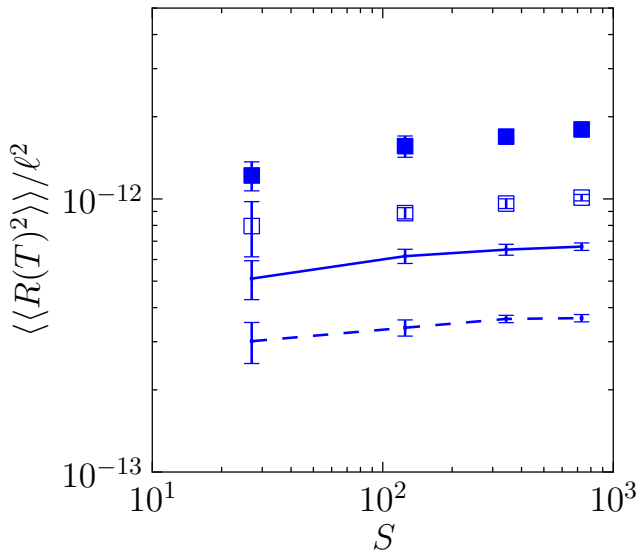

Fig. 2.7 shows how the quantity $\langle\langle R(T)^2\rangle\rangle$ scales with total number S of the dumbbells at fixed density ρ. After a slight jump from the $(3 \times 3 \times 3)$ case, adding more swimmers at fixed density ρ produces only a minimal increase in displacement, and the effect appears for both optimized or randomized phase distributions; again, collective displacement is generally smaller for randomized phase distributions than for optimal phase distributions.

2.7 Discussion

We have derived stroke-averaged analytics for pair interactions of symmetric dumbbells, comparing them to independent time-resolved numerical simulations in multiple cases: translation along a common axis, rotation in various orientations, and in 3D suspensions of cubic arrays. In all cases the analytics and numerics show good agreement.

We compared stroke-averaged analytics with microscopic numerical simulations at relatively low densities, and observed very good agreement down to separations of a few body lengths and intermediate-to-high swimmer densities, where the effective equations of motion are expected to become less accurate. We therefore conclude that the coarse-grained model is a reasonable approximation. However, it should be kept in mind that at very high densities, when collisions (i.e., steric effects) become relevant, lubrication effects as well as near-field hydrodynamics must be modelled more carefully.

In the case of dumbbells arranged on a 3D grid, the translational speed due to hydrodynamic interaction between dumbbells varies predictably with spacing, tending toward $|D|^{-4}$ decay, where $|D|$ is the distance between dumbbell centres. Due the short range of the effective hydrodynamic interactions for symmetric dumbbells, adding more swimmers at a fixed density has only a minimal impact on dumbbell

translational speed. On the other hand, the collective swimming speed can be noticeably increased by replacing a randomized phase distribution with an ordered, "optimal" distribution of phases such that the difference in phase between a periodically-driven dumbbell and its nearest neighbors is $\pi/2$.

More generally, our numerical investigations illustrate that GPU-based simulations of multi-swimmer systems can provide a valuable tool for studying collective motions at very low Reynolds number. Moreover, the CUDA algorithm used in our computer experiments can be readily adapted to simulate hydrodynamic interactions between colloids that can be trapped and manipulated by means of optical tweezers [52], simply by adding additional forces in the form of external potentials. Such theoretical investigations can help to create more efficient micropumps, e.g., by optimizing the phase relations in oscillating arrays of colloids. The basic design of the simulation, with replaceable stages of computation, makes it relatively easy to create and test bead-based swimmer models with only moderate effort. Modules could also be added which provide external forces or torques to examine behaviours such as gyrotaxis or gravitaxis and sedimentation, which can result in bioconvection [92] and other group effects.

Finally, another long-term objective is to compare many-swimmer simulations with predictions of effective field theories [8]. Our results suggest that a promising approach towards achieving this goal may be a two-step procedure. First, one should try to derive stroke-averaged equations of motion that correctly capture the phase dependence on the level of effective two-particle interactions. We have shown that such coarse-grained models can correctly reproduce many of the main features of the microscopic model, at least for our dumbbell swimmers. Second, one could then implement the coarse-grained equations themselves into a CUDA environment to provide a basis for comparison with predictions from a field theory derived from the pair interactions. Compared to simulations of the full microscopic dynamics, this may

reduce the effective simulation time by an additional factor of 100 or more since the analytic stroke-averaging procedure makes it unnecessary to numerically resolve the smallest dynamical time scales in the system.

However, while symmetric dumbbells represent the *simplest* model of collective swimming, the simplicity of their motion and their apolarity may make these a special case. Rather than proceeding with further use of the analytics, it is interesting to examine what happens when the symmetry of these swimmers is broken, simply by making one sphere larger than the other.

Chapter 3

Collective motion of asymmetric dumbbells

3.1 Introduction and motivation

In Chapter 3, we examined the motion of apolar, symmetric dumbbells which oscillated in a reciprocal fashion, showing that these could exhibit group motion. We found that coarse-grained, stroke-averaged analytics could provide a simplified (but nevertheless reasonably accurate) model of this motion which was verified by comparison with simulation in cases of pair interactions and simulations of suspensions.

However, the use of a symmetric dumbbell represents only a very basic sort of behaviour. Not only is it clear that the interactions are very slight and decay very rapidly (as $\propto |D|^{-4}$ for translation and $\propto |D|^{-5}$ for rotation, see Eqns. (2.16) and (2.17)), the motion itself is very slow, moving an individual swimmer on the order of 10^{-6} body lengths per period for parameters used in Chapter 2.

Symmetric dumbbells are apolar, in that they do not distinguish their orientation vector $\hat{\boldsymbol{N}}$ from its negation $-\hat{\boldsymbol{N}}$. Simha and Ramaswamy [8] noted significant differences in the propagation modes and number fluctuations between suspensions of

Figure 3.1: The dumbbell model is easily modified by making the spheres different sizes such that $a_1 \neq a_2$.

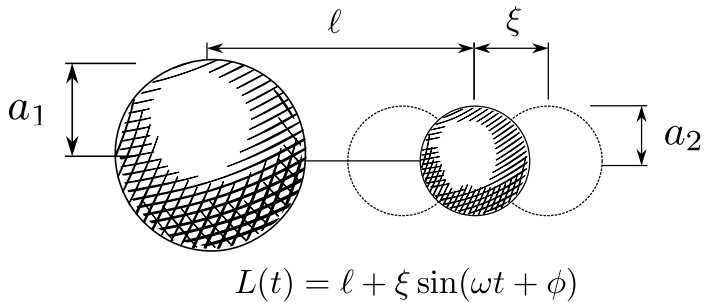

polar and apolar particles. The introduction of polarity may have significant impacts on the pair interactions of swimmers, and a suspension of asymmetric dumbbells may constitute the simplest model system for studying how the symmetry of the microscopic constituents affects both hydrodynamics and orientational order in the continuum limit.

We shall use the same basic method as in Chapter 3, although with the minor modifications necessary to introduce asymmetry into the analytical equations and to deal with its consequences.

3.2 Changes in method

We modify our dumbbell model by making one sphere larger than the other, as shown in Fig. 3.1. The method outlined in Section 2.3 for determining two-swimmer pair interactions relies on knowledge of time-varying quantities. One must know the positions of each swimmer's spheres $\boldsymbol{X}_1^\sigma$ and $\boldsymbol{X}_2^\sigma$ relative to its position $\boldsymbol{R}^\sigma$ to determine the small quantities h_m^σ relative to $|\boldsymbol{D}|$ in the double-expansion of the Oseen tensor. One must also know the time-varying force applied to each sphere of the source dumbbell ρ. With both those quantities known, the advection at each sphere of the target dumbbell σ may be calculated to analyze motion. It is advantageous for the Taylor-expansion approach to have a swimmer position variable which changes as

little as possible during a stroke such that the vector $\boldsymbol{D}^{\sigma\rho}$ does not change, placing the variation instead in the small parameters h_m^σ.

Introducing asymmetry affects both the notion of swimmer position $\boldsymbol{R}^\sigma$ as well as the calculation of the small parameters h_m^σ. The question "where *is* a swimmer?" turns out to be nontrivial. Since our spheres are moving along a line via an opposing force pair, we define a centre of expansion and contraction by the speeds of the two spheres. If the two spheres moved inward along the swimmer's axis at constant speeds $v_{1,2}$, they would coincide at the point

$$\boldsymbol{R} = \frac{v_1 \boldsymbol{X}_2 + v_2 \boldsymbol{X}_1}{v_1 + v_2}. \tag{3.1}$$

For a symmetric dumbbell, the two spheres expanded and contracted symmetrically ($v_1 = v_2$) around the dumbbell's *geometric* centre, which for clarification we shall now label $\boldsymbol{R}_\mathrm{G}$, defined as

$$\boldsymbol{R}_\mathrm{G} = \frac{1}{2}\left(\boldsymbol{X}_1 + \boldsymbol{X}_2\right), \tag{3.2}$$

with displacements from centre for each dumbbell sphere

$$h_1 = -\frac{1}{2}L\left(t\right), \qquad h_2 = \frac{1}{2}L\left(t\right). \tag{3.3}$$

We chose the geometric centre as the dumbbell position in Chapter 3, but using the same quantity for asymmetric dumbbells results in incorrect results. Since the two spheres travel at different rates due to their unequal radii, the geometric centre of an asymmetric dumbbell exhibits cyclic motion during its stroke, causing incorrect values for the small displacements h_m^σ.

In order to apply our method to asymmetric dumbbells, we must find a new definition of the dumbbell's center, and new expressions for the small displacements h_m^σ of the spheres away from that center over time. It is tempting to use the *centre*

of hydrodynamic stress as defined by Brenner [93],

$$\boldsymbol{R}_{\mathrm{H}} = \frac{a_2 \boldsymbol{X}_2 + a_1 \boldsymbol{X}_1}{a_2 + a_1}, \tag{3.4}$$

which is the same result as one obtains by using the Stokes velocity $v_m \propto 1/(6\pi\mu a_m)$ in (3.1). Substituting in (2.5) and solving for h_1, h_2 gives us leg lengths

$$h_1 = -\frac{a_2}{(a_1 + a_2)} L(t), \qquad h_2 = \frac{a_1}{(a_1 + a_2)} L(t). \tag{3.5}$$

This gives good results for rotation, but when calculating the translation term for pair reactions, we found it produced a strange result: the translation expression reduced to zero.

The answer was to take not only the Stokes velocity of the spheres into account as with (3.4), but also the Oseen contributions of the opposing spheres. This led to what we term the *centre of hydrodynamic stretch*,

$$\boldsymbol{R}_{\mathrm{S}} = \frac{2(a_2 \boldsymbol{X}_2 + a_1 \boldsymbol{X}_1)\ell - 3a_1 a_2 (\boldsymbol{X}_2 + \boldsymbol{X}_1)}{2((a_2 + a_1)\ell - 3a_1 a_2)}, \tag{3.6}$$

giving leg lengths

$$h_1 = -\frac{a_2 L(t)(2\ell - 3a_1)}{2\ell(a_1 + a_2) - 6a_1 a_2}, \qquad h_2 = \frac{a_1 L(t)(2\ell - 3a_2)}{2\ell(a_1 + a_2) - 6a_1 a_2}, \tag{3.7}$$

where ℓ is the mean dumbbell length as in Section 2.2. It should be noted that using (3.1) assumes that the ratio of speeds remains constant, while the Oseen contribution would change with relative dumbbell length, so (3.6) should only be regarded as accurate over a dumbbell's full stroke in the limit $\xi \ll \ell$.

Fig. 3.2 compares the variations of the three quantities $\boldsymbol{R}_{\mathrm{G}}$, $\boldsymbol{R}_{\mathrm{H}}$, $\boldsymbol{R}_{\mathrm{S}}$ over time for

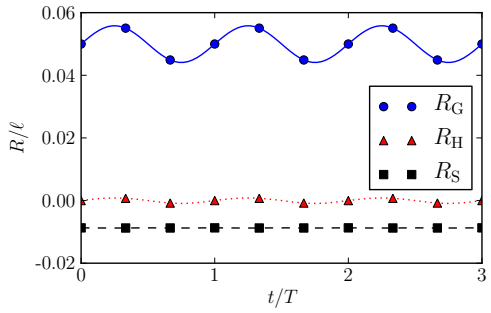

Figure 3.2: Comparison of geometric centre $\boldsymbol{R}_G$, hydrodynamic centre $\boldsymbol{R}_H$, and stretch centre $\boldsymbol{R}_S$ for an isolated dumbbell with moderate asymmetry; $\ell = 5\mu$m, $\xi = 0.5\mu$m, $a_1 = 0.55\mu$m, $a_2 = 0.45\mu$m, measured over three periods of simulation. Of the three quantities, $\boldsymbol{R}_S$ shows the least variation with time and is thus the best choice for swimmer centre used to define the vector between dumbbells.

a given microscopic simulation of an isolated dumbbell. The difference in periodic variation for the three approximations, as well as the differences between their average values during a stroke, means that the choice of centre for any given calculation is not to be dismissed lightly. For example, a static (non-oscillating) asymmetric dumbbell subjected to Brownian motion or shear flow may rotate in place about its hydrodynamic centre, causing translation of its geometric centre. As $\boldsymbol{R}_S$ is the most stable point during an oscillating asymmetric dumbbell's stroke, it is the most appropriate choice here.

Additionally, the presence of asymmetry magnified any problems with choice of integrator; while for symmetric dumbbells simple Euler-style integration could suffice given a small timestep, asymmetric dumbbells experienced a small amount of numeric "creep" and appeared to self-swim. For this reason a two-step Heun integrator [82] was used to increase the quality of integration and the timestep and spring constants adjusted to reduce the effects of this error until it was no longer noticeable in comparisons to analytics.

3.3 Analysis

Following the considerations of Section 3.2, we use Eqn. (2.13b) with the definitions of leg length from (3.7) to determine rotations resulting from pair interactions. Em-

ploying the same procedure as used in Section 2.3, we find the asymmetry causes a second term of lower order to survive in the expansion of the Oseen tensor. As can be seen in (3.9), (3.13), we gain a lower-order D^{-4} term which was not present for symmetric dumbbells. Similarly, the translation of the centre of hydrodynamic stretch gains a D^{-3} term.

With all these considerations and simplifications, and restricting to two-body interactions, we find, for asymmetric dumbbells, coarse-grained equations of motion of the form

$$\dot{R}^{\sigma}_{\mathrm{S}i} = \left(\frac{a_2^2 - a_1^2}{a_1^2 + a_2^2}\right) \sum_{\rho \neq \sigma} I_i^{\sigma\rho} + \sum_{\rho \neq \sigma} J_i^{\sigma\rho}, \tag{3.8}$$

$$\dot{\hat{N}}^{\sigma}_i = -\left(\delta_{ik} - \hat{N}^{\sigma}_i \hat{N}^{\sigma}_k\right) \left\{ \left(\frac{a_2 - a_1}{a_1 + a_2}\right) \sum_{\rho \neq \sigma} K_k^{\sigma\rho} + \sum_{\rho \neq \sigma} L_k^{\sigma\rho} \right\}, \tag{3.9}$$

where the I, J, K, L terms to leading order in ξ/ℓ are given by

$$\begin{aligned} I_i^{\sigma\rho} =& \Lambda\omega \sin\left(\phi^{\sigma} - \phi^{\rho}\right) \frac{9}{64} \left(\frac{\Lambda}{\ell}\right) \left(\frac{\xi}{\ell}\right)^2 \left(\frac{\ell}{|D_{\mathrm{S}}^{\sigma\rho}|}\right)^3 \times \\ & \hat{N}^{\sigma}_i \left(1 - 3r^2 - 3s^2 - 6qsr + 15s^2r^2\right), \end{aligned} \tag{3.10}$$

$$\begin{aligned} J_i^{\sigma\rho} =& \Lambda\omega \sin\left(\phi^{\sigma} - \phi^{\rho}\right) \frac{9}{64} \left(\frac{\xi}{\ell}\right)^2 \left(\frac{\ell}{|D_{\mathrm{S}}^{\sigma\rho}|}\right)^4 \times \\ & \left\{ \hat{N}^{\sigma}_i \left(2s + 4qr - 10sr^2\right) + \hat{D}^{\sigma\rho}_{\mathrm{S}i} \left(1 + 2q^2 - 5s^2 - 5r^2 - 20qsr + 35s^2r^2\right) \right\}, \end{aligned} \tag{3.11}$$

$$\begin{aligned} K_k^{\sigma\rho} =& \omega \sin\left(\phi^{\sigma} - \phi^{\rho}\right) \left(\frac{9}{32}\right) \left(\frac{\Lambda}{\ell}\right) \left(\frac{\xi}{\ell}\right)^2 \left(\frac{\ell}{|D_{\mathrm{S}}^{\sigma\rho}|}\right)^4 \times \\ & \hat{D}^{\sigma\rho}_{\mathrm{S}k} \left(1 + 2q^2 - 5s^2 - 5r^2 - 20qsr + 35s^2r^2\right), \end{aligned} \tag{3.12}$$

$$\begin{aligned} L_k^{\sigma\rho} =& \omega \sin\left(\phi^{\sigma} - \phi^{\rho}\right) \left(\frac{15}{64}\right) \left(\frac{\Lambda}{\ell}\right) \left(\frac{\xi}{\ell}\right)^2 \left(\frac{\ell}{|D_{\mathrm{S}}^{\sigma\rho}|}\right)^5 \times \\ & \hat{D}^{\sigma\rho}_{\mathrm{S}k} \left(3s + 6rq + 6sq^2 - 7s^3 - 21sr^2 - 42qs^2r + 63s^3r^2\right). \end{aligned} \tag{3.13}$$

Here,

$$\Lambda := 2a_1a_2/\left(a_1+a_2\right) \tag{3.14}$$

denotes the harmonic mean of the sphere radii, the vectors $\boldsymbol{D}_{\mathrm{S}}$, $\hat{\boldsymbol{D}}_{\mathrm{S}}$ have the same meaning as used in (2.9), with the vector pointing between the centres of hydrodynamic stretch of the swimmers, and s, r, q abbreviate projections (2.10).

Compared to Eqns. (2.14)-(2.17), prominent features are evident. The stroke-averaged interactions I, J, K, L vanish if the phases ϕ^σ and ϕ^ρ differ by multiples of π. Secondly, in the limit $|\boldsymbol{D}^{\sigma\rho}| \gg \ell$ the leading contribution to $\dot{\boldsymbol{R}}^\sigma_{\mathrm{H}}$ is given by the I-terms, which decay as $|\boldsymbol{D}^{\sigma\rho}|^{-3}$ [57]. By contrast, for symmetric dumbbells with $a_1 = a_2$ the first term in (3.9) is absent and one recovers equations (2.14)-(2.17) from Chapter 3, which decay asymptotically as $|\boldsymbol{D}^{\sigma\rho}|^{-4}$. Similarly, asymmetric dumbbells experience angular velocity contributions $\dot{\hat{\boldsymbol{N}}}^\sigma$ which decay as $|\boldsymbol{D}^{\sigma\rho}|^{-4}$, whereas the effective rotation interaction for symmetric dumbbells decays as $|\boldsymbol{D}^{\sigma\rho}|^{-5}$. The introduction of asymmetry has moved the interactions to a lower order.

3.4 Testing asymmetric dumbbell pair interactions

3.4.1 Aligned dumbbell pairs

As in Subsection 2.5.1, we compare the interactions first using aligned dumbbell pairs and examine the effects of linear translation with spacing, as studied by Lauga and Bartolo [57]. Aligned dumbbells do not change their orientation, and Eqns. (3.8),(3.10),(3.11) reduce to

$$\begin{aligned}\dot{R}^\sigma_{\mathrm{S}} =& \frac{9}{16}\sum_{\rho\neq\sigma}\Lambda\omega\sin\left(\phi^\sigma-\phi^\rho\right)\left(\frac{\xi}{\ell}\right)^2\times \\ & \left\{\left(\frac{a_2^2-a_1^2}{a_2^2-a_1^2}\right)\left(\frac{\Lambda}{|D^{\sigma\rho}_{\mathrm{S}}|}\right)\left(\frac{\ell}{|D^{\sigma\rho}_{\mathrm{S}}|}\right)^2\hat{\boldsymbol{N}}^\sigma+\left(\frac{\ell}{|D^{\sigma\rho}_{\mathrm{S}}|}\right)^4\hat{\boldsymbol{D}}^{\sigma\rho}_{\mathrm{S}}\right\},\end{aligned} \tag{3.15}$$

where $\dot{R}_{\mathrm{S}}^{\sigma}$ denotes the coordinates of the swimmers' centres of stretch along the common axis. The lines in Fig. 3.3 represent the dynamics of aligned dumbbell pairs as predicted by (3.15), and symbols indicate the results of corresponding microscopic model simulations. We quantify collective motion of the dumbbell pairs in terms of their mean collective displacement ((2.19), solid lines/filled symbols in Fig. 3.3) and mean relative distance ((2.20), dashed lines/unfilled symbols in Fig. 3.3).

As evident from the two diagrams in Fig. 3.3, we find qualitatively different behaviour depending on the symmetry of the initial dumbbell pair configuration. Fig. 3.3 (a) summarizes results for reflection-symmetric initial conditions. In this case, the pair can move in either direction, depending on whether the smaller spheres point towards or away from each other, but the mean distance between the two dumbbells remains constant. By contrast, the translationally invariant configurations in Fig. 3.3 (b) always move in the same direction with nearly identical speeds for symmetric and asymmetric dumbbell pairs. We note that our results for the translationally invariant geometries essentially agree with those obtained by Lauga and Bartolo [57]. However, we find a different behaviour for mirror symmetric configurations (cf. Fig. 2 (a) of [57]).

Furthermore, Fig. 3.4 shows how both the collective displacement and the relative separation per period vary with the distance between the dumbbells, with symbols, colors, and line-styles referring to the same configurations/model parameters as in Fig. 3.3. The dynamics of the microscopic model is very well described by the averaged equations (3.15) down to distances of a few body lengths. In particular, as also correctly predicted by the stroke-averaged equations (3.15), the translational motion has components in both $\hat{\boldsymbol{N}}^{\sigma}$ and $\hat{\boldsymbol{D}}_{\mathrm{S}}^{\sigma\rho}$, so for the mirror symmetric configuration with small spheres pointing outwards the pair velocity reverses its sign at a distance of approximately 11ℓ; see the black diamonds in Fig. 3.4 (a).

Figure 3.3: Depending on the symmetry of their initial configuration, aligned dumbbell pairs exhibit qualitatively different collective motions. In both diagrams, lines were obtained by numerical integration of the stroke-averaged equations (3.15), whereas symbols show the simulation results for the microscopic spring-based dumbbell model described in Section 2.2. Solid lines and filled symbols depict the mean displacement $\overline{R_{\mathrm{S}}^{21}}(t) - \overline{R_{\mathrm{S}}^{21}}(0) = \{[R_{\mathrm{S}}^{2}(t) + R_{\mathrm{S}}^{1}(t)] - [R_{\mathrm{S}}^{2}(0) + R_{\mathrm{S}}^{1}(0)]\}/2$ of the hydrodynamic centres. Dashed lines and unfilled symbols indicate the relative separation $\Delta R_{\mathrm{S}}^{21}(t) - \Delta R_{\mathrm{S}}^{21}(0) = [R_{\mathrm{S}}^{2}(t) - R_{\mathrm{S}}^{1}(t)] - [R_{\mathrm{S}}^{2}(0) - R_{\mathrm{S}}^{1}(0)]$. (a) For mirror symmetric configurations, the mean distance between the dumbbells remains constant and the dumbbell pair can move in either direction. In particular, asymmetry can enhance the collective speed, see triangles. (b) For translation invariant configurations, asymmetry does not affect the collective pair velocity, but depending on the initial orientation the dumbbells either approach each other (red triangles) or move away from each other (black diamonds). Simulation parameters are roughly comparable to those of Lauga and Bartolo [57]: Initial separation $\Delta R_{\mathrm{S}}^{21}(0) = R_{\mathrm{S}}^{2}(0) - R_{\mathrm{S}}^{1}(0) = 10\ell$, mean dumbbell length $\ell = 5\mu\mathrm{m}$, driving frequency $\omega = 500\mathrm{s}^{-1}$ (time is given in units of the stroke period $T = 2\pi/\omega$), stroke amplitude $\xi = 0.1\ell$, $\Lambda = 2a_1a_2/(a_1 + a_2) = 0.15\ell$ with $a_2 = a_1/2$ for asymmetric dumbbells, phase difference $\phi^2 - \phi^1 = \pi/2$. For the microscopic model: spring constants $k_0 = 0.001\mathrm{kg/s}^2$, viscosity $\mu = 10^{-3}\mathrm{kg/(ms)}$, particle mass density $\varrho = 10^3\mathrm{kg/m}^3$; simulation timestep $\Delta t \approx 10^{-4}T$. We note that the quantitative difference between symbols and lines decreases when choosing smaller ratios a_α/ℓ, cf. discussion in Subsection 2.5.1.

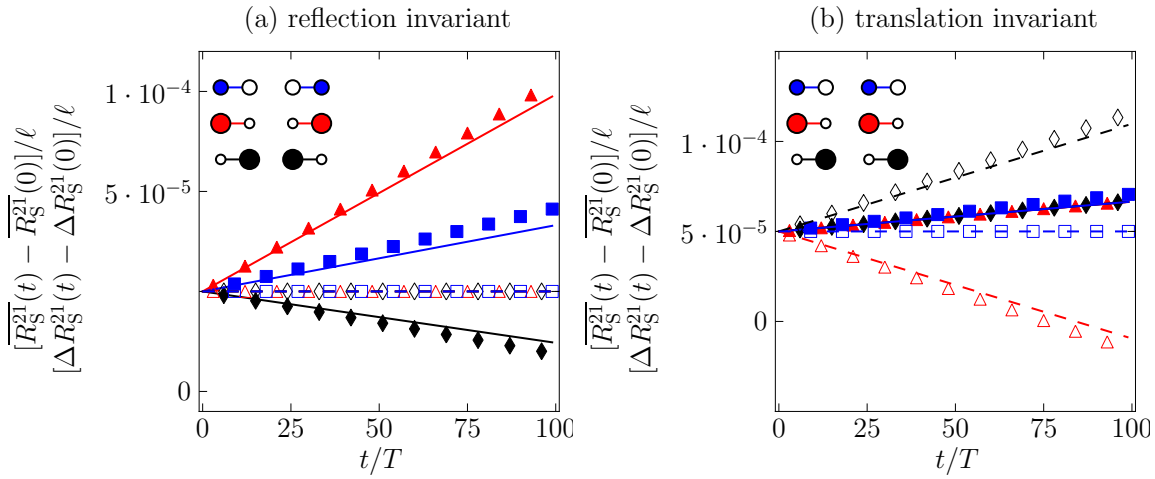

Figure 3.4: Distance dependence of the collective motion and separation for aligned dumbbell pairs in (a) mirror-symmetric and (b) translation-invariant configurations. Line styles and symbols correspond to the same configurations and simulation parameters as used in Fig. 3.3. For a reflection symmetric configuration such that the small spheres point outwards, see black diamonds in diagram (a), the collective velocity reverses its sign at a distance of approximately 11ℓ. Qualitatively, this change is correctly reflected by the stroke-averaged equation (3.15), see solid black line in diagram (a). As in Chapter 3, the stroke-averaged equations describe the microscopic dumbbell dynamics reasonably well down to distances of a few body lengths.

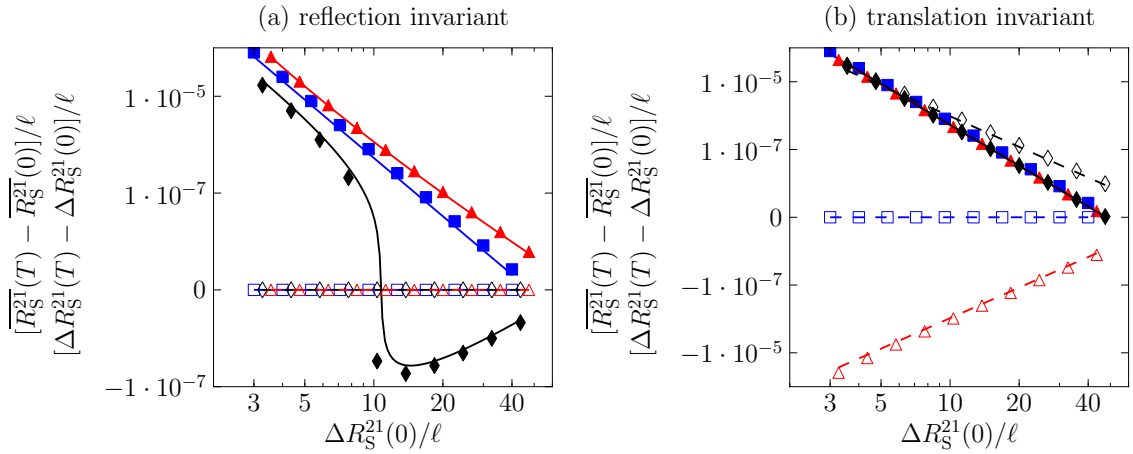

3.4.2 Three-dimensional pair interactions

In two- and three-dimensional swimmer geometries, hydrodynamic interactions can not only lead to collective translational motion but may also induce orientational changes. To illustrate both effects and to verify the validity of the angular velocity equations (3.9),(3.12),(3.13), we consider various different initial configurations as sketched next to the diagrams in Fig. 3.5 and Fig. 3.6. In each of the diagrams, blue symbols/squares indicate the change of the relative orientation of the two dumbbells, quantified through the change of the projections noted in (2.21). It is important to note that, for symmetric dumbbells with $a_1 = a_2$, the orientation vector is *not* uniquely defined (it is invariant under the transformation $\hat{\boldsymbol{N}} \mapsto -\hat{\boldsymbol{N}}$). For asymmetric dumbbells, however, the orientation can be uniquely characterized by means of the different sphere radii. In our plots, we fix the orientation as pointing from the filled to the unfilled sphere in all cases.

Figure 3.5: In-plane rotation of the initial swimmer displacement: Blue solid lines/blue squares denote change of relative orientation Δq. Red dotted lines/red triangles denote change of relative distance ΔD_{S}. Swimmer parameters are identical with those use in Figs. 3.4-3.3, except $\Lambda = 2a_1a_2/\left(a_1 + a_2\right) = 0.1\ell$.

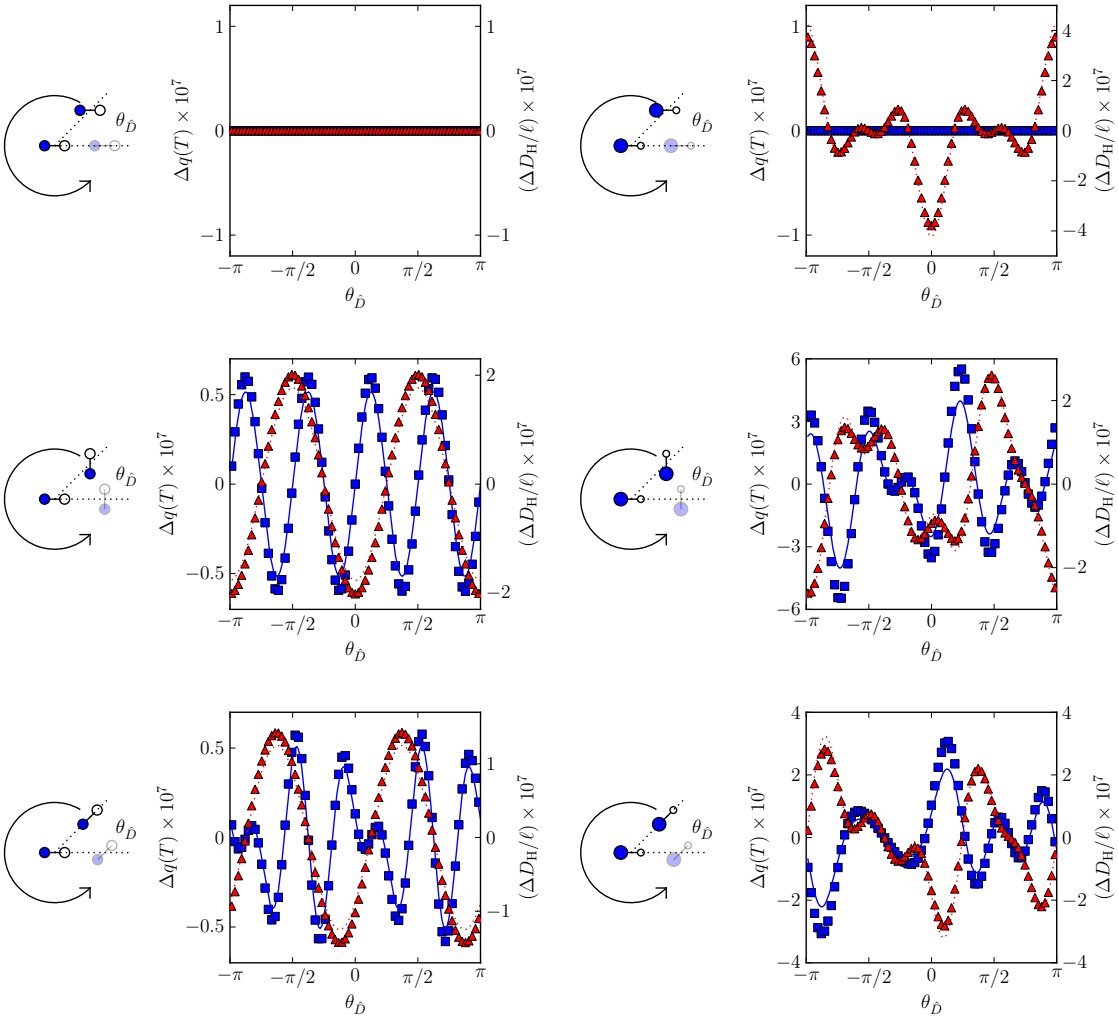

Figure 3.6: Comparison of rotation for skew configurations. In all cases, the relative orientation of the swimmers $\boldsymbol{D}_{\mathrm{S}}^{\sigma\rho}$ remains fixed, but one swimmer has its initial orientation rotated around a vector perpendicular to an axis. Blue solid lines/blue squares denote change of relative orientation Δq. Red dotted lines/red triangles denote change of relative distance ΔD_{S}.

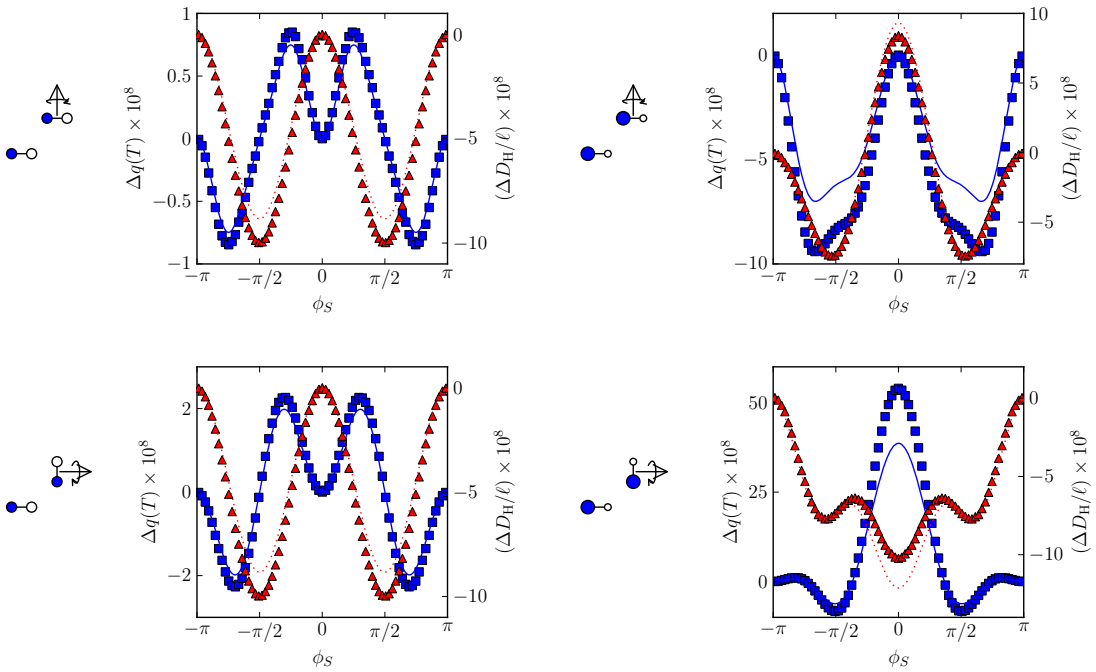

Furthermore, the red lines/triangles show the change in the relative separation of the two dumbbells after one period,

$$\Delta D_{\mathrm{S}}(T) := \left|\boldsymbol{D}_{\mathrm{S}}(T) - \boldsymbol{D}_{\mathrm{S}}(0)\right|/\ell, \qquad \boldsymbol{D}_{\mathrm{S}}(t) := \left(\left[\boldsymbol{R}^{\sigma}_{\mathrm{S}}(t) - \boldsymbol{R}^{\ell}_{\mathrm{S}}(t)\right]\right)/\ell, \quad (3.16)$$

where we normalize ΔD_{S} by dividing by the dumbbell mean length ℓ. For $\Delta D_{\mathrm{S}}(T) > 0$ the dumbbells approach each other; for $\Delta D_{\mathrm{S}}(T) < 0$ they move away from each other.

To illustrate the effects of a change in symmetry, we plot the results for symmetric and asymmetric dumbbell pairs next to each other. As one may readily observe, asymmetry does strongly affect both the translational and orientational motions of the dumbbells. This suggests that geometry can play an important role for the emergence of orientational (dis)order in suspensions of hydrodynamically interacting organisms. Generally, Figs. 3.5 and 3.6 confirm that the coarse-grained equations of motions (3.9)-(3.13) are able to quantitatively reproduce the characteristic features of the microscopic dynamics.

3.5 Discussion

We have broken the symmetry of the dumbbells discussed in Chapter 2, finding that the resultant asymmetry forces us to define dumbbell position more precisely, causes the two ends of the dumbbell to vary asymmetrically about the new centre, and changes the time-dependent force applied. The combination of these changes results in interactions with a component dependent on the asymmetry but which acts at a lower order (D^{-3} versus D^{-4} for translation and D^{-4} versus D^{-5} for rotation). At long range, these asymmetric components dominate the interaction, even reversing direction of motion in some cases, as shown in Fig. 3.4.

The introduction of asymmetry also posed computational challenges for the time-

resolved simulations, as numerical error with naive (Euler) integration became significant, causing fixed-radius reciprocal dumbbells to move in the simulation when they should not. This necessitated use of a higher-level (Heun) integrator and more careful selection of timestep to achieve accurate results. As the group motion produced by fixed-radius dumbbells is of a very small scale compared to their body length, even slight numerical error can cause inaccurate results.

Suspensions of dumbbells represent a simple isolated model of group swimming, as they are neither self-motile nor do they generate a net flow field. However, we are also interested in self-motile particles which do generate net flow. To examine this sort of swimmer, we shall perturb the symmetry of the dumbbells again, by allowing the radii of the spheres to vary with time, producing a phased dipolar swimmer.

Chapter 4

A phased dipolar swimmer

4.1 Motivation

Thus far, we have shown that reciprocal swimmers can exhibit collective motion, and that perturbing the symmetry of those swimmers can generate lower-order corrections which greatly increase the effectiveness of group motion.

Even so, the motion produced has been very slight; for asymmetric dipole pairs with the geometries we examined in Section 3.4, translational motion was on the order of 10^{-5} body lengths per swimming cycle. While the effects are noticeable and worthy of study, it is difficult to imagine a bacterium moving effectively in this manner.

A host of self-swimming models have been proposed. Some prescribe a succession of shape changes, such as the three-link swimmer proposed by Purcell [21, 94, 95], while others prescribe the flow of fluid across a static surface, such as the squirmers modeled by Ishikawa and Pedley [43, 45, 44]. Several model swimmers use colloidal particles as their constituent elements, such as the three-sphere swimmer of Najafi and Golestanian [35, 38, 39, 41], Avron's pushmepullyou dimer [36], or the Purcell rotator studied by Dreyfus et al. [96].

We shall now take steps to modify our dumbbell swimmer into a variable-resistance

swimmer which can self-swim and generate flow purely by changing the resistances of its two ends in a periodic fashion. This gives the swimmer two degrees of freedom: the phase difference between the resistances, and the difference between their mean and the phase of the length change. These two degrees of freedom give the swimmer a large phase space where different phase parameters change the swimming behaviour and flow field without changing essential geometry and sizes of the swimmer. This makes the model quite versatile, as a given geometry can produce particles which swim with no significant flow field, those which cannot swim but generate a strong extensile or contractile dipolar flow field, or any combination of these.

We find that the presence of self-swimming and flow dominates pair interactions, and that while our model produces a pure dipolar flow field, implementing the changing resistance as a variable-length dumbbell adds a quadrupolar component, allowing some comparisons to the three-sphere swimmer of Najafi and Golestanian [35].

4.2 The model and the role of phase

In order to give our dumbbell swimmer self-motility and flow, it will be necessary to break reciprocality [21] in the absence of other swimmers. We shall choose to modify the two-sphere dumbbell, both to provide continuity with the previous dumbbell models of Chapters 2 and 3, and also to keep the model as simple as possible while allowing richness of behaviour not achievable with the classic Najafi-Golestanian three-sphere swimmer. We shall keep the basic design of two linked spheres, but allow the spheres' radii to oscillate periodically to produce a changing resistance; this will not only break reciprocality given the correct choice of parameters, but also allow motion and flow. Our eventual swimmer shall resemble Avron's pushmepullyou [36] but with greater freedom to vary its configurations.

This sort of motion (two variable resistances connected by a variable-length link)

Figure 4.1: (a) *Eutreptiella* moving through water by shifting its contents to create localized changes in hydrodynamic resistance, a process known as *metaboly*; picture from [97]. (b) The phased motion of *Chlamydomonas reinhardtii* shows how a reciprocal-seeming motion (moving cilia back and forth) becomes nonreciprocal by changing the resistance (flagella wide and flat on the power stroke versus narrow on the return stroke), thus leading to self-swimming; picture from [98].

(a)

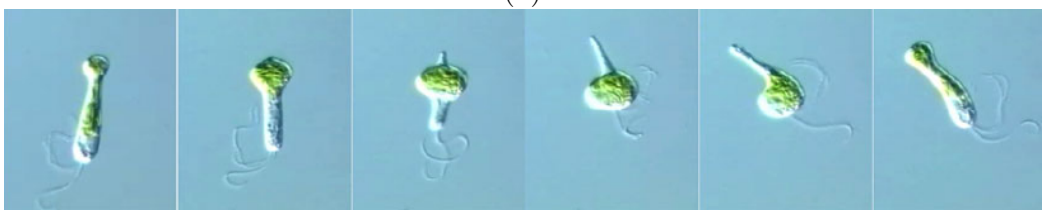

(b)

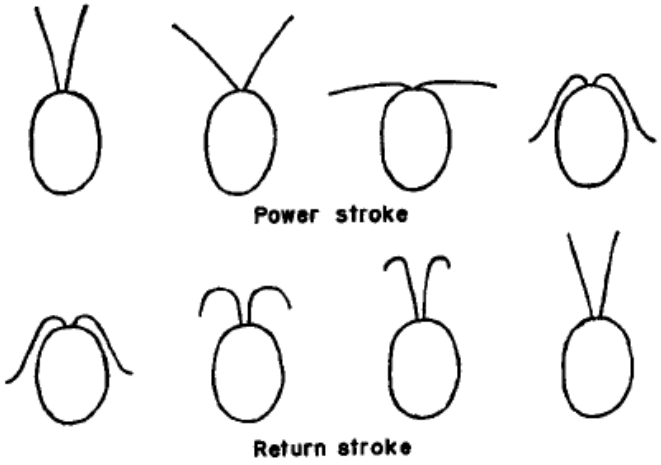

has some precedence in nature; it is not unlike the undulating motion of jellyfish or the human breaststroke. While these are high $\mathcal{R}$ swimmers, metaboly in *Euglena* and *Eutreptiella* [97], shown in Fig. 4.1 (a), is a similar mechanism at lower $\mathcal{R}$. Similarly, the motion of *Chlamydomonas reinhardtii* [98] shows a similar motion in Fig. 4.1 (b), with one resistance (the body) fixed and the other (the oscillating flagella) forming a secondary phased resistance.

4.2.1 A phased-resistance pump

To examine the idea of a variable resistance breaking reciprocality, let us consider the case of an object with a sinusoidally-varying hydrodynamic resistance

$$R(t) = r_0 + \epsilon \sin(\omega t + \phi), \tag{4.1}$$

moving back and forth along a one-dimensional sinusoidal path

$$x(t) = X_0 + \xi \sin(\omega t + \theta). \tag{4.2}$$

Knowing that

$$\frac{\mathrm{d}}{\mathrm{dt}} x = \frac{f(t)}{R(t)}, \tag{4.3}$$

we can solve for the time-varying force, finding

$$f(t) = \xi\omega \left(\epsilon \sin(\omega t + \phi) \cos(\omega t + \theta)\right). \tag{4.4}$$

Orienting this such that $\boldsymbol{x}(t) = x(t)\,\hat{\boldsymbol{N}}$ and $\boldsymbol{f}(t) = f(t)\,\hat{\boldsymbol{N}}$, we can harness our tools of an expanded Oseen tensor and solve for the fluid flow at some point $\boldsymbol{P} = \boldsymbol{X_0} + \boldsymbol{D}$ far from the point of origin $\boldsymbol{x_0}$, time-averaging over a period, and taking the result to leading order in ξ/r to find

$$\boldsymbol{u}(\boldsymbol{P}) = \frac{\epsilon\xi\omega \left(\hat{\boldsymbol{D}} r + \hat{\boldsymbol{N}}\right) \sin(\phi - \theta)}{16\pi\mu D}, \tag{4.5}$$

where r is the projection $\hat{\boldsymbol{D}} \cdot \hat{\boldsymbol{N}}$ as in (2.10). The result is a straightforward $1/D$ flow. This is a simple but pleasant result; the purely reciprocal motion $x(t)$ has been transformed into a nonreciprocal pumping flow by the changing resistance, provided that the difference between the path phase θ and the resistance phase ϕ is not a

multiple of π.

This sort of pump can be easily visualized by imagining moving one's hand back and forth in a thick liquid such as treacle; if the hand is kept closed, its resistance does not change ($\epsilon = 0$) and no net flow is generated. However, if the hand is cyclically opened into a paddle (high resistance) on one side of the stroke and closed into a fist (low resistance) on the return, a net flow will result–unless the peaks of the resistance cycle are reached at the peaks of the motion cycle ($\phi - \theta$ is a multiple of π).

A simple sinusoidally-varying resistance can be mathematically modeled by a sphere with sinusoidally-varying radius $R(t) = 6\pi\mu(a + \lambda \sin(\omega t + \phi))$, where a is the mean radius and λ the variation. This assumption will be used below when we discuss the phased-resistance swimmer. We shall ignore the small flow produced by the changing radius itself in the interest of focusing on the motility and flow produced by the swimming motion, deferring discussion of the flow produced by the changing resistance to Section 4.5.

4.2.2 A phased-resistance swimmer

To generate our swimmer, we simply allow the radii a_1 and a_2 to vary sinusoidally, their cycles differing only in phase, such that the radii and length of the dumbbell vary as

$$a_1(t) = a + \lambda \sin(\omega t + \phi_1), \tag{4.6a}$$

$$a_2(t) = a + \lambda \sin(\omega t + \phi_2), \tag{4.6b}$$

$$L(t) = \ell + \xi \sin(\omega t + \theta). \tag{4.6c}$$

The two spheres are moved by a force pair with magnitude f, such that along the

line of the swimmer

$$\frac{\mathrm{d}}{\mathrm{dt}}x_1 = \frac{f}{R_1} - \frac{f}{\kappa L}, \quad \frac{\mathrm{d}}{\mathrm{dt}}x_2 = \frac{f}{\kappa L} - \frac{f}{R_2}, \tag{4.7}$$

where $\kappa = 4\pi\mu$, $L = L(t)$ represents the changing length of the swimmer, and $R_{1,2} = R_{1,2}(t) = 6\pi\mu a_{1,2}(t)$ represents the time-varying hydrodynamic resistance of the spheres. Knowing that $L(t) = x_2 - x_1$, we can solve for the time-varying force magnitude f and 1D motion of the geometric centre $R_\mathrm{G} = (x_1 + x_2)/2$, yielding

$$f = -\frac{R_1 R_2 \kappa \left(\frac{\mathrm{d}}{\mathrm{dt}}L\right) L}{(R_1 + R_2)\kappa L - 2R_1 R_2}, \tag{4.8}$$

$$\frac{\mathrm{d}}{\mathrm{dt}}R_\mathrm{G} = \frac{(R_2 - R_1)}{2R_1 R_2} f. \tag{4.9}$$

The time-varying quantities R_1, R_2, L involve the three phases ϕ_1, ϕ_2, θ respectively, and the resulting expression for motion of the geometric centre (4.9) is

$$\begin{aligned}\frac{\mathrm{d}}{\mathrm{dt}}R_\mathrm{G} &= [\lambda\xi\omega\ell(\sin(\omega t + \phi_2) - \sin(\omega t + \phi_1))\cos(\omega t + \theta)]/ \\ &\quad 2\Big\{-3\sin(\omega t + \phi_1)\sin(\omega t + \phi_2)\lambda^2 \\ &\quad + (\sin(\omega t + \phi_1) + \sin(\omega t + \phi_2))(\ell\lambda - 3a\lambda) \\ &\quad + 2a\ell - 3a^2\Big\},\end{aligned} \tag{4.10}$$

which is cumbersome to integrate. As long as the variation in radius λ is much smaller than the radius a, it suffices to keep only the leading order terms in λ/a, simplifying this to

$$\frac{\mathrm{d}}{\mathrm{dt}}R_\mathrm{G} = -\frac{\lambda\xi\omega\ell(\sin(\omega t + \phi_2) - \sin(\omega t + \phi_1))\cos(\theta + \omega t)}{2a(2\ell - 3a)}, \tag{4.11}$$

which is more manageable. Integrating and using trigonometric identities to combine

phase terms, we find the time-averaged swimming velocity

$$\boldsymbol{V} = \frac{1}{4}\omega\lambda\left(\frac{\xi}{a}\right)\left(1-\frac{3a}{2\ell}\right)^{-1}\sin\left(\Delta\phi\right)\cos\left(\Delta\theta\right)\hat{\boldsymbol{N}}, \tag{4.12}$$

where $\hat{\boldsymbol{N}}$ is the orientation vector of the swimmer as in (2.4c), and $\Delta\phi$ and $\Delta\theta$ represent the phase differences

$$\Delta\phi := \frac{1}{2}\left(\phi_1-\phi_2\right), \qquad \Delta\theta := \frac{1}{2}\left(\phi_1+\phi_2\right)-\theta. \tag{4.13}$$

Knowing now an expression for the time-varying force f, we can repeat the method used in previous chapters to identify the time-averaged flow produced from the swimmer's spheres at a point $\boldsymbol{P} = \boldsymbol{R}_{\mathrm{G}} + \boldsymbol{D}$ as

$$\boldsymbol{u}\left(\boldsymbol{P}\right) = U\left(\frac{a}{D}\right)^2\left[3r^2-1\right]\hat{\boldsymbol{D}}, \tag{4.14}$$

where $D = |\boldsymbol{D}|$, r is the projection $\hat{\boldsymbol{D}}\cdot\hat{\boldsymbol{N}}$ as in (2.10), and

$$U = \frac{3}{16}\omega\lambda\left(\frac{\xi\ell}{a^2}\right)\left(1-\frac{3a}{2\ell}\right)^{-2}\cos\left(\Delta\phi\right)\sin\left(\Delta\theta\right) \tag{4.15}$$

represents the magnitude of the swimmer's dipolar flow field.

The swimmer thus has a strong dipolar flow, as seen from (4.14)-(4.15), which depends on the phase terms (4.13) as $\sin\left(\Delta\theta\right)\cos\left(\Delta\phi\right)$, while the swimmer's self-swimming speed (4.12) depends on the same phase differences as $\cos\left(\Delta\theta\right)\sin\left(\Delta\phi\right)$.

This is a striking finding. It means that a simple swimmer with fixed dimensions a, λ, ℓ, ξ can, simply by adjusting the *phases* of its resistances and length rather than its *geometry*, choose to swim forward, backward, or not at all, or to adjust its flow to be extensile (pumping fluid out of its ends and in towards its sides), contractile (the reverse), or neutral, generating no dipolar flow at all. Fig. 4.2 shows normalized

Figure 4.2: Map of relative dipolar swimmer self-swimming velocity and flow. (a) Relative self-swimming velocity $\cos(\Delta\theta)\sin(\Delta\phi)$; positive values indicate motion in the direction $\hat{\boldsymbol{N}}$. (b) Relative dipolar flow strength $\sin(\Delta\theta)\cos(\Delta\phi)$; positive values indicate extensile flow.

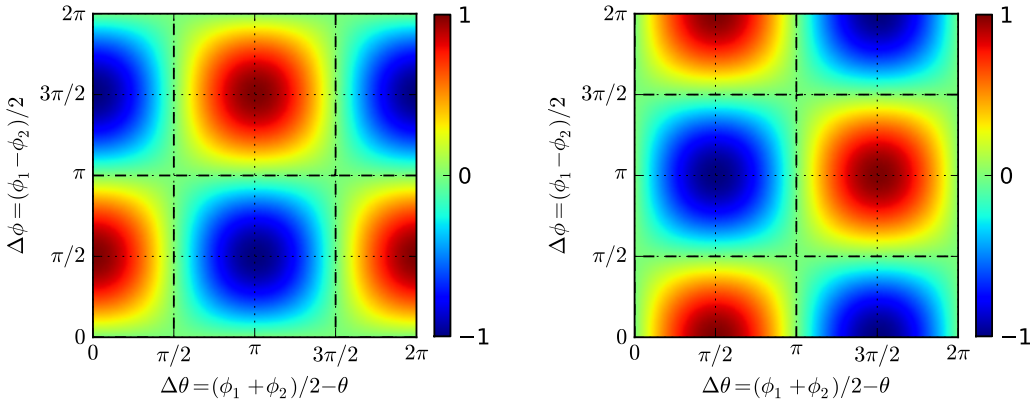

swimmer speed and flow plotted as a function of $\Delta\theta$ and $\Delta\phi$ to give an map of phase space for this dipolar swimmer.

4.3 Changes in method

Finding appropriate values for the small parameters $h^{\sigma\rho}_{mn}$ of the Oseen tensor (2.11) for these two-sphere dipolar swimmers presents a problem. While we discussed the relative merits of geometric centre $\boldsymbol{R}_{\mathrm{G}}$, hydrodynamic centre $\boldsymbol{R}_{\mathrm{H}}$ and "stretch" centre $\boldsymbol{R}_{\mathrm{S}}$ in Fig. 3.2, the cyclic variation of the sphere radii means that these quantities change very differently for two-sphere dipolar swimmers. For example, a "static" dipolar swimmer with zero length variation ($\xi = 0$) but a nonzero resistance variation ($\lambda \neq 0$) would not change its geometric centre $\boldsymbol{R}_{\mathrm{G}}$ but would experience significant variation in hydrodynamic centre $\boldsymbol{R}_{\mathrm{H}}$.

Further, under examination, while the time-averaged speed of the swimmer along its orientation vector $\hat{\boldsymbol{N}}$ is given by (4.12), the motion of its geometric centre under-

goes a periodic variation such that

$$\frac{\mathrm{d}}{\mathrm{dt}}\boldsymbol{R}_{\mathrm{G}} = \boldsymbol{V}\left(t + \frac{\sin\left(2\omega t + \Delta\theta\right)}{2\omega\cos\left(\Delta\theta\right)}\right), \tag{4.16}$$

where $\boldsymbol{V}$ is the linear time-averaged velocity of (4.12), and the second term represents a small sinusoidal variation at twice the frequency of oscillation. However, this variation is quite small, and for simplicity we shall proceed for both source and target swimmer using $\boldsymbol{R}_{\mathrm{G}}$ as the centre of our swimmer, assuming that during a single cycle the dumbbell's ends move approximately symmetrically about its center for purposes of interactions. This enables us to find the dominant lowest-order terms for pair interactions, but the motion of the geometric centre poses difficulties for higher-order corrections.

The magnitude of the applied force pair is significantly more complex than for static dumbbells, where it was neatly approximated by a sinusoidal variation. Here, the force varies with hydrodynamic resistance, and using (4.9), to leading order in λ/a and ξ/ℓ

$$f = -\frac{6\pi\xi\mu\omega\ell\cos\left(\theta+\omega t\right)\left[\ell\lambda\left(\sin\left(\omega t+\phi_2\right)+\sin\left(\omega t+\phi_1\right)\right)+2a\ell-3a^2\right]}{\left(2\ell-3a\right)^2}. \tag{4.17}$$

4.4 Pair interactions

Going through the same calculation for swimmer pair interactions as in Chapters 2 and 3, we must add in the ability of these dipolar swimmers to self-locomote. We find, to the lowest-order, translation of the geometric centre,

$$\frac{\mathrm{d}}{\mathrm{dt}}\boldsymbol{R}^{\sigma}_{\mathrm{G}} = V\hat{\boldsymbol{N}}^{\sigma} + \sum_{\rho\neq\sigma} U^{\rho}\left(\frac{a}{|D^{\sigma\rho}|}\right)^2\left[3r^2-1\right]\hat{\boldsymbol{D}}^{\sigma\rho}, \tag{4.18}$$

Table 4.1: Summary of dominant (lowest-order) swimmer interaction features.

Swimmer type	Translation	Rotation
Symmetric Dumbbell	D^{-4}, active	D^{-5}, active
Asymmetric Dumbbell	D^{-3}, active	D^{-4}, active
Phased Dipolar	D^{-2}, passive	D^{-3}, passive

and rotation,

$$\frac{\mathrm{d}}{\mathrm{dt}}\hat{\boldsymbol{N}}^{\sigma} = 3\sum_{\rho\neq\sigma}\left(\frac{U^{\rho}}{a}\right)\left(\frac{a}{|D^{\sigma\rho}|}\right)^{3}\left(\hat{\boldsymbol{D}}^{\sigma\rho} - \hat{\boldsymbol{N}}^{\sigma}s\right)\left(5rs^{2} - 2qs - r\right), \tag{4.19}$$

where again (r, s, q) are the projections (2.10). It is important to realize that both the self-swimming speed V and the dipolar flow magnitude U are dependent on phase differences $\Delta\theta$ and $\Delta\phi$ as displayed in Fig. 4.2.

Once again, our examination of swimmer pair interactions has revealed some interesting features. Most obvious is the presence of the self-swimming term $V\hat{\boldsymbol{N}}$ in (4.18), a term which by definition does not depend on other swimmers in the suspension and thus does not scale with distance. Secondly, there is a notable absence of an inter-swimmer phase difference term as we had with the dumbbells; while the interactions between reciprocal-motion swimmers were dominated by so-called *active* terms [40] depending on a phase difference, the interactions between swimmers which generate their own flow fields are dominated by *passive* terms which depend on *intraswimmer* phase differences ($\Delta\theta$,$\Delta\phi$) rather than any *interswimmer* phase differences. Lastly, the presence of a net dipolar term has again changed the scaling of pair interactions with inter-swimmer distance as shown in Table 4.1.

So long as $U \neq 0$ for swimmers in a suspension (i.e., so long as their intraswimmer phase differences are such that the quantity $\cos(\Delta\theta)\sin(\Delta\phi)$ is not near 0), Eqns. (4.18) and (4.19) dominate interactions. In the absence of flow, these passive terms vanish and higher-order active terms are significant. However, in Subsection 4.5.1 we shall show that the changing geometry of a resistance could generate a

more complex flow in the near-field which could dominate when the dipolar flow is minute or absent. Since this simple two-sphere model abstracts this away, we shall restrict comparison with simulations to those cases where the generated flow will be significant. Additionally, the large impact of $\Delta\theta$ and $\Delta\phi$ on swimmer motility and flow presents a potential problem with simulations. Since the simulations use spheres linked by potential springs of periodically-changing length (2.3), an insufficiently-stiff spring constant k_0 can cause small amounts of phase lag. While this was a potential problem with the reciprocal dumbbells, the symmetry of their motion mitigated it; it is more problematic here, as the changing resistances can cause, for example, swimmers with parameters designed for zero motility to self-swim, or swimmers with parameters for zero flow to advect fluid, as the phase lag changes $\Delta\theta$ and $\Delta\phi$. Due to these difficulties with numeric simulations, our comparisons will be restricted to swimmers which are self-motile and generate flow, thus we will look only at cases where $U \neq 0, V \neq 0$. The results are summarized in Fig. 4.3, where four test cases are shown, with very good agreement between analytics and simulations.

4.5 Exploring the details of resistance

In Sections 4.2-4.4, we examined the effect of moving variable hydrodynamic resistances without considering how changing the resistance itself will generate a flow. Here we wish to explore the details of that resistance change in the context of a simple pump where the variable resistances are produced by fixed-radius colloids. We find that adding the details of the changing resistance adds a quadrupolar (D^{-3}) term onto the flow field produced by movement of the resistance. This is useful when considering the three-sphere swimmer [35], which has a quadrupolar flow field at close range [38].

Implementing a phased dipolar swimmer using variable-length dumbbells is easy

Figure 4.3: Dipolar swimmer interactions for four cases of nonzero flow and motion. Swimmer parameters $\ell = 5\mu\text{m}$, $\xi = 0.1\ell$, $a = 0.2\ell$, $\lambda = 0.1\ell$. Phase parameters for each case are shown in accompanying table. Results show excellent agreement with simulation.

Subfigure	Swimming Direction	Flow	$\Delta\theta$	$\Delta\phi$
a	Right	Extensile	$\pi/4$	$\pi/4$
b	Right	Contractile	$\pi/4$	$3\pi/4$
c	Left	Extensile	$3\pi/4$	$\pi/4$
d	Left	Contractile	$3\pi/4$	$3\pi/4$

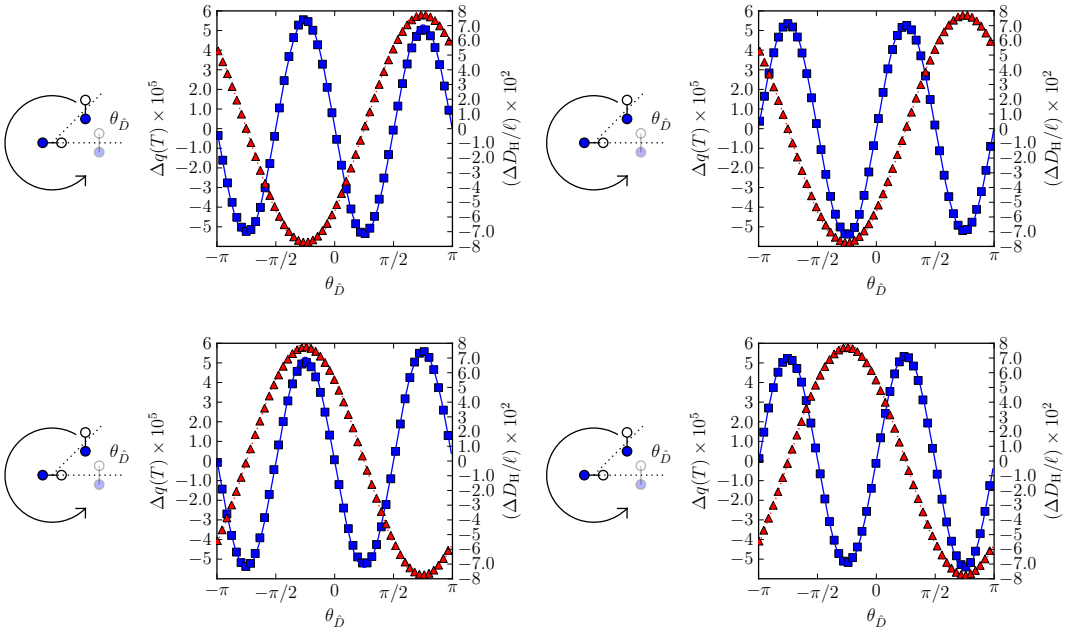

Figure 4.4: A two-sphere pump; the direction and intensity of flow are determined by the resistance phase ϕ and the path phase θ.

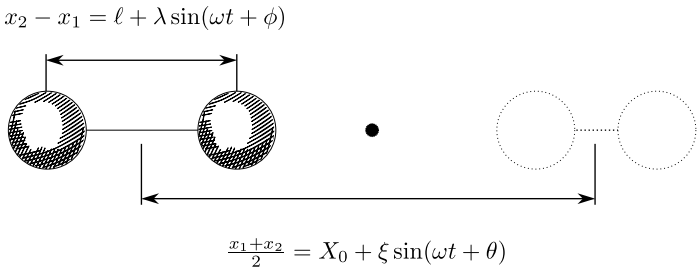

using our simulation, but very difficult to treat analytically as the interactions between four beads become complex. We shall instead introduce the idea of an overlaid quadrupolar flow by discussing a simpler mechanism, a pump constructed of an externally-forced dumbbell which changes its length periodically.

4.5.1 A "dumbbell pump"

The Oseen tensor formalism shows that a point force on a low Reynolds number fluid advects fluid around it. A dumbbell composed of two spheres subject to an external force along its axis thus exhibits a hydrodynamic resistance dependent on its length, as the force on each bead advects fluid at the location of the other bead, helping it move. This means that a dumbbell with a sinusoidally-oscillating length comprises a sinusoidally-oscillating hydrodynamic resistance (Appendix C).

We therefore posit a simple two-sphere pump as shown in Fig. 4.4, where the positions of the two spheres x_1 and x_2 are determined by the changing length of the dumbbell and the motion of the dumbbell along a cyclic path. We shall calculate the net flow both by modeling the system as a point particle with varying resistance and by modeling it as two separate spheres, and compare the resultant flow from each.

4.5.2 Modeling the dumbbell pump as a point particle

We first view the pump as a point particle moving as

$$\boldsymbol{x} = \boldsymbol{X}_0 + (\xi \sin(\omega t + \theta))\, \hat{\boldsymbol{N}}, \tag{4.20}$$

with the varying resistance of an oscillating dumbbell from Appendix C,

$$R = \frac{24\pi a \ell \mu}{2\ell + 3a} + \frac{72\pi a^2 \mu \lambda}{(2\ell + 3a)^2} \sin(\omega t + \phi). \tag{4.21}$$

Since the velocity of a particle at zero $\mathcal{R}$ is proportional to its resistance as $\frac{\mathrm{d}}{\mathrm{dt}} x = F/R$, taking the derivative and solving for force gives

$$F = \frac{24\pi a \mu \omega \cos(\omega t + \theta)\, \xi\, (3a\lambda \sin(\omega t + \phi) + 2\ell^2 + 3a\ell)}{(2\ell + 3a)^2}. \tag{4.22}$$

We now have the position of the particle (4.20) and the time-varying force applied (4.22). Using the Oseen tensor, we find the instantaneous flow at some point $\boldsymbol{P} = \boldsymbol{X}_0 + \boldsymbol{D}$, to leading order in powers of ξ/D and order two in powers of a/ℓ,

$$\boldsymbol{u}(\boldsymbol{P}) = \frac{3a\omega\xi\, (3a\lambda \sin(\omega t + \phi) + 2\ell^2 - 3a\ell) \cos(\omega t + \theta)}{4\ell^2 D} \left(\hat{\boldsymbol{D}} r + \hat{\boldsymbol{N}} \right), \tag{4.23}$$

which, time-averaged over a period, becomes

$$\boldsymbol{u}_{ave}(\boldsymbol{P}) = \frac{9}{8} \left(\frac{a}{l} \right)^2 \omega \sin(\phi - \theta)\, \xi\lambda \left(\frac{1}{D} \right) \left(\hat{\boldsymbol{D}} r + \hat{\boldsymbol{N}} \right). \tag{4.24}$$

This a straightforward $1/D$ Stokeslet as with (4.5).

4.5.3 Modeling the dumbbell pump as two spheres

Modeling the system as two spheres separated by a varying distance and a prescribed path for the dumbbell's geometric centre

$$x_2 - x_1 = \ell + \lambda \sin(\omega t + \phi), \tag{4.25a}$$

$$\frac{x_1 + x_2}{2} = X_0 + \xi \sin(\omega t + \theta), \tag{4.25b}$$

we can decompose the force on each sphere into f_{ext}, the applied external force which works on both spheres identically, and f_{res}, a force pair which works in opposite directions on each sphere to change the dumbbell's resistance, such that $f_1 = f_{ext} + f_{res}$, $f_2 = f_{ext} - f_{res}$. This enables us to write the motion of each sphere as

$$\frac{\mathrm{d}}{\mathrm{dt}} x_1 = \frac{f_{ext} - f_{res}}{4\pi\mu(x_2 - x_1)} + \frac{f_{ext} + f_{res}}{6\pi\mu a}, \tag{4.26a}$$

$$\frac{\mathrm{d}}{\mathrm{dt}} x_2 = \frac{f_{ext} + f_{res}}{4\pi\mu(x_2 - x_1)} + \frac{f_{ext} - f_{res}}{6\pi\mu a}. \tag{4.26b}$$

Combining (4.26) with (4.25b), we can find expressions for f_{ext} and f_{res}, use (4.25) to determine linear variations for our expanded tensor, and integrate to find expressions for the first three terms of the expansion. We find, for the time-averaged fluid flow at some position $\boldsymbol{P} = \boldsymbol{X}_0 + \boldsymbol{D}$, simplified in terms of λ/ℓ, a/ℓ, and ξ/D,

$$\begin{aligned}\boldsymbol{u}_{ave}(\boldsymbol{P}) = &\frac{9}{8}\left(\frac{a}{\ell}\right)^2 \omega \sin(\phi - \theta)\, \xi\lambda \times \\ &\left\{ \left(\frac{1}{D}\right)\left(\hat{\boldsymbol{D}} r + \hat{\boldsymbol{N}}\right) \right. \\ &\left. - \frac{3}{8}\left(\frac{\ell}{D}\right)^2 \left(\frac{1}{D}\right)\left(\hat{\boldsymbol{D}}\left(15r^3 - 3r\right) - \hat{\boldsymbol{N}}\left(3r^2 - 1\right)\right) \right\}.\end{aligned} \tag{4.27}$$

There are some interesting features of this flow. The primary contribution, from the second line of (4.27), is the same Stokeslet flow as in (4.24). However, modeling

both spheres of the dumbbell has added a relatively strong quadrupolar contribution (third line of (4.27)) which is comparable to the primary flow at distances of about $D^2 \sim 3\ell^2/8$, or $D \sim 0.6\ell$ and is evidently due to the change in geometry of the dumbbell comprising the resistance.

There are a great many ways to visualize fluid flow, from concepts used in painting [99] to distortion of a background image [100] or calculation of streamlines [101]. We use the method of line integral convolution [102, 103], which shows structure and critical points of a flow, as a good compromise between ease of implementation and resultant images. A study of various visualization methods [104] showed errors in identifying features of flow using line integral convolution alone, as it does not show direction of flow, so we overlay a grid of arrows showing local flow direction. Fig. 4.5 shows the flow (4.27) in the immediate vicinity of the dumbbell pump, with the quadrupolar contribution visible in the centre of the graph. This shows us that the details of the changing resistance *can* matter, but that in the presence of significant flow can be neglected except very near to the swimmer itself.

4.6 Comparison with the three-sphere swimmer

Having described the phased dipolar swimmer, and shown that a moving oscillating dumbbell can perform as a varying resistance giving quadrupolar flow, we now show that the oft-studied three-sphere swimmer of Najafi and Golestanian [35] shown in Fig. 1.2 may be itself an instance of a phased dipolar swimmer, explaining some aspects of its motion and flow. The original four-stroke model can be recast into sinusoidal motion [38, 40, 39] for easier analysis, such that the front and back legs change length as

$$L_{1,2} \;=\; \ell + \xi_{1,2} \sin\left(\omega t + \phi_{1,2}\right). \tag{4.28}$$

Figure 4.5: Direction of flow from a two-sphere pump. (a) Stokes $1/D$ flow from the point-particle analysis (4.24). (b) Flow from the pump modeled as a dumbbell showing quadrupolar contribution near the centre. Parameters were chosen to show a quadrupolar contribution; $\ell = 1$, $a = 0.1\ell$, $\lambda = 0.1\ell$, $\xi = \ell$, $\phi - \theta = \pi/2$.

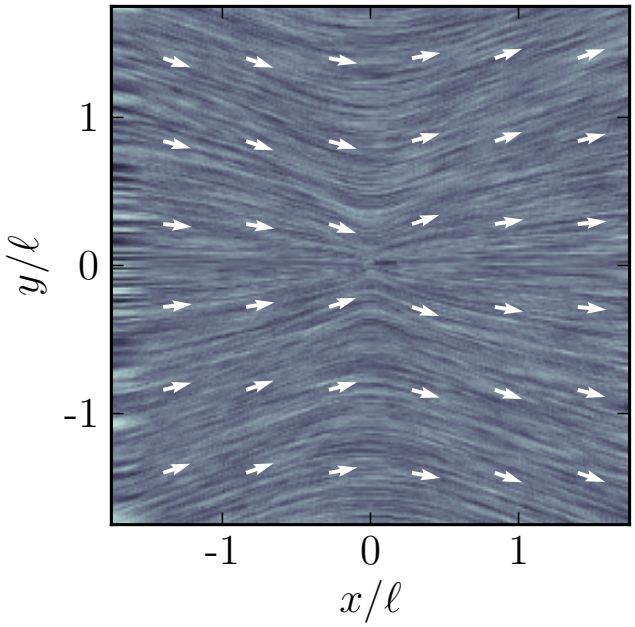

(a)

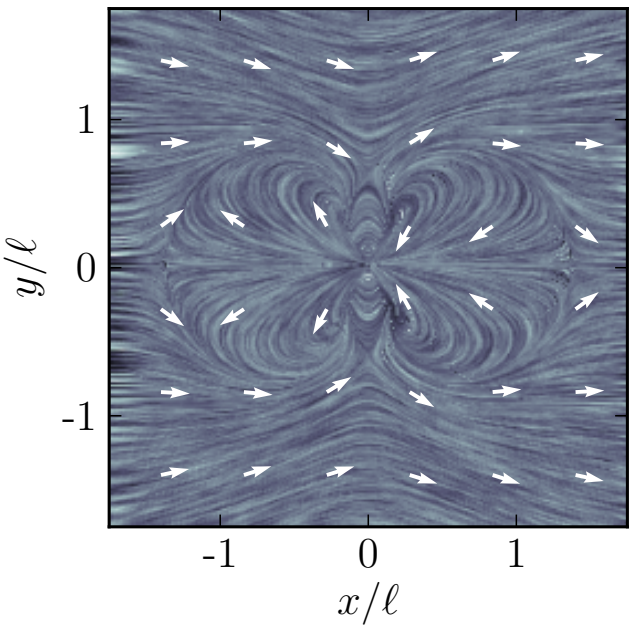

(b)

Alexander et al. [38] found that the speed of such a sinusoidal three-sphere swimmer scaled with $\sin(\phi_1 - \phi_2)$ and thus was at a maximum when the phase difference between the two lengths was $\phi_1 - \phi_2 = \pi/2$, as compared to the phased dipolar swimmer, which has a maximum speed when the phase difference between the two ends is $\phi_1 - \phi_2 = \pi$. They also showed that the dipolar contribution of the three-sphere swimmer's fluid flow was extensile when $\xi_1 > \xi_2$, contractile when $\xi_1 < \xi_2$, and vanished when $\xi_1 = \xi_2$.

We can gain some insight into these observations by taking the middle sphere of the three-sphere swimmer and separating it into a fixed dumbbell with separation ε as shown in Fig. 4.6, with the aim of viewing the three-sphere swimmer as an instance of the phased dipolar swimmer described previously. The varying-length dumbbells of the two legs now form sinusoidally-oscillating resistances, and the line between the centres of the two legs can be seen as an oscillating link. We can now calculate ℓ, ξ, θ for the body link $L(t)$ by noting that

$$\begin{aligned} L(t) &= \varepsilon + \frac{L_1(t) + L_2(t)}{2} \\ &= \varepsilon + \ell_{leg} + \frac{\xi_1 \sin(\omega t + \phi_1) + \xi_2 \sin(\omega t + \phi_2)}{2}. \end{aligned} \tag{4.29}$$

The sinusoidal components on the right of (4.29) can be combined using a trigonometric identity and, using the definition of $\Delta\phi$ from (4.13), we find

$$\begin{aligned} L(t) &= \varepsilon + \ell_{leg} + \frac{\sqrt{2\xi_1\xi_2 \cos(2\Delta\phi) + \xi_2^2 + \xi_1^2}}{2} \\ &\quad \times \sin\left(\omega t + \tan^{-1}\left(\frac{\xi_1 \sin(2\Delta\phi)}{\xi_1 \cos(2\Delta\phi) + \xi_2}\right) + \phi_2\right). \end{aligned} \tag{4.30}$$

Comparing (4.30) to the body length $L(t)$ in (4.6c) and using the definition of $\Delta\theta$ from (4.13), we can say that the three-sphere swimmer is somewhat analogous to a

Figure 4.6: The three-sphere swimmer can be interpreted as a phased dipolar swimmer if the centre sphere is replaced by a fixed dumbbell. The two oscillating legs form sinusoidal resistances, and the line joining their centres forms the body link length $L(t)$, not unlike Eqns. (4.6). The phased dipolar "body" parameters ℓ, ξ, and θ (and thus the phase parameters $\Delta\phi$ and $\Delta\theta$) depend on the three-sphere swimmer's "leg" parameters ℓ_{leg}, $\xi_{1,2}$, $\phi_{1,2}$, where ℓ_{leg}, $\xi_{1,2}$, $\phi_{1,2}$ are the mean leg length, amplitude of variations, and phases of the individual leg oscillations. The two dumbbells comprising the changing resistances can now be modeled as sinusoidally varying spheres, where the radii and variation of the spheres are calculated using the resistance of a sinusoidally-varying dumbbell (C.5).

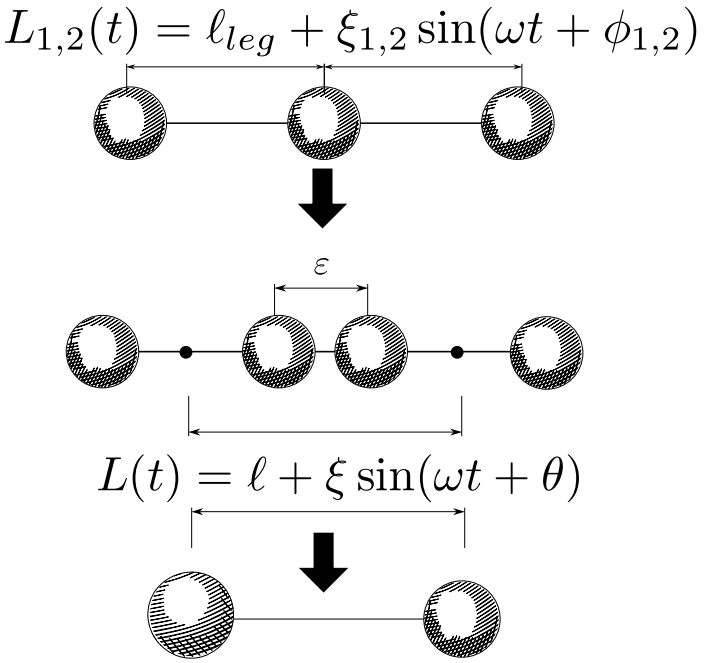

phased dipolar swimmer with parameters

$$\ell = \varepsilon + \ell_{leg}, \tag{4.31a}$$

$$\xi = \frac{\sqrt{2\xi_1\xi_2\cos(2\Delta\phi) + \xi_2^2 + \xi_1^2}}{2}, \tag{4.31b}$$

$$\Delta\theta = \tan^{-1}\left(\frac{\xi_1\sin(2\Delta\phi)}{\xi_1\cos(2\Delta\phi) + \xi_2}\right) - \Delta\phi. \tag{4.31c}$$

Eqns. (4.31) show how, for the three-sphere swimmer, both the amplitude of the body length variation ξ and the path phase difference $\Delta\theta$ depend on the resistance phase difference $\Delta\phi$.

4.6.1 Phase parameters and effect on flow

The phased dipolar swimmer speed (4.12) depends on $\xi\sin(\Delta\phi)\cos(\Delta\theta)$, and we can now see why the three-sphere swimmer swims best at $\Delta\phi = \pi/4$ instead of $\Delta\phi = \pi/2$ as one would expect. For a symmetric ($\xi_1 = \xi_2 = \xi_{leg}$) three-sphere swimmer, the path phase difference simplifies to $\Delta\theta = 0$, and the body length variation simplifies to $\xi = \xi_{leg}\cos(\Delta\phi)$. The resultant speed varies as $\propto \xi_{leg}\sin(2\Delta\phi)/2$, maximized at the parameters $\Delta\phi = \pi/4$, $\Delta\theta = 0$ on the map of phase space shown in Fig. 4.2. Phased dipolar swimmers with these parameters have no dipolar flow, reflecting the behaviour of symmetric three-sphere swimmers.

Having located the symmetric three-sphere swimmer in phase space, what are the effects of asymmetry on speed and flow? We note from (4.31) that changing the relative variations ξ_1, ξ_2 affects the path variation ξ and phase difference $\Delta\theta$. At the optimal resistance phase difference $\Delta\phi = \pi/4$, we find

$$\xi = \frac{\sqrt{\xi_1^2 + \xi_2^2}}{2}, \tag{4.32a}$$

$$\Delta\theta = \tan^{-1}\left(\frac{\xi_1}{\xi_2}\right) - \frac{\pi}{4}. \tag{4.32b}$$

Since the magnitude of the phased dipolar swimmer's fluid flow (4.15) is proportional to $\xi \cos(\Delta\phi) \sin(\Delta\theta)$, making the back leg longer than the front ($\xi_1 > \xi_2$) shifts the path phase difference $\Delta\theta$ to be slightly positive, into the regime of slight extensile dipolar flow on Fig. 4.2. Similarly, when the back leg is shorter ($\xi_1 < \xi_2$), the phase difference $\Delta\theta$ becomes slightly negative, into the regime of slight contractile dipolar flow.

4.6.2 Comparison of speeds

Knowing that a dumbbell oscillating about its length can be modeled as a point particle with varying resistance similar to a sphere with a varying radius, we shall compare the speed of a symmetric three-sphere swimmer modeled as two varying dumbbells with that of an actual three-sphere swimmer. We substitute the radius a and variation λ in (4.12) with an equivalent radius and variation found by dividing the resistance of an oscillating dumbbell (4.21) by $6\pi\mu$. Using the phase parameters $\Delta\phi = \pi/4$, $\Delta\theta = 0$ of a symmetric three-sphere swimmer, and the lengths $\ell = \ell_{leg} + \varepsilon$, $\xi = \xi_{leg}/\sqrt{2}$, we find the time-averaged speed of the equivalent phased dipolar swimmer to be

$$V = \frac{3a\xi_{leg}^2 \omega \left(\ell_{leg} + \varepsilon\right)}{8\ell_{leg}\left(2\ell_{leg}^2 + 2\varepsilon\ell_{leg} - 3a\ell_{leg} + 3a\varepsilon\right)}, \tag{4.33}$$

which to leading order in a/ℓ_{leg} is

$$V = \left(\frac{3}{16}\right)\left(\frac{\xi_{leg}}{\ell_{leg}}\right)^2 a\omega. \tag{4.34}$$

For comparison, we use formula (11) given in [38] for the distance traveled during a cycle by the three-sphere swimmer, divided by a period to give time-averaged speed. With symmetric parameters $\xi_r = \xi_f = \xi_{leg}$, and the leg phase difference $\phi = \pi/2$, this

becomes

$$
\begin{aligned}
V &= \frac{a\omega}{6\sqrt{2}\left(\ell_{leg}-\xi_{leg}\right)\left(\ell_{leg}+\xi_{leg}\right)\sqrt{2\ell_{leg}^2-\xi_{leg}^2}} \\
&\quad\times\Bigg\{4\sqrt{2}\ell_{leg}\sqrt{\ell_{leg}^2-\xi_{leg}^2}\sqrt{2\ell_{leg}^2-\xi_{leg}^2} \\
&\qquad-\left(\ell_{leg}^2-\xi_{leg}^2\right)\left(3\sqrt{2}\sqrt{2\ell_{leg}^2-\xi_{leg}^2}+2\ell_{leg}\right)\Bigg\},
\end{aligned}
\tag{4.35}
$$

which to order $\left(\xi_{leg}/\ell_{leg}\right)^2$ is

$$
V=\left(\frac{7}{24}\right)\left(\frac{\xi_{leg}}{\ell_{leg}}\right)^2 a\omega. \tag{4.36}
$$

Eqns. (4.34) and (4.36) are very similar, suggesting that the mechanism by which the three-sphere swimmer moves is the same as the more abstract phased dipolar swimmer described in this chapter. The difference in prefactor between (4.34) and (4.36) accounts for the details of swimmer geometry which have changed in the transformation from three-sphere swimmer to phased dipolar swimmer.

4.7 Discussion

We have introduced an abstract model swimmer, the phased dipolar swimmer, which propels itself by means of two varying resistances connected by a varying length. The varying phases allow a swimmer with fixed geometry to move in either direction (or to not move at all) and generate a dipolar flow field which can be extensile, contractile, or neutral.

The pair interactions experienced by these swimmers are dominated by self-swimming and net flow, with no active terms dependent on interswimmer phase difference, and which scale as D^{-2} for translation and D^{-3} for rotation. This is in contrast to the active interactions of the dumbbells in Chapters 2 and 3, which exhibited no self-

motility and had interactions only at higher orders. The lack of active terms for the phased dipolar swimmer interactions (so long as parameters are chosen such that the dipolar flow is not zero) means that they are also of interest in numerical simulation as much more generic swimmers, since phase differences between swimmers become unimportant and a time-averaged interaction which neglects individual swimmer phase is sufficient.

However, we also noted that the details of the resistance can be important in the near field, by demonstrating the flow fields produced by a simple pump, modeled both as a point particle with varying resistance and as a variable-length dumbbell. Adding the details of the resistance produced a quadrupolar (D^{-3}) flow in the near field.

The three-sphere swimmer of Najafi and Golestanian shows many features of a phased dipolar swimmer confined to a small neighborhood around the point $\Delta\phi = \pi/4$, $\Delta\theta = 0$ in the phase space shown in Fig. 4.2. With the observation that a moving variable-length dumbbell generates a quadrupolar flow in the near field, we submit that the pair interactions of the three-sphere swimmer, which are dominated by quadrupolar active interactions at moderate range [38], are a somewhat special case because the dipolar flow of the three-sphere swimmer is weak when it exists at all.

That the Avron pushmepullyou swimmer and the Najafi-Golestanian three-sphere swimmer both derive from a more abstract phased dipolar swimmer is interesting given the many discussions of efficiency surrounding both. Avron [36] claimed much greater distance traveled per stroke for pushmepullyou compared to the three-sphere swimmer, but this is partly due to the small varying resistance of dumbbells versus a sphere with varying radius, partly due to the restriction of the three-sphere swimmer to its phase neighborhood, and partly due to the dependence of the three-sphere swimmer's body length change ξ to its leg lengths $\xi_{1,2}$. Alouges et al. [42] examined optimal strokes for the three-sphere swimmer and pushmepullyou, but kept the as-

sertion that the pushmepullyou swimmer must change radii in such a way that the total mass of the end spheres remains constant. This concept precludes the idea of varying resistances which do not transfer mass between them, such as variable-length dumbbells or spheroids which change their aspect ratio from oblate to prolate in a periodic fashion. The phased dipolar swimmer provides a higher abstract framework to examine these concepts. It would be interesting to examine a more rigorous evaluation of the three-sphere swimmer in the phased-dipolar swimmer framework, or to pursue swimmers where one resistance is fixed as with the motion of *C. reinhardtii*. Additionally, higher-order corrections exist for phased dipolar swimmers with minimal flow or self-motility, and may be worth pursuing in future work.

We shall now examine the effects of both the abstract phased dipolar swimmer (with dipolar flow) and the symmetric three-sphere swimmer (with quadrupolar flow) on a passive tracer particle.

Chapter 5

Motion of a tracer particle

5.1 Motivation

In Chapter 4, we discussed swimmers that, with suitable parameters, both imparted a net fluid flow to the environment and propelled themselves through that environment, but our discussion was limited to short-term pair interactions between active swimmers. We now direct our attention to the effect of a swimmer's long-term passing on a passive tracer particle's path, in contrast to our previous chapters with immediate scattering of active swimmers.

Scattering processes are ubiquitous in nature, ranging from elementary particle collisions at subatomic scales to gravitational encounters in galaxies or galactic clusters. Traditionally, scattering experiments have played an important role in elucidating the interactions between 'non-living' physical objects. Nowadays, modern experimental techniques allow us to track the motion of individual microorganisms [18, 105, 5, 106], as beautifully illustrated by recent high-speed microscopy observations of *Volvox* [15] and *Chlamydomonas reinhardtii* [107, 108]. These and similar experiments on colloidal systems [52] suggest that it should be possible in the near future to systematically study the effective hydrodynamic interaction forces gener-

ated by algae, bacteria or artificial microswimmers [53, 56] through suitably designed 'biophysical' scattering experiments.

Additional motivation for studying swimmer-tracer scattering comes from recent experiments by Leptos et al. [107], who observed that a passive tracer particle exhibits non-Gaussian diffusion when surrounded by a dilute suspension of self-motile *Chlamydomonas reinhardtii* algae. Qualitatively, the anomalous diffusive behavior arises because the algae modify the velocity field of the fluid, thereby occasionally accelerating the tracer particle to relatively large velocities. A better understanding of the underlying elementary scattering processes is a key step en route to deriving the corresponding generalized diffusion equation.

But what features should be observable when a small colloidal tracer particle is scattered by an artificial or natural microswimmer? Specifically, we would like to address the following problems: How does the swimmer's flow field (dipolar or quadrupolar) affect the path of a tracer particle? Is it sufficient to consider an effective time-averaged description in order to correctly predict the tracer trajectories, or is it necessary to use a time-resolved model that captures the details of the swimming stroke? How does Brownian motion, which plays a non-negligible role for (sub-)micron-sized colloidal particles, affect the tracer dynamics? To answer these questions, we will compare both analytically and numerically the dynamics of a tracer in the presence of various simplified model swimmers.

5.2 A Langevin model of swimmer-tracer scattering

We consider the motion $\boldsymbol{x}(t)$ of a passive colloidal tracer particle in a fluid due to the presence of an active object (a 'swimmer' which here which may be an externally forced colloid, an artificial microswimmer, or a microorganism) represented by a phase space coordinate vector $\boldsymbol{\Gamma}(t)$. For a spherical colloid with position vector $\boldsymbol{X}(t)$ and

velocity $\dot{\boldsymbol{X}}(t)$, for example, $\boldsymbol{\Gamma}(t)$ is simply given by $\boldsymbol{\Gamma}(t) = \left(\boldsymbol{X}(t), \dot{\boldsymbol{X}}(t)\right)$, but for more complex objects such as the multisphere swimmers in Chapter 4 and [38, 41] $\boldsymbol{\Gamma}$ is comprised of all the coordinates necessary to uniquely specify the swimmer's motion. We assume that the tracer particle, to good approximation, does not affect the swimmer's motion and is purely diagnostic, i.e., $\boldsymbol{\Gamma}(t)$ is taken to be independent of $\boldsymbol{x}(t)$.

In principle, when studying the scattering of a tracer particle by a self-swimming object, one can distinguish (at least) two different approaches:

1. One can numerically simulate the exact time-resolved motion of the tracer particle in the oscillatory flow field of the swimmer.

2. One can try to compute the approximate mean motion of the tracer particle in a time-averaged (or stroke-averaged) effective flow field of the swimmer.

Using the mechanisms described earlier, we shall compare the results from both methods for multi-sphere swimmer models [109, 38]; in the coarse-grained approach, we will simply approximate the swimmer state by $\boldsymbol{\Gamma}(t) = \left(\boldsymbol{X}(t), \dot{\boldsymbol{X}}(t)\right)$, and the swimmer will be assumed to move at constant velocity $\dot{\boldsymbol{X}}(t) \equiv \boldsymbol{V}$ along the straight line

$$\boldsymbol{X}(t) = \boldsymbol{X}_0 + t\boldsymbol{V}, \tag{5.1}$$

where the effective stroke-averaged swimmer velocity $\boldsymbol{V}$ results from the microscopic swimmer dynamics.

Assuming we know the velocity field $\boldsymbol{v}(\boldsymbol{x}(t)|\boldsymbol{\Gamma}(t))$ generated by a given swimmer configuration $\boldsymbol{\Gamma}(t)$, we can model the motion of a small tracer particle by the overdamped Langevin equation

$$\dot{\boldsymbol{x}}(t) = \boldsymbol{v}(\boldsymbol{x}(t)|\boldsymbol{\Gamma}(t)) + (2D_0)^{1/2}\boldsymbol{\zeta}(t). \tag{5.2}$$

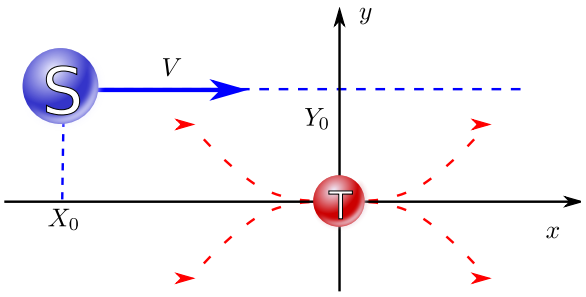

Figure 5.1: Swimmer-tracer scattering initial conditions. The swimmer (blue) starts at $\boldsymbol{X}_0 = (X_0, Y_0, 0)$ and moves with velocity $\boldsymbol{V} = (V, 0, 0)$ parallel to the $x-$axis. The trajectory of the tracer (red), initially located at $\boldsymbol{x}(0) = (0, 0, 0)$, depends on the flow field generated by the moving swimmer.

This equation is valid in the Stokes regime, which is realized to good approximation under typical experimental conditions [15, 107, 108]. The second contribution on the rhs. of (5.2) represents Gaussian white noise $\boldsymbol{\zeta}(t) = (\zeta_i(t))$ describing thermal fluctuations in the fluid and characterized by

$$\langle \zeta_i(t) \rangle = 0 \qquad \langle \zeta_i(t)\, \zeta_j(s) \rangle = \delta_{ij} \delta(t - s)\,. \tag{5.3}$$

For a spherical tracer particle of radius a_0, the thermal diffusion constant D_0 is given by the Stokes formula

$$D_0 = k_B T / \gamma_0 = k_B T / (6\pi\mu a_0)\,. \tag{5.4}$$

For example, considering $a_0 = 1\mu$m and water at room temperature $T = 25°$ with viscosity $\mu = 10^{-3}\text{kgm}^{-1}\text{s}^{-1}$ and $k_B T = 4.11 \times 10^{-21}\text{kgm}^2\text{s}^2$, we have $D_0 = 0.22\mu\text{m}^2/\text{s}$.

We intend to analyze swimmer-tracer scattering processes for well-defined, reproducible initial conditions. To this end, we choose the coordinate system such that the spherical tracer particle is initially located at the origin, $\boldsymbol{x}(0) = \boldsymbol{0}$. The swimmer (with some characteristic dimension A) starts at $\boldsymbol{X}_0 = (X_0, Y_0, 0)$ with $|Y_0| > a_0 + A$ and moves in the $(z = 0)$ plane with an average velocity $\boldsymbol{V} = (V, 0, 0)$ parallel to the x-axis, as in Fig. 5.1.

To understand the motion of the tracer in the velocity field $\boldsymbol{v}(\boldsymbol{x}(t)\,|\boldsymbol{\Gamma}(t))$ of an externally-driven or self-motile object, it is convenient for a simpler notation to define

the distance vector between tracer and swimmer by

$$\boldsymbol{r}\left(t\right)=\boldsymbol{x}\left(t\right)-\boldsymbol{X}\left(t\right), \tag{5.5}$$

and to introduce unit vectors

$$\hat{\boldsymbol{r}}\left(t\right)=\frac{\boldsymbol{r}\left(t\right)}{\left|\boldsymbol{r}\left(t\right)\right|},\qquad\hat{\boldsymbol{n}}=\frac{\boldsymbol{V}}{\left|\boldsymbol{V}\right|}. \tag{5.6}$$

Here, we focus on self-motile swimmers [58, 57, 38, 63, 41] that are analytically tractable and easily tuned so that their flow fields can vary from extensile to contractile, and which can be easily implemented numerically, allowing us to compare analytic estimates based on a time-averaged description with numerical results. As such, our two candidates are the two-sphere phased dipolar swimmer described in Chapter 4 and the elegant three-sphere swimmer derived by Najafi and Golestanian [35] in a sinusoidal-period form.

5.3 Tracer motion from a dipolar two-sphere swimmer

As the first example of tracer scattering by a self-motile object, we consider the two-sphere dipolar swimmer from Chapter 4. The stroke-averaged velocity field generated by the swimmer is dipolar, as given by (4.12), which we recast here as

$$\boldsymbol{v}\left(\boldsymbol{x}\left(t\right)|\boldsymbol{X}\left(t\right),\boldsymbol{V}\right)=V\kappa_{2}\left(\frac{a}{\left|\boldsymbol{r}\left(t\right)\right|}\right)^{2}\left[3\left(\hat{\boldsymbol{n}}\hat{\boldsymbol{r}}\right)^{2}-1\right]\hat{\boldsymbol{r}}, \tag{5.7}$$

with unit vectors $\hat{\boldsymbol{n}}$ and $\hat{\boldsymbol{r}}$ as defined in (5.6), and

$$\kappa_{2}=\frac{3}{4}\left(\frac{\ell}{a}\right)\left(1-\frac{3a}{2\ell}\right)^{-1}\frac{\tan\left(\Delta\theta\right)}{\tan\left(\Delta\phi\right)}. \tag{5.8}$$

Figure 5.2: Dipolar structure of the stroke-averaged flow field for two different setups: (a) extensile pusher with $\kappa_2 > 0$ and (b) contractile puller with $\kappa_2 < 0$. In both cases the swimmer is located at the origin, points along the $x-$axis, and swims in the positive $x-$direction. Swimmer parameters: $\ell = 20\mu$m, $\xi = a = 0.1\ell$, $\lambda = 0.1a$, $\omega = 500\text{s}^{-1}$ with $\Delta\phi = \Delta\theta = \pi/4$ for extensile swimmers and $\Delta\phi = 3\pi/4$, $\Delta\theta = \pi/4$ in the contractile case, yielding $V \simeq 14.7\mu$m/s and $\kappa_2 = \pm 8.8$. The flow fields are rotationally invariant about the $x-$axis. Arrows indicate the local direction $\hat{\boldsymbol{v}} := \boldsymbol{v}/|\boldsymbol{v}|$ of the stroke-averaged flow (5.7). Dark (bright) areas show the projection $(\hat{\boldsymbol{r}}\hat{\boldsymbol{v}})$, corresponding to regions where the mean flow points toward (away from) the swimmer. Results shown were obtained from direct simulation of time-resolved swimmer dynamics by tracking a grid of non-interacting tracer particles over a stroke period and agree very highly with stroke-averaged flow fields calculated from (5.7).

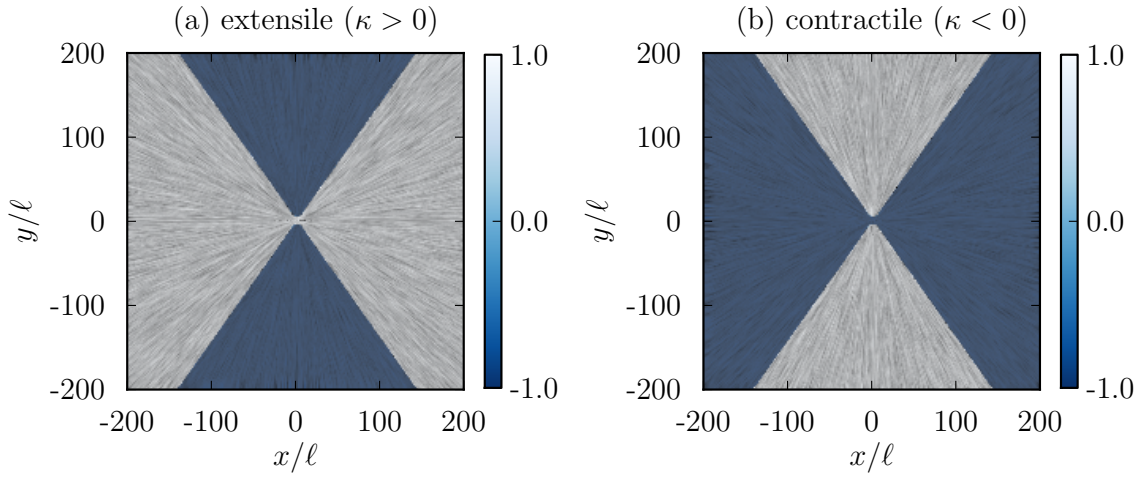

Note that, depending on the choice of $\Delta\phi$ and $\Delta\theta$, the coefficient κ_2 can be both negative or positive for a swimmer with $V > 0$. Swimmers with $\kappa_2 > 0$ are extensile 'pushers', whereas negative values $\kappa_2 < 0$ correspond to contractile 'pullers'. For our simulations, we used $\theta = 0, \Delta\phi = \Delta\theta = \pi/4$ to realize an extensile swimmer and $\theta = 0, \Delta\phi = 3\pi/4, \Delta\theta = \pi/4$ in the contractile case.

Again, linking two spheres with a harmonic spring of periodically varying equilibrium length $L(t)$ gives us (with a large enough stiffness parameter k_0) a model which essentially behaves like a shape-driven swimmer. As we are attempting to compare the exact tracer motion in the time-resolved flow field with the coarse-grained tracer dynamics in the time-averaged flow (5.7), we compare the two: Fig. 5.2 depicts the normalized velocity field $\hat{\boldsymbol{v}} := \boldsymbol{v}/|\boldsymbol{v}|$ obtained from microscopic simulation for $\kappa_2 > 0$

and $\kappa_2 < 0$, reconstructing the net (Lagrangian) flow fields by tracking a grid of non-interacting tracer particles over a stroke period. The color shading indicates the projection $(\hat{\boldsymbol{r}}\hat{\boldsymbol{v}})$, i.e., dark (bright) areas correspond to regions where the mean flow is directed toward (away from) the swimmer. For comparison, we calculated the same quantity using the stroke-averaged velocity field (5.7), finding good agreement with the results from the time-resolved simulations.

Based then on (5.7), it is possible to analytically estimate the mean tracer trajectory in the far-field limit by considering initial conditions with $\hat{\boldsymbol{n}} = (1, 0, 0)$ as depicted in Fig. 5.1, and approximating

$$\boldsymbol{r}\left(t\right) \simeq \boldsymbol{X}\left(t\right), \qquad \hat{\boldsymbol{n}}\hat{\boldsymbol{r}} \simeq \frac{X\left(t\right)}{\sqrt{X\left(t\right)^2 + Y_0^2}}, \tag{5.9}$$

with $X\left(t\right)$ denoting the swimmer's x-coordinate. The approximations (5.9) hold in the far-field scattering limit where (5.7) is valid. We are then able to integrate the equations of motion (5.2) in the deterministic limit (setting $D_0 = 0$), yielding the trajectory $\boldsymbol{x}\left(t\right) = \left(x\left(t\right), y\left(t\right), 0\right)$ of the tracer particle in the $(z = 0)$-plane,

$$x\left(t\right) \simeq -\kappa_2 a \left\{ \frac{a\left(2X_0^2 + Y_0^2\right)}{\left(X_0^2 + Y_0^2\right)^{3/2}} - \frac{a\left(2X\left(t\right)^2 + Y_0^2\right)}{\left(X(t)^2 + Y_0^2\right)^{3/2}} \right\}, \tag{5.10a}$$

$$y\left(t\right) \simeq -\kappa_2 a \left\{ \frac{aX_0Y_0}{\left(X_0^2 + Y_0^2\right)^{3/2}} - \frac{aX\left(t\right)Y_0}{\left(X\left(t\right)^2 + Y_0^2\right)^{3/2}} \right\}. \tag{5.10b}$$

Letting $t \to \infty$, we can see that asymptotically

$$x\left(t\right) \to -\kappa_2 a \left[\frac{a\left(2X_0^2 + Y_0^2\right)}{\left(X_0^2 + Y_0^2\right)^{3/2}} \right], \tag{5.11a}$$

$$y\left(t\right) \to -\kappa_2 a \left[\frac{aX_0Y_0}{\left(X_0^2 + Y_0^2\right)^{3/2}} \right], \tag{5.11b}$$

which offers an interesting conclusion: if the swimmer starts very far away in the

limit $X_0 \to -\infty$, the tracer returns to its initial condition $\boldsymbol{x}(0) = \mathbf{0}$, thus forming a closed loop in the $(z = 0)$-plane.

Fig. 5.3 shows tracer trajectories in the (x, y)-plane, based on the time-averaged flow field (5.7). Symbols were obtained by numerically integrating (5.2) for $D_0 = 0$ using the dipolar velocity field (5.10) using the same swimmer parameters as in Fig. 5.2. For comparison, we also plot, in Fig. 5.3 (b), the result from simulations that resolve the microscopic dynamics of the swimmer. In the latter case, one finds that the tracer particle performs a small oscillatory motion around its mean trajectory. The dotted lines indicate the analytic estimates from (5.10); comparing the two cases shows that the stroke-averaged description is able to capture the main features of the mean particle trajectory, in this case a "bowtie" pattern where each corner coincides with the tracer passing a shear line (extensile to contractile or the reverse) in the swimmer's flow field. The inset on Fig. 5.3 (b) shows that in-stroke oscillations in this pattern are mostly along the path of the tracer, commensurate with the sharp lines delineating what appear to be almost strictly radial (toward or away from the swimmer) portions of the dipolar flow field depicted in Fig. 5.2.

By setting $D_0 > 0$, the effects of Brownian motion on the tracer's path can be studied. As Eqn. (5.7) shows, the effective velocity field of the dipolar swimmer falls off as r^{-2}, thus increasing the relevance of thermal Brownian motion on the tracer particle versus advection by the swimmer's velocity field. This raises the question of whether the loop-like motion of the tracer remains in the presence of Brownian effects and might be observed under experimental conditions such as those considered by Leptos et al. [107] who tracked motions of *Chlamydomonas reinhardtii* algae in water at room temperature. To examine this, we numerically integrated the stochastic equations of motion (5.2) using a diffusion constant $D_0 = 0.22\mu\text{m}^2/\text{s}$, corresponding to a tracer particle of radius $a = 1\mu\text{m}$ and water at room temperature. We also performed microscopic time-resolved simulations of the same setup by applying

Figure 5.3: Deterministic tracer scattering by a dipolar two-sphere swimmer. In the limit $D_0 = 0$ the tracer trajectories converge to closed loops if the force-free 2-sphere swimmer starts sufficiently far away from the tracer (arrows indicate how the loop is traversed). The plots are based on initial conditions $X_0 = -350a$, $Y_0 = 10a$ for the swimmer and $\boldsymbol{x}(0) = \mathbf{0}$ for the tracer. The tracer trajectories are depicted for the time interval $[0, 100\text{s}]$. The swimmer parameters are the same as those in Fig. 5.2. Tracer radius: $a = 1\mu\text{m}$. Simulation time step: $\Delta t = 2.2 \times 10^{-7}\text{s}$. (a) Results for the stroke-averaged dynamics. Dotted lines indicate the analytic estimate from (5.10). Symbols were obtained by numerically integrating (5.2) for $D_0 = 0$ for the dipolar flow field (5.7) using the same parameters as in Fig. 5.2. (b) Results for the time-resolved dynamics. The inset shows the details of the oscillatory motion of the tracer particle near the turning point at the top-right corner of the extensile (blue) path.

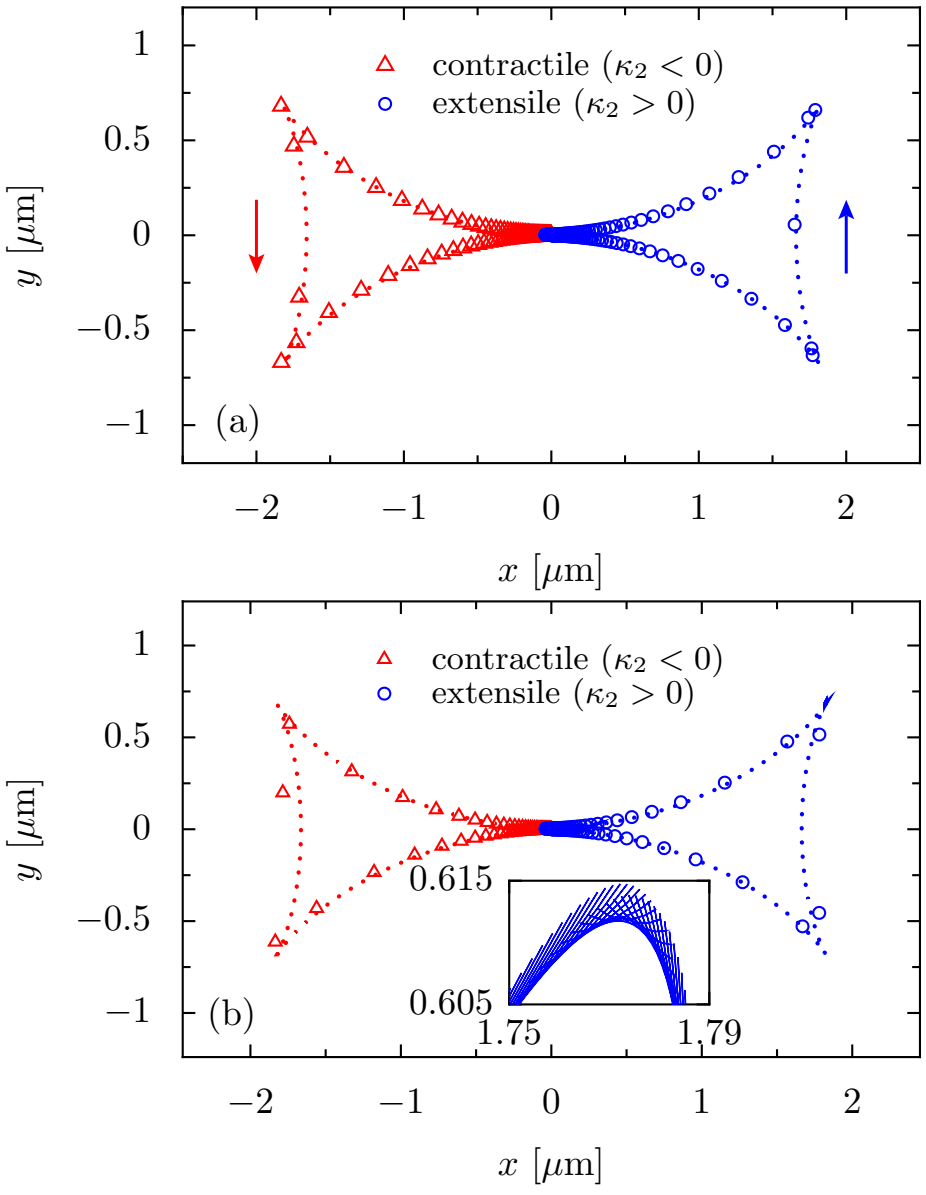

Figure 5.4: Brownian tracer scattering by a dipolar two-sphere swimmer. For $D_0 > 0$ loop-like scattering patterns can be recovered by averaging over many sample trajectories with identical initial conditions $\boldsymbol{x}(0) = \mathbf{0}$. (a) Results for the stroke-averaged dynamics obtained by numerically integrating (5.2) with $D_0 = 0.22\mu\text{m}^2/\text{s}$. (b) Results from the corresponding time-resolved simulations. The filled symbols in both figures were obtained by averaging over 1000 sample trajectories and dotted lines represent the analytic estimate from (5.10). Statistical error bars correspond to the sample standard deviation, divided by $10 \times \sqrt{t}$ for better visibility. Prior to rescaling, the length of the error bars agrees with the theoretically expected value $\sqrt{2D_0 t}$. Compared with Fig. 5.3, swimmer parameters are identical but the swimmer was started nearer to the tracer at $X_0 = -10a$, and sample trajectories were recorded for the shorter interval $t \in [0, 10\text{s}]$, thus producing loops that are not fully closed, in agreement with Eqn. (5.10) when t and X_0 are not taken to infinity.

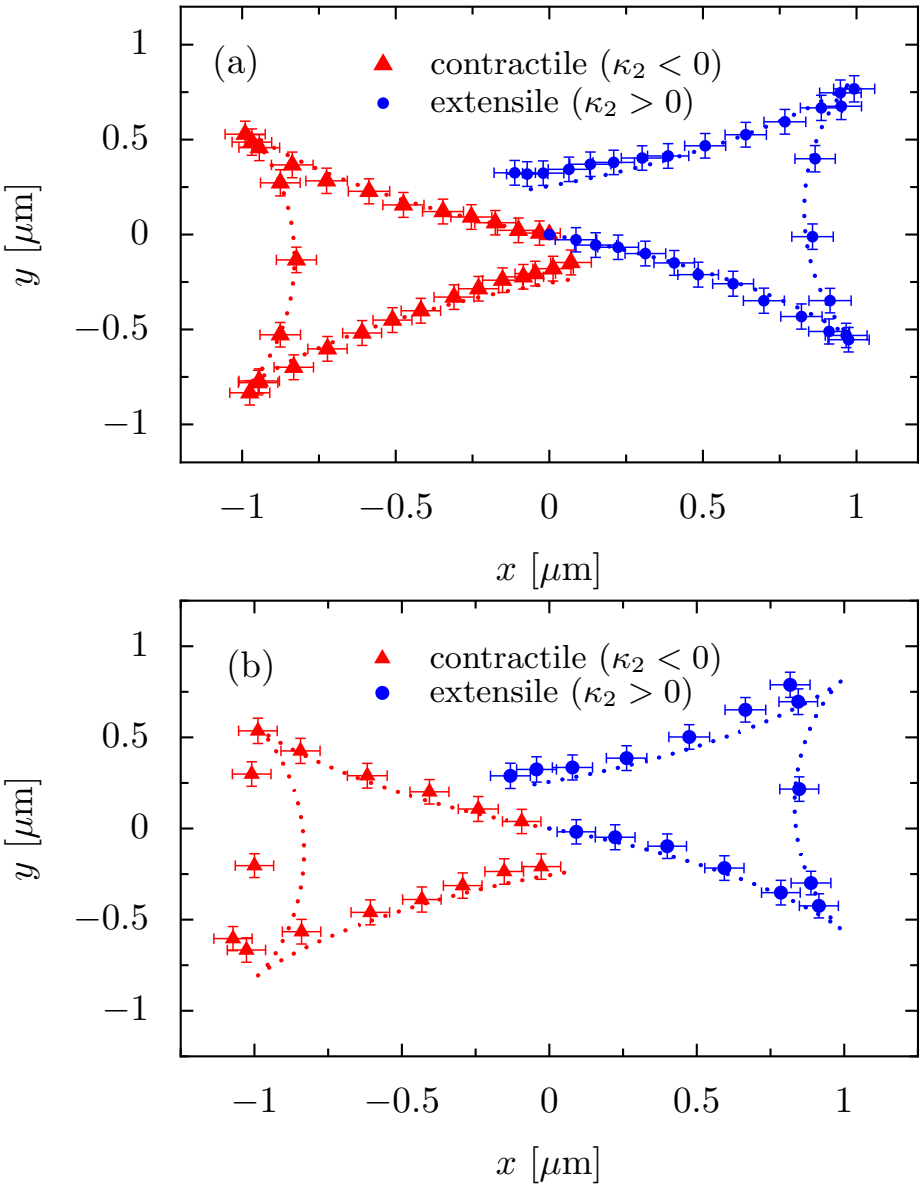

purely additive Gaussian noise to the tracer particles (no Cholesky decomposition was performed), leaving the swimmer noise-free to ensure that it traveled linearly.

The results are shown in Fig. 5.4 (a), where the mean tracer trajectories were obtained by numerical integration of the time-averaged model for extensile (red triangles) and contractile (blue circles) swimmers. Fig. 5.4 (b) shows the corresponding results for the time-resolved microscopic swimmer simulations. The numerical data points (filled symbols) in Fig. 5.4 were obtained by averaging over 1000 sample trajectories with identical initial conditions. In both cases, we used the same swimmer parameters as in Fig. 5.3, but the swimmer was started closer to the tracer at $X_0 = -10a$ to reduce computation time (this shorter run explains why the loops in Fig. 5.4 are open and not closed). The simulation time per run was limited to 10s. For comparison, isolated *Chlamydomonas* algae typically swim in an almost straight line for approximately $5 - 10s$ [110] before changing direction due to tumbling and rotational Brownian motion. The statistical bars in Fig. 5.4 correspond to the sample standard deviation and were divided by $10 \times \sqrt{t}$ for better visibility. Prior to this rescaling, the length of the error bars agrees well with the theoretically expected value $\sqrt{2D_0 t}$.

To summarize, the diagrams in Fig. 5.4 suggest that, despite the fact that individual trajectories may look very different due to the effects of Brownian motion, at sufficiently large sample size the loop-like patterns of Fig. 5.3 can be recovered.

5.4 Tracer motion from a (quasi-)quadrupolar three-sphere swimmer

As a second example, we consider the scattering of a tracer by the linear three-sphere swimmer suggested by Najafi and Golestanian [35] and examined by Alexander et al. [38]. This swimmer, by virtue of its geometry, generates a flow field which is a

superposition of quadrupolar (which dominates at close range) and dipolar flows. The lengths of the rear leg (R) and front leg (F) vary in time as

$$L_{F,R}(t) = \ell + \xi_{F,R} \sin(\omega t + \phi_{F,R}), \qquad \ell \gg a > 0, \tag{5.12}$$

where ℓ is the mean leg length and $\xi_{R,F}$ denotes the oscillation amplitude. If the initial phases $\phi_{R,F}$ are chosen such that

$$\Delta\phi := \phi_R - \phi_F > 0, \tag{5.13}$$

then the swimmer moves with stroke-averaged speed

$$V = \frac{7}{24} a\omega \sin(\Delta\phi) \frac{\xi_F \xi_R}{\ell^2} \tag{5.14}$$

in the direction of the front leg. The time-averaged flow field at distances far from the three-sphere swimmer is given by [38]

$$\begin{aligned} \boldsymbol{v}(\boldsymbol{x}(t) | \boldsymbol{X}(t), \boldsymbol{V}) = & V\kappa_2 \left(\frac{a}{|\boldsymbol{r}(t)|}\right)^2 \left[3\left(\hat{\boldsymbol{n}}\hat{\boldsymbol{r}}^2 - 1\right)\hat{\boldsymbol{r}}\right] + \\ & V\kappa_3 \left(\frac{a}{|\boldsymbol{r}(t)|}\right)^3 \left\{\left[15(\hat{\boldsymbol{n}}\hat{\boldsymbol{r}})^3 - 9(\hat{\boldsymbol{n}}\hat{\boldsymbol{r}})\right]\hat{\boldsymbol{r}} - \left[3(\hat{\boldsymbol{n}}\hat{\boldsymbol{r}})^2 - 1\right]\hat{\boldsymbol{n}}\right\} \end{aligned} \tag{5.15}$$

with unit vectors $\hat{\boldsymbol{n}}$ and $\hat{\boldsymbol{r}}$ as defined in (5.6). The constants $\kappa_{2,3}$ represent the strengths of the field contributions and are determined by the swimmer's geometry,

$$\kappa_2 = \frac{9}{32} \frac{\xi_R^2 - \xi_F^2}{a\ell}, \qquad \kappa_3 = \frac{51}{56} \left(\frac{\ell}{a}\right)^2.$$

The quadrupole coefficient is always positive ($\kappa_3 > 0$), but we can have either $\kappa_2 > 0$ (extensile 'pusher'), $\kappa_2 = 0$ (symmetric quadrupolar swimmer) or $\kappa_2 < 0$ (contractile

Figure 5.5: Quasi-quadrupolar fluid flow generated by three-sphere swimmers, showing the structure of the stroke-averaged flow field of a three-sphere swimmer for three different parameter sets: (a) extensile pusher with $0.2\ell = \xi_R > \xi_F = 0.1\ell$, (b) symmetric swimmer with $\xi_R = \xi_F = \sqrt{0.02}\ell$, and (c) contractile puller with $0.1\ell = \xi_R < \xi_F = 0.2\ell$. In all three cases, the swimmer is located at the origin, points along the $x-$axis, and swims in the positive $x-$direction. The flow fields are rotationally invariant about the $x-$axis. Arrows indicate the local direction $\hat{\boldsymbol{v}} := \boldsymbol{v}/|\boldsymbol{v}|$ of the stroke-averaged flow field. Dark (bright) areas show the projection $(\hat{\boldsymbol{r}}\hat{\boldsymbol{v}})$, corresponding to regions where the mean flow points towards (away from) the swimmer. Note that in all three cases the quadrupolar contribution dominates at intermediate distances. Swimmer parameters: $\ell = 10\mu$m, $a = 0.2\ell$, $\omega = 10^3 \mathrm{s}^{-1}$, $\Delta\phi = \pi/2$, corresponding to $V \simeq 12\mu$m/s. Flow fields were obtained by tracking a grid of tracer particles over a stroke period as in Fig. 5.2 and agree highly with corresponding stroke-averaged flow fields calculated using (5.15).

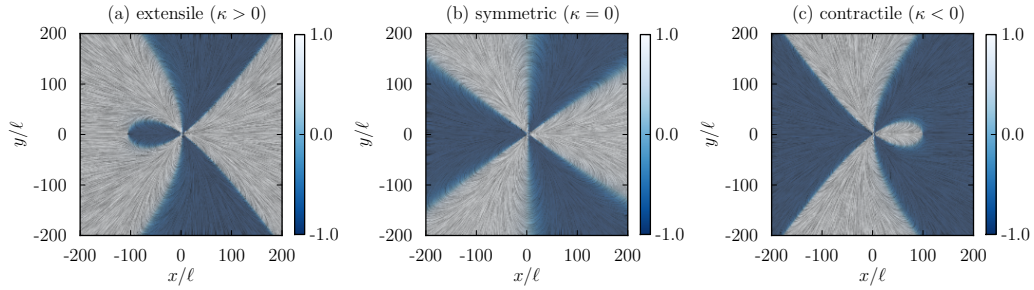

'puller'), depending on the choice of oscillation amplitudes $\xi_{R,F}$. Importantly, the geometric restriction $\ell > 2a + \xi_R + \xi_F$ implies that $\kappa_2 \ll \kappa_3$, and thus the quadrupolar κ_3 term dominates the flow field (5.15) except at fairly large distances. As seen in Fig. 5.5 (a,c), with even moderate asymmetry the quadrupolar flow dominates for distances up to a hundred body lengths. In Fig. 5.5 we show the normalized flow field $\hat{\boldsymbol{v}} := \boldsymbol{v}/|\boldsymbol{v}|$ from microscopic simulation (5.15) and its projection onto the unit vector $\hat{\boldsymbol{r}}(t)$ for $\kappa_2 > 0$, $\kappa_2 = 0$, and $\kappa_2 < 0$. The flow agrees very highly with that calculated using the analytical formula (5.15).

Based on (5.15), we again derive an analytic estimate for the mean tracer trajectory. Considering initial conditions with $\hat{\boldsymbol{n}} = (1, 0, 0)$ as depicted in Fig. 5.1 and making use of the earlier approximations (5.9), we integrate the equations of motion (5.2) for $D_0 = 0$, finding the trajectory of the tracer particle in the $(z = 0)$-plane as

$\boldsymbol{x}(t) = (x(t), y(t), 0)$, where

$$x(t) \simeq -\kappa_2 a \left\{ \frac{a\left(2X_0^2 + Y_0^2\right)}{\left(X_0^2 + Y_0^2\right)^{3/2}} - \frac{a\left(2X(t)^2 + Y_0^2\right)}{\left(X(t)^2 + Y_0^2\right)^{3/2}} \right\} + \kappa_3 a \left\{ \frac{a^2 X_0 \left(2X_0^2 - Y_0^2\right)}{\left(X_0^2 + Y_0^2\right)^{5/2}} - \frac{a^2 X(t)\left(2X(t)^2 - Y_0^2\right)}{\left(X(t)^2 + Y_0^2\right)^{5/2}} \right\}, \tag{5.16a}$$

$$y(t) \simeq -\kappa_2 a \left\{ \frac{aX_0 Y_0}{\left(X_0^2 + Y_0^2\right)^{3/2}} - \frac{aX(t) Y_0}{\left(X(t)^2 + Y_0^2\right)^{3/2}} \right\} + \kappa_3 a \left\{ \frac{a^2 X_0 \left(2X_0^2 - Y_0^2\right)}{\left(X_0^2 + Y_0^2\right)^{5/2}} - \frac{a^2\left(2X(t)^2 - Y_0^2\right) Y_0}{\left(X(t)^2 + Y_0^2\right)^{5/2}} \right\}. \tag{5.16b}$$

Note that the dipolar (κ_2) contributions are formally equivalent to the result for the two-sphere swimmer (5.10), but with V and κ_2 now determined by the geometry of the three-sphere swimmer. In the asymptotic limit where $t \to \infty$, we find that

$$x(t) \to -\kappa_2 a \left(\frac{a\left(2X_0^2 + Y_0^2\right)}{\left(X_0^2 + Y_0^2\right)^{3/2}} \right) + \kappa_3 a \left(\frac{a^2 X_0 \left(2X_0^2 - Y_0^2\right)}{\left(X_0^2 + Y_0^2\right)^{5/2}} \right), \tag{5.17a}$$

$$y(t) \to -\kappa_2 a \left(\frac{aX_0 Y_0}{\left(X_0^2 + Y_0^2\right)^{3/2}} \right) + \kappa_3 a \left(\frac{a^2\left(2X_0^2 - Y_0^2\right) Y_0}{\left(X_0^2 + Y_0^2\right)^{5/2}} \right). \tag{5.17b}$$

Again, Eqns. (5.17) predict that if the swimmer starts very far away (corresponding to the limit $X_0 \to -\infty$), the tracer will return to its initial position $\boldsymbol{x}(0) = \mathbf{0}$, thus forming a closed loop in the $(z = 0)$-plane. However, comparing the dipolar tracer "bowtie" pattern from Fig. 5.3 (a) with the "cloverleaf" pattern produced by the three-sphere swimmer in Fig. 5.6 we see very different paths, as the flow field (5.15) is dominated by the quadrupolar κ_3 contribution for the swimmer geometry and initial conditions used.

The time-resolved microscopic simulations agree closely with the analytics, although the in-stroke oscillations, shown in Fig. 5.6 (b), are qualitatively different from the dipolar case (Fig. 5.2 (b)). The superpositions of dipolar and quadrupolar flow cause more oscillation perpendicular to the mean tracer path, resulting in

more obvious oscillations away from the mean tracer path. The relative magnitude of the tracer's in-stroke oscillations from its mean path is larger than in the case of the dipolar two-sphere swimmer, as the effective quadrupolar flow field of the three-sphere swimmer decays more rapidly, resulting in a smaller absolute loop size at similar initial conditions and swimmer speeds. As is evident from Fig. 5.6, the stroke-averaged result captures the main features of the mean tracer motion in the time-resolved flow field, but there is a quantitative difference of approximately 20 to 30 percent due to the approximations made during the stroke-averaging process. However, we can still observe that asymptotically the time-resolved tracer trajectory approximately returns to its initial position if the swimmer starts sufficiently far away from the tracer particle.

When Brownian motion is taken into account, corresponding to $D_0 > 0$ in (5.2), individual tracer trajectories may differ strongly from each other, as the weaker quadrupolar velocity field creates trajectories more easily washed out by Brownian motion. However, as for the two-sphere dipolar swimmer, loop-shaped scattering patterns can be reconstructed by averaging over a tracer ensemble with identical conditions. Fig. 5.7 shows mean tracer trajectories obtained by averaging over 1000 sample trajectories. We used the same swimmer parameters as in Fig. 5.6, but started the swimmer closer to the tracer at $X_0 = -10a$ and reduced simulation time per run to 11s, as this is roughly similar to the time scale during which an isolated alga performs a quasilinear motion [108]. The statistical error bars in Figs Fig. 5.7 illustrate the sample standard deviation and were divided by $10 \times \sqrt{t}$ for better visibility; prior to this rescaling the length of the error bars agreed well with the value $\sqrt{2D_0t}$ expected theoretically. In both Fig. 5.7 (a) and (b), we notice a small systematic drift of the mean Brownian trajectories compared to the corresponding deterministic trajectories (unfilled symbols) and analytic estimate (dotted lines), which occurs in the direction of the swimmer motion and is possibly caused by a noise-induced Stokes drift [111]

Figure 5.6: Deterministic tracer scattering by a (quasi-)quadrupolar three-sphere swimmer. In the deterministic limit $D_0 = 0$, the tracer trajectories converge to closed loops if the force-free three-sphere swimmer starts sufficiently far away from the tracer, $X_0 \to -\infty$. The dotted lines in either diagram represent the analytical estimate from (5.16). (a) Results from the stroke-averaged dynamics for the time interval $[0, 55\text{s}]$. The tracer particle starts at $\boldsymbol{x}(0) = \mathbf{0}$ and the swimmer at $X_0 = -150a$, $Y_0 = 10a$. Symbols were obtained by numerically integrating (5.2) for $D_0 = 0$ using the stroke-averaged flow field (5.15). (b) Results from the corresponding time-resolved simulation for the same time interval and initial conditions for the geometric centre of the swimmer. The tracer oscillates due to the periodicity of the swimming stroke. Swimmer parameters: $\ell = 10\mu\text{m}$, $a = 0.2\ell$, $\omega = 10^3\text{s}^{-1}$, $\Delta\phi = \pi/2$, which results in $V \simeq 12\mu\text{m/s}$, $\kappa_2 \simeq \pm 0.04$, $\kappa_3 \simeq 22$. Tracer radius $a = 1\mu\text{m}$, simulation time step $\Delta t = 2.2 \times 10^{-7}\text{s}$.

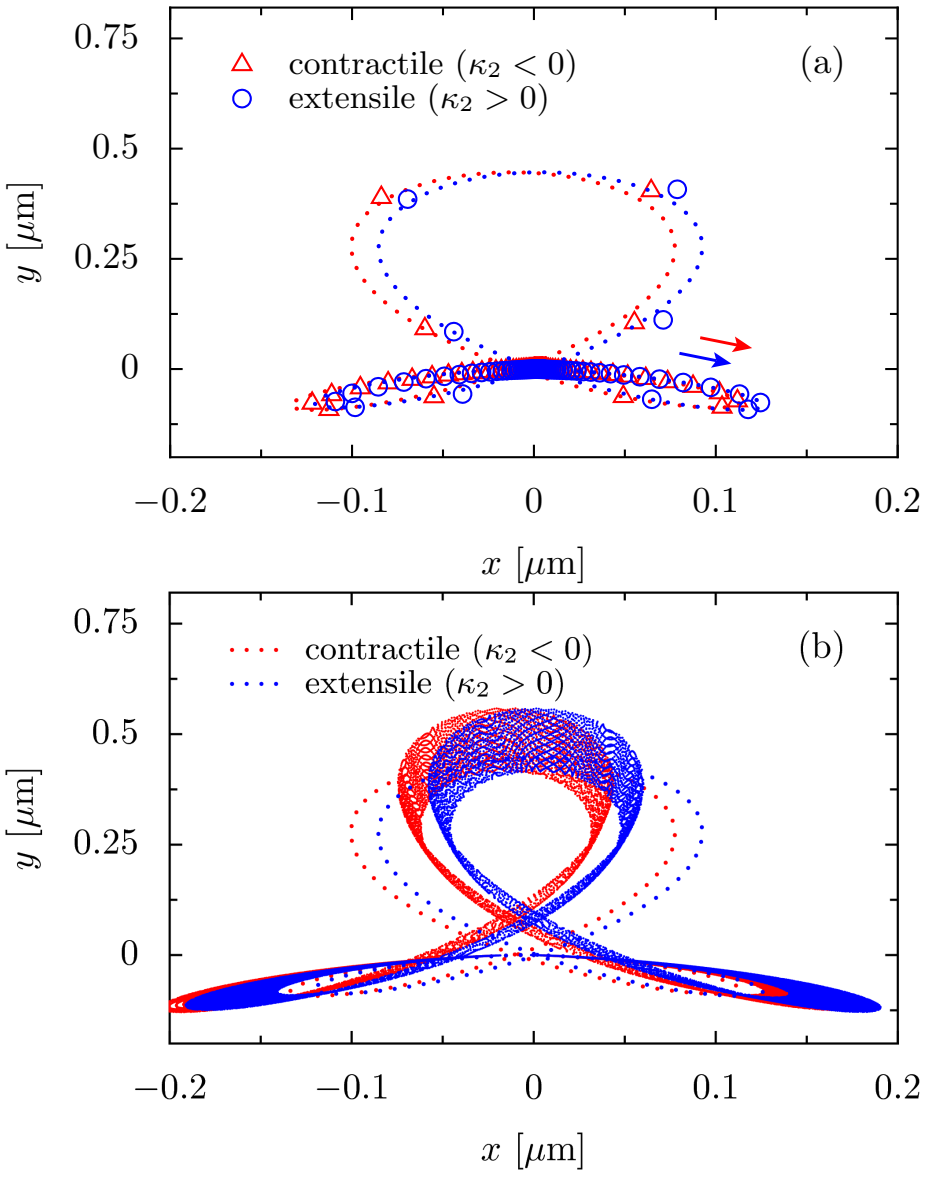

and an additional noise-induced bias due to the gradients of the flow field.

5.5 Discussion

We have examined the hydrodynamic scattering of a neutral tracer particle for different types of model swimmers: the abstract phased dipolar swimmer from Chapter 4 and the Najafi-Golestanian three-sphere swimmer [35]. Using both symbolic analysis and numeric simulation, we showed that scattering by a force-free swimmer may lead to quasi-closed loop-shaped tracer trajectories. The shapes and orientations of the loops are determined by the properties of the stroke-averaged flow field. Our results imply that a time-averaged description is sufficient for capturing the main features of swimmer-tracer scattering.

The presence of Brownian motion may obscure individual tracer trajectories, but our analysis shows that averaging over many trajectories may allow one to reconstruct the loops from noisy data, suggesting that such patterns could be studied in experiments similar to those of Leptos et al. [107]; in fact, the inset of Fig. 1 (c) from [107] and shown here as Fig. 5.8 shows a particle in a suspension of *Chlamydomonas reinhardtii* algae which, despite the many swimmers and Brownian motion, still shows a looplike path. However, a systematic experimental investigation remains an interesting challenge for the future, possibly by adapting the experimental setup of Leoni et al. [52], who constructed a colloidal linear three-sphere pump using optical tweezers.

Figure 5.7: Brownian tracer scattering by a (quasi-)quadrupolar three-sphere swimmer. For $D_0 > 0$, loop-like scattering patterns can be recovered by averaging over many sample trajectories with identical initial conditions $\boldsymbol{x}(0) = \mathbf{0}$. (a) Results for the stroke-averaged dynamics obtained by numerically integrating (5.2) with $D_0 = 0.22\mu\text{m}^2/\text{s}$. (b) Results from corresponding time-resolved simulations. The filled symbols in both figures were obtained by averaging over 1000 sample trajectories; unfilled symbols show the results of simulations with $D_0 = 0$, and dotted lines represent the analytic estimate from (5.16). Statistical error bars correspond to sample standard deviation, divided by $10 \times \sqrt{t}$ for better visibility. Prior to rescaling, error bar length agreed with the theoretically expected value $\sqrt{2D_0 t}$. Compared to Fig. 5.6, we used the same swimmer parameters but the swimmer was started nearer to the tracer at $X_0 = -10a$ and sample trajectories were recorded for the shorter interval $t \in [0, 11\text{s}]$, resulting in loops which are not fully closed.

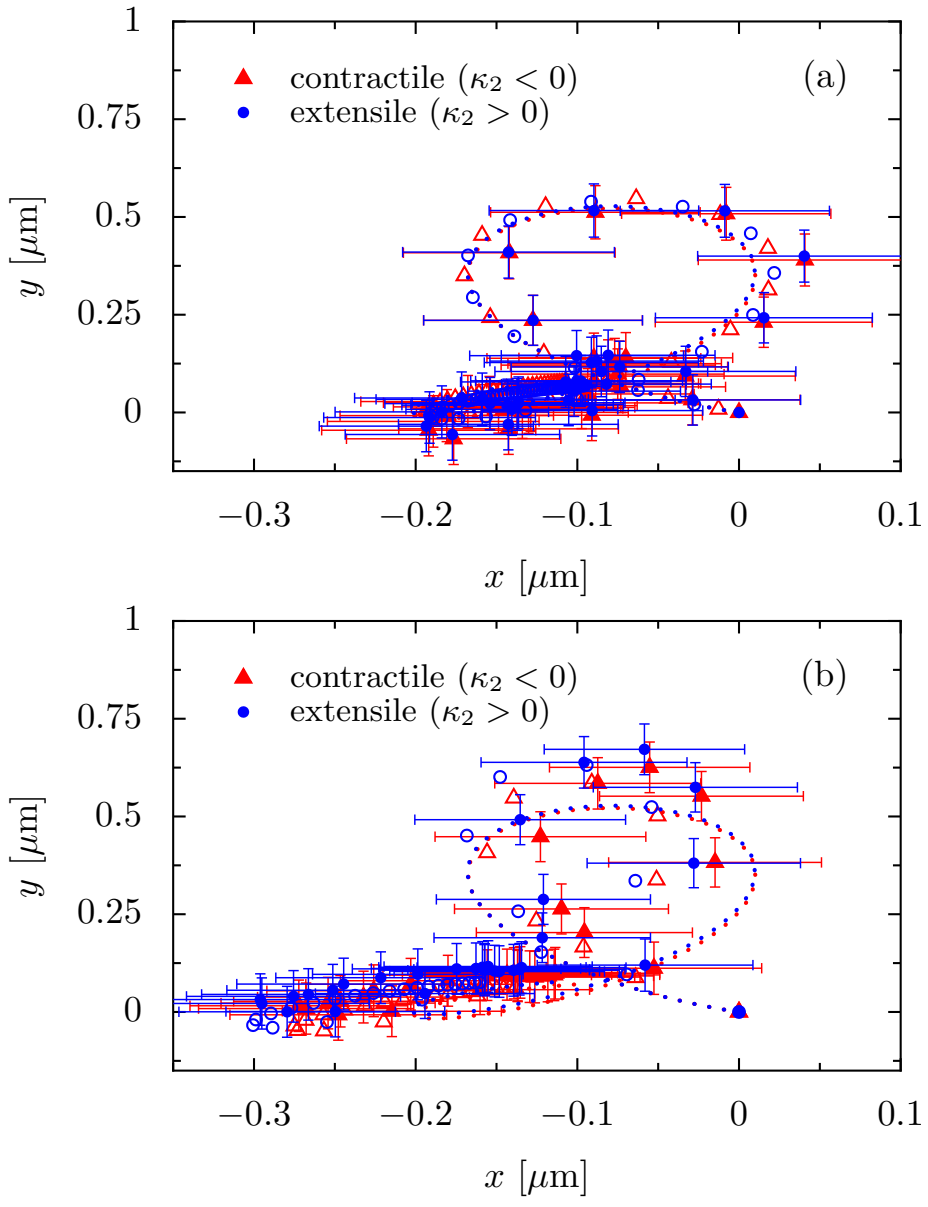

Figure 5.8: Fig 1 (c) from [107], with kind permission of Prof. Raymond E. Goldstein; inset shows the looplike path of a tracer particle in a suspension of *Chlamydomonas reinhardtii* algae.

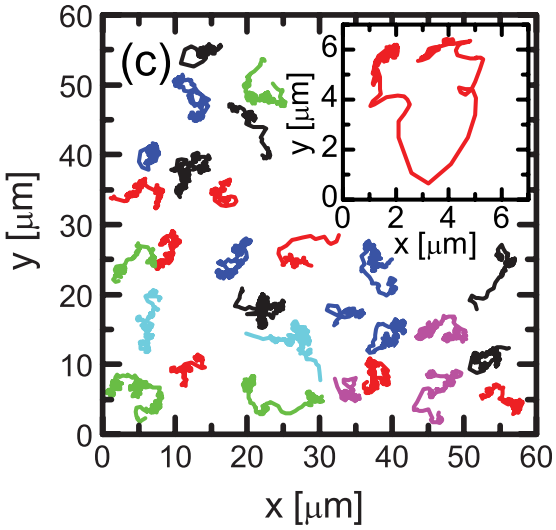

Chapter 6

Synchronisation of model microswimmers

6.1 Introduction

We now turn away from the effects of passive swimmer interactions (those generated by net flow with no reliance on interswimmer phase differences, as in Eqns. (4.18) and (4.19)) and examine again active interactions (those dependent on interswimmer phase differences, as in Eqns. (3.8)-(3.13)). Given the importance of relative phase in controlling some swimmer-swimmer interactions (as seen in Chapters 2 and 3, and for swimmers generating weak velocity fields [40]), it is feasible that biological swimmers could exploit phase changes to control their relative motion. Indeed, there is considerable evidence that hydrodynamic phase synchronisation is feasible at low Reynolds number. One striking example of this is the coordinated motion of beating cilia (metachronal waves), thought to be a consequence of hydrodynamic interactions [112, 113, 114, 115]. Additionally, Taylor [48] demonstrated that two undulating sheets minimise their dissipation if they oscillate in phase, and simulations have demonstrated that sperm cells adjust their position to synchronise their

motion [91]. Reichert and Stark [116] showed synchronisation due to hydrodynamic interactions of rigid helices anchored in harmonic traps, and Uchida and Golestanian [117] saw evidence of synchronisation in an array of rotors on a substrate.

However, the discussion of microscopic swimmers to this point has assumed a strictly shape-driven swimmer, one which, though advected and rotated by external flow, still proceeds relentlessly through its movement cycle according to the dictates of an internal clock. While this formulation simplifies analysis, it does not allow the relative phase of two swimmers to change dynamically. As we have shown, in certain circumstances (particularly in cases where swimmers swim weakly or generate little net fluid flow), the relative phase between swimmers can have significant impacts on the way in which they interact.

To explore synchronisation in the context of linear-sphere swimmers, we must modify the simple models from shape-driven to force-driven, allowing hydrodynamics to alter the speed at which the swimmer proceeds through its cycle.

6.2 Modifying a model swimmer

We consider the established linear three-sphere swimmer conceptualized by Najafi and Golestanian [35]. We used the basic design as a quadrupolar swimmer in Section 5.4, but for this discussion we remove the sinusoidal motion of its legs and move them linearly in the cycle shown in Fig. 1.2 (a). In its original and most basic form, the three-sphere swimmer proceeds at constant velocity, and we shall term this a *constant velocity* swimmer [64, 41, 40]. But it is also possible to drive the extension or contraction of each leg by equal and opposite applied forces F_a acting on the spheres at the end of that rod (a *constant force* swimmer). However, to ensure that the swimmer remains in a valid configuration (i.e., it does not bend and the length of the passive leg remains fixed), a set of constraint forces must be calculated.

For both the constant velocity and constant force swimmers, we define each stage of the cycle to continue until the active rod has reached a specified *length*, rather than lasting for a specified *time* (a different condition from that used for the previous swimmers in this thesis). For a single swimmer, this is an irrelevant distinction, as the relative positions of the beads during the cycle, rather than the speed at which the stroke is completed, defines the swimmer motion. However, for more than one swimmer these two definitions are not equivalent, as hydrodynamic interactions between swimmers can affect how quickly a given swimmer progresses through its stroke. Thus, while interacting constant velocity swimmers have, by definition, a fixed cycle period, interacting constant force swimmers can reach a specified leg length at different times, allowing the possibility of phase synchronisation.

6.3 Equations of motion

As before, we rely on the model of a swimmer as an assemblage of spheres generating a velocity field as a linear combination of the forces $\boldsymbol{f}_m$ acting on each sphere m [33]. This can be evaluated at the location of sphere n to give its velocity

$$\dot{\boldsymbol{q}}_n = \sum_m \mathcal{H}_{nm} \boldsymbol{f}_m. \tag{6.1}$$

The tensor $\mathcal{H}_{mn}$ is known exactly only for point spheres; for this study, we used the Rotne-Prager-Yamakawa approximation [26, 27] for finite radius spheres in our simulations.

In general, (6.1) must be solved numerically, although as shown earlier certain specific configurations permit analytical treatment. Once the forces are calculated, the outputs are the velocities of the beads, which in turn define the swimming motion.

The applied forces moving the active leg are only part of the puzzle in this case, for in the absence of a purely shape-driven model we must calculate *constraint* forces as

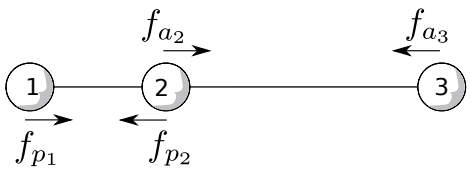

Figure 6.1: Forces on a three-sphere swimmer during contraction of the right-hand leg

well to maintain the swimmer's validity. Imposing a fixed length on the passive leg is equivalent to imposing constraint forces on the spheres at its ends; these constraints are internal to the swimmer, so they must be equal and opposite to maintain the force-free condition. In two or more dimensions, additional constraint forces must also be formulated to preserve the linearity of the swimmer against bending.

To obtain an expression for the constraint forces of N swimmers, we define the positions of the $3N$ spheres needed to construct them by the $9N$-component vector $\boldsymbol{q}$. We define the applied forces $\boldsymbol{f}_a \equiv (\boldsymbol{f}_{a1}, \boldsymbol{f}_{a2}, \ldots)$ as the $9N$-component vector listing the (known) forces moving the active legs of the swimmers, and vectors $\boldsymbol{f}_{p\alpha} \equiv \left(\boldsymbol{f}_{p1}, \boldsymbol{f}_{p2}, \ldots\right)$ describing the forces needed to impose each of the constraints which preserve the lengths of the passive legs. For example, for swimmer 1, when the leg between beads 1 and 2 remains at a constant length, $\boldsymbol{f}_{p\alpha} = \left(\boldsymbol{f}_{p1}, \boldsymbol{f}_{p2}, \mathbf{0}, \mathbf{0}, \mathbf{0}, \ldots\right)$ (see Fig. 6.1). Each holonomic constraint α is specified by a function $C_\alpha(\boldsymbol{q}) = 0$. $\dot{C}_\alpha = \sum_i \frac{\partial C_\alpha}{\partial q_i}\dot{q}_i = 0$, or, defining $j_{\alpha i} \equiv \frac{\partial C_\alpha}{\partial q_i}$,

$$\boldsymbol{j}_\alpha^T \cdot \dot{\boldsymbol{q}} = 0. \tag{6.2}$$

The constraint forces must be purely passive and do no actual work on the swimmer; thus,

$$\boldsymbol{f}_{p\alpha}^T \cdot \dot{\boldsymbol{q}} = 0. \tag{6.3}$$

Equations (6.2) and (6.3) imply that

$$\boldsymbol{f}_{p\alpha} = \lambda_\alpha \boldsymbol{j}_\alpha. \tag{6.4}$$

Substituting (6.4) into (6.1), and using (6.2) gives

$$-\boldsymbol{j}_\beta^T \mathcal{H} \boldsymbol{f}_a = \sum_\alpha \boldsymbol{j}_\beta^T \mathcal{H} \boldsymbol{j}_\alpha \lambda_\alpha, \tag{6.5}$$

a set of simultaneous equations that can be solved for the constraint multipliers λ_a. In this case, $\boldsymbol{j}_\beta^T \mathcal{H} \boldsymbol{j}_\alpha$ is symmetric, and hence

$$\lambda_\alpha = -\left(\boldsymbol{j}_\alpha^T \mathcal{H} \boldsymbol{j}_\beta\right)^{-1} \left(\boldsymbol{j}_\alpha^T \mathcal{H} \boldsymbol{f}_\beta\right). \tag{6.6}$$

The advantage of this method is that it is very general and can be used for any arbitrary holonomic constraint; it is possible to pin spheres in place, thus modeling a pump, keep two swimmers tethered at a fixed distance from each other, or construct elaborate low Reynolds number "robots" with different sorts of joints. Additionally, when the forces involved are known, the explicit calculation of constraint forces allows relatively large timesteps to be used, as the forces involved do not change dramatically during a stroke. This is in sharp contrast to the models used in earlier chapters, which required a very small timestep due to the time scales the stiff springs required (see discussion in Section 2.2). However, since the system interaction tensor $\mathcal{H}$ is in general dense, the required numerical inversion in (6.6) to find the λ_α makes this method $\mathcal{O}(N^3)$ in general and thus very slow for large populations. This can, however, be mitigated somewhat by using other numerical methods (such as finding λ_α through a conjugate gradient method applied to Eqn. (6.5), which solves for λ_α by an iterative refinement of guesses that converge to a solution within a specified tolerance; see [118]). In order to reduce any mathematical error, and to simplify the code, we preferred numerical inversion.

Additionally, while larger timesteps were usable in general, near the end of each leg movement it was necessary to stop the motion exactly at the prescribed leg length. Failure to do so resulted in swimmers which distorted over time, and caused erroneous

results. To counteract this, as any leg of any swimmer reached the end of its travel, the simulation had to calculate as precisely as possible a timestep which would move the leg exactly the correct amount. As the number of swimmers increased, the simulation began to spend proportionally much more of its CPU time determining these end-of-motion timesteps than it did during the main travel of the leg.

6.4 Phase locking of one-dimensional swimmers

To examine phase-locking, it is only necessary to impose intra-swimmer constraints which keep individual swimmers consistent within their shape. The motion of each swimmer is thus controlled by fixed applied forces $\boldsymbol{f}_a$ which act until the active arm reaches a prescribed length. When more than one swimmer is present, however, external advection produced by fluid flow from other swimmers' motions can impact how *quickly* the swimmer proceeds through its cycle, allowing for the possibility of phase-locking.

To discuss the notion of phase in a non-sinusoidal context and a variable-length cycle, it is most convenient to define a *spatial phase* which is a function only of the lengths of a swimmer's legs, independent of an explicit time variable. During a complete swimming stroke, the active spheres move a total distance $2\left(\xi_f + \xi_r\right)$ relative to the centre sphere. We define the spatial phase ϕ of a swimmer as the fraction of this distance traveled since the beginning of the stroke, multiplied by 2π, giving a number varying from 0 at the beginning of the stroke to 2π at the completion of the stroke.

As a first example, we consider the behaviour of two collinear swimmers moving in one dimension. Two extensile swimmers, with $\xi_f = 0.1$ and $\xi_r = 0.5$, were placed along the x-axis with their centres of mass separated by three leg lengths. The initial phase of the leading swimmer was taken to be $\phi = 0$, and several simulations were

Figure 6.2: Time evolution of the state of two collinear extensile swimmers with $\ell = 1, a = 0.03, \xi_r = 0.5, \xi_f = 0.1$ for different initial relative phase. (a) Variation of relative phase with time; the graph shows the phase of the rear swimmer, ϕ_2, measured at the beginning of the stroke of the leading swimmer ($\phi_1 = 0$). (b) Distance between the centres of mass of the swimmers.

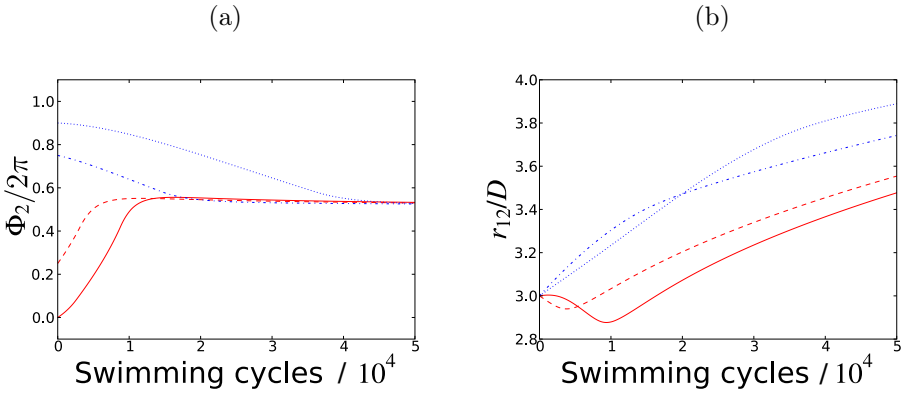

run for different initial phases of the trailing swimmer. Each simulation was run for 50,000 swimmer cycles.

Figure 6.2a compares the variation of the phase of the rear swimmer measured at the beginning of the lead swimmer's stroke as it evolves over time. It is apparent that the phase difference between the swimmers slowly drifts toward a stable value, indicating phase-locking behaviour. At the lock-in point, the swimmers are approximately out of phase with each other ($|\phi_2 - \phi_1| \approx \pi$).

As the relative phase changes, the transport of the swimmer is affected; the evolution of the distance between the two swimmers is plotted in Fig. 6.2b. As the trailing swimmer changes its phase, it moves closer to the lead swimmer for a time before settling, at the locking point, to motion away from the lead swimmer. This agrees with the conclusion in [40] that extensile, collinear, constant-period swimmers attract if they are in phase but repel if they are out of phase.

The phase locking occurs because velocity gradients across a swimmer due to hydrodynamic interactions between swimmers can either assist or hinder the leg motion. Figure 6.3 illustrates this by showing the change in phase experienced by the trailing

swimmer after one swimming cycle. If the trailing swimmer is iterating through its cycle more quickly than the lead swimmer, it will show a positive change in phase, corresponding to moving along the graph in Fig. 6.3 to the right. Similarly, if hydrodynamic interactions hinder the swimmer in its cycle, its phase will fall behind that of the lead swimmer, corresponding to moving to the left. Locking occurs when a stable point (zero phase shift) is reached. The further the curve from the x-axis, the faster the phase-locking behaviour proceeds. Details of the shape of the phase-change curve in Fig. 6.3 depend on the swimmer parameters and their separation. In general it becomes flatter and more centred about a phase change of zero as the distance between the swimmers increases, because the hydrodynamic interactions between them decrease.

By examining the points at which the curve crosses the x-axis for increasing swimmer-swimmer spacing, we can identify how the relative phase of the swimmers in the phase-locked state varies with their separation. This is shown in Fig. 6.4. For a collinear arrangement of two swimmers, the lock point depends only weakly on the distance between them, although the time it takes to adjust phases increases with separation. For the case of collinear swimmers moving in opposite directions (Fig. 6.3d), the symmetry of the arrangement forces the stable lock point to be exactly halfway through the cycle ($\phi_2 = \pi$).

The swimmer we have considered so far has leg amplitudes $\xi_f < \xi_r$. Such an extensile swimmer is related to a contractile swimmer, with ξ_f and ξ_r interchanged, through a T-dual transformation i.e. time reversal, together with a relabelling of front and rear [39]. In terms of Fig. 6.3, this corresponds to an inversion of the curve $y \to -y$ (compare Figs 6.3b and 6.3c). The stable zeros of an extensile swimmer thus become the unstable zeros of its T-dual, contractile counterpart, and contractile swimmers lock-in to a relative phase $\phi \sim 0$.

When $\xi_r = \xi_f$, the swimmer is neither extensile nor contractile and it maps onto

Figure 6.3: Change in the phase of the trailing swimmer after one swimming cycle as a function of its phase at the beginning of the cycle of swimmer 1. Crossing points on the x-axis represent either an unstable (for positive slope) or a stable (if the slope is negative) lock-in point. Arrows indicate how the swimmer's motion evolves with time. All swimmers have $\xi_r = 0.5$, $\xi_f = 0.1$, $\ell = 1$. (a) Separation=3ℓ; extensile, $\xi_r = 0.5$, $\xi_f = 0.1$; swimmers moving in same direction; (b) separation=5ℓ; extensile, $\xi_r = 0.5$, $\xi_f = 0.1$; swimmers moving in same direction; (c) separation=5ℓ; contractile; $\xi_r = 0.1$, $\xi_f = 0.5$; swimmers moving in same direction; (d) separation=5ℓ; $\xi_r = 0.5$, $\xi_f = 0.1$; swimmers moving away from each other.

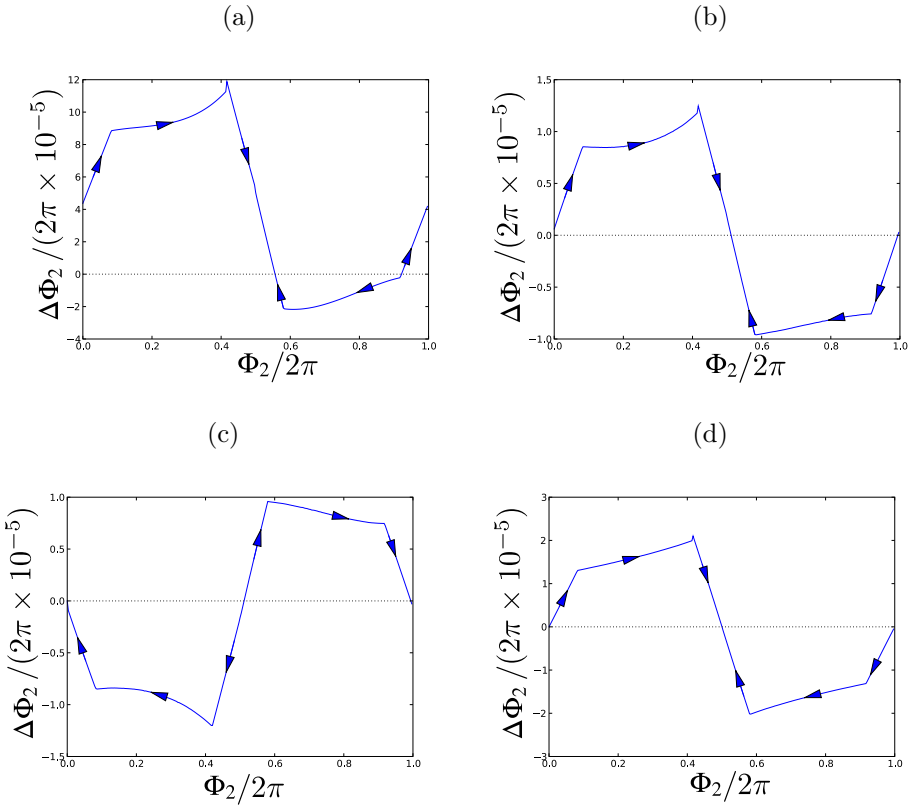

Figure 6.4: Stable and unstable lock-in points of the relative phase of two collinear swimmers as a function of their separation.

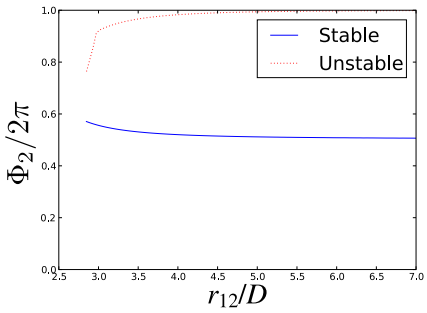

itself under the T-duality transformation (its flow field is not dipolar, but decays more rapidly, as r^{-3} [40]). The phase-change curve now lies along the x-axis, corresponding to a difference in cycle time of zero for all relative phases. Hence there is no phase-locking, as expected on grounds of symmetry, for a swimmer which is self T-dual.

6.5 Three collinear swimmers

We have demonstrated that hydrodynamic phase locking is possible for two collinear swimmers. We now investigate the behaviour of three swimmers, again moving in one dimension. Consider three collinear, extensile swimmers, initially with spacing 2.5ℓ, and all initially with $\phi = 0$. Fig. 6.5 shows the phases of the middle and rear swimmer when the lead swimmer reaches the beginning of its cycle as a function of the number of swimmer cycles. It is apparent from this figure that there is no simple phase locking. Early in the simulation, the phases of swimmers 2 and 3 relative to that of swimmer 1 do not tend to a fixed point as for the two-swimmer case, but vary periodically. As the simulation proceeds, the hydrodynamic interaction between the swimmers acts to change their relative positions. Swimmers 1 and 2 remain at a similar spacing, and swimmer 3 drifts away as shown in Fig. 6.5b. The stronger interaction between swimmers 1 and 2 constrains their relative phase to be close to π, but with a small oscillation imposed by the third swimmer, as its phase decreases at an approximately constant rate.

For comparison we present, in Fig. 6.5c, similar results for the relative positions of constant velocity swimmers which remain in phase. There is the same tendency for one of the swimmers to drift away from the other two. At the longest time this swimmer is still moving away, whereas for the constant force case, its position has been stabilized by the changing relative phase.

Figure 6.5: Time evolution of the relative phase of three collinear swimmers. (a) Relative phase of the middle and rear swimmers at the beginning of the front swimmer's cycle. (b) Displacements of the middle and rear swimmers from the front swimmer in a constant force swimmer simulation. (c) Displacements of the middle and rear swimmers from the front swimmer in a constant velocity swimmer simulation.

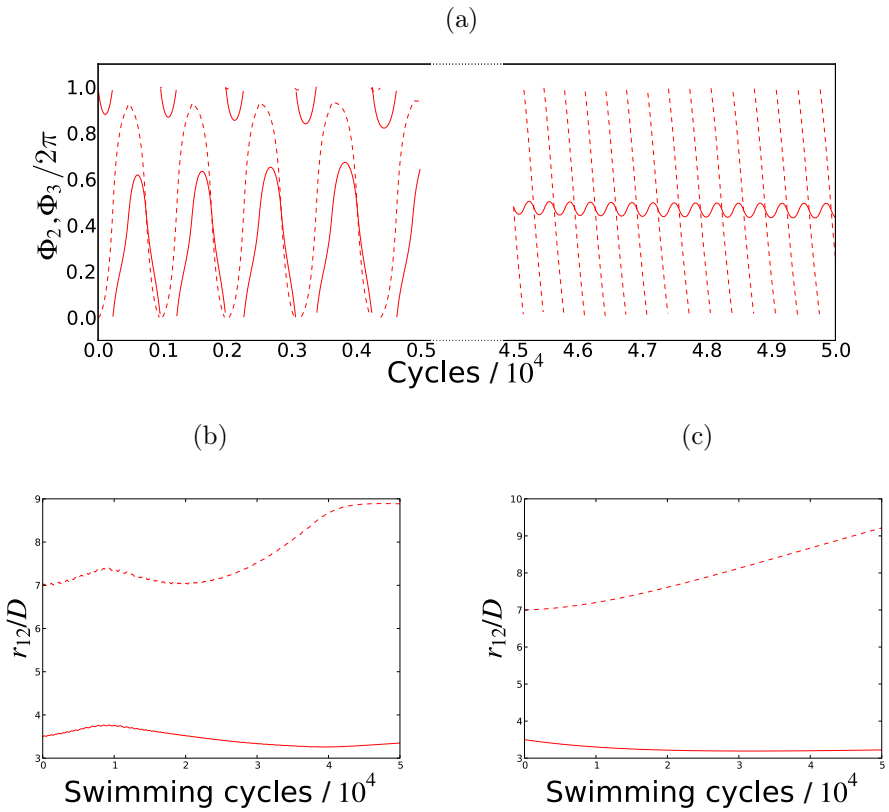

6.6 Tethered collinear swimmers

Swimmers which are constrained to remain in a fixed position become pumps that drive a net flow field. The flow field and hydrodynamic interactions will be changed by the constraint; in particular the far flow field will, in general, decay as r^{-1} due to the force holding the swimmer in position. The locking is likely to be simpler, as the distance between the pumps, and hence the strength of the hydrodynamic interactions between them, will remain constant.

To investigate this we considered collinear swimmers, fixed in space by applying a holonomic constraint that their centre of mass could not move. This resulted in a relatively small external force ($\sim 10^{-3}$ of the magnitude of the internal forces of the swimmer) applied to each sphere at each time step of the simulation.

The evolution of the relative phases of the pumps with time is shown in Fig. 6.6. Two extensile pumps phase-lock with a phase difference of π, as for the free swimmers. Three or four equispaced pumps show stable oscillations in their relative phases. These are reminiscent of the metachronal waves observed in arrays of cilia [114, 112, 113, 115].

6.7 Two dimensions

The phase-locking behaviour of two swimmers is considerably more complex when they are not collinear. To investigate this we ran simulations with two extensile swimmers, initially parallel, for different distances apart and for different angles θ between the swimmer orientation and the vector joining their centres. For each position, we ran the swimmers through one cycle at relative phases from 0 to 2π to produce phase-change curves analogous to those in Fig. 6.3. Examples are shown in Fig. 6.7, together with a central panel summarising the locking behaviour as a function of swimmer spacing and θ.

Figure 6.6: Time evolution of the relative phases of collinear pumps with time (a) Two, (b) three, (c) four swimmers. The phases are measured at the beginning of the cycle of pump 1.

(a)

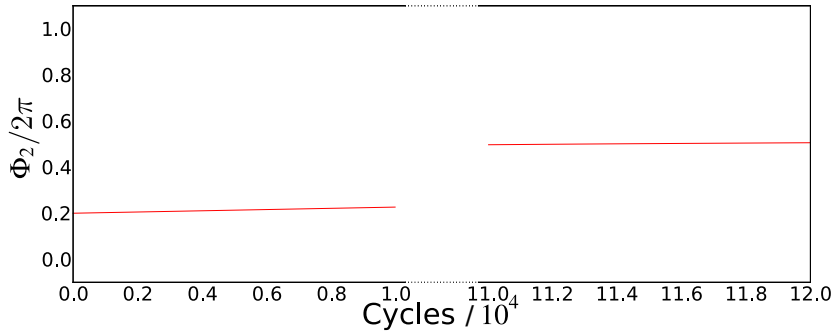

(b)

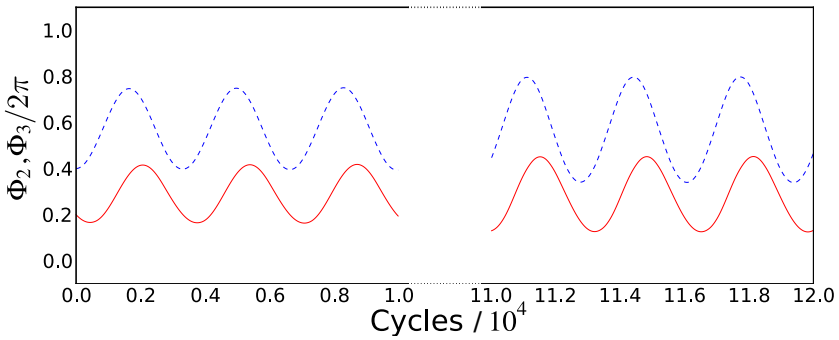

(c)

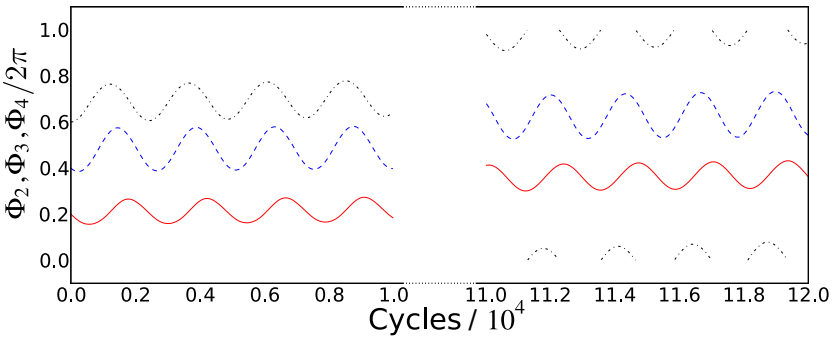

Figure 6.7: Centre: phase locking behaviour of two extensile swimmers. The swimmers are parallel and swimmer 1 is at the origin. The axes of the plot in the centre are labelled in units of ℓ. When swimmer 2 lies in the grey areas, the swimmers synchronise out-of-phase ($\phi = \pi$). When swimmer 2 lies in the black areas, the swimmers synchronise in-phase ($\phi = 0$). The white areas represent regions with two or more stable zeros. Sides: phase change curves corresponding to swimmer configurations $A, B \ldots H$. In each case the change of phase of swimmer 2 per cycle is plotted as a function of the phase of swimmer 2 measured at the beginning of the stroke of swimmer 1.

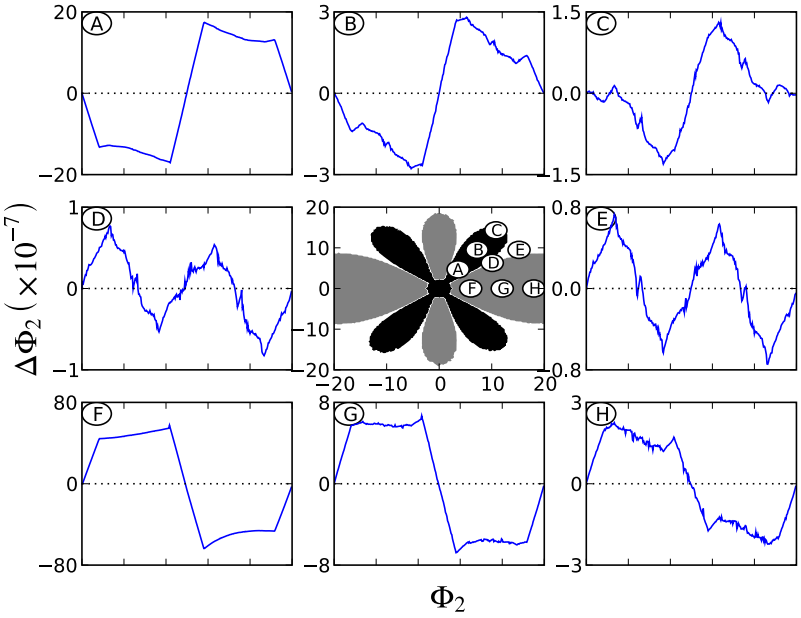

As θ varies, the phase change curves change dramatically. Consider first increasing θ along the arc GDB in Fig. 6.7. At G ($\theta = 0$), there is lock-in to a phase difference $\phi = \pi$, corresponding to the the swimmers oscillating in antiphase. As θ increases, the fixed point loses its stability via a bifurcation and two new stable fixed points appear (D). These move apart and annihilate, such that stability is transferred to the fixed point at $\phi = 0$, and the swimmers synchronise in phase (B).

This interchange of stability occurs several times as θ varies, giving regions of lock-in which are alternately in-phase and out-of-phase. The pattern reflects the dipolar symmetry of the hydrodynamic interactions.

As the swimmers move further apart, remaining parallel but at the same angle θ (e.g. FGH in Fig. 6.7), the curves retain approximately the same shape but the change in phase per cycle is smaller, reflecting the weakening interactions. Beyond the shaded regions two or more lock points are seen but it is difficult to distinguish locking from numerical noise.

6.8 Discussion

The extension of the simple linear three-sphere swimmer model into a constrained-dynamics framework is very promising. For purposes of this portion of the study, it allows the model to experience hydrodynamic synchronisation between swimmers, and allows for arbitrary holonomic constraints to be added such as those fixing the centres of mass for the discussion of tethered swimmers. Much as this constrained dynamics approach has proven fruitful for modern robotics, we feel it has potential use in the creation and analysis of arbitrary swimmer models.

The lock-in these swimmers experience is to a phase difference of ~ 0 or $\sim \pi$, depending on relative positions and flow field; superficially, this looks similar to a Kuramoto synchronisation model where $\frac{\partial \theta_i}{\partial t} = \omega_i + \frac{K}{N} \sum_{j=1}^{N} \sin(\theta_j - \theta_i)$ for a collection

of N limit-cycle oscillators. However, while this is a reasonable fit for two swimmers, the behaviour of multiple swimmers (or for two swimmers in varied positions in higher dimensions) is more complex. The locking in any case is very slow for these swimmers, taking place over tens or hundreds of swimmer cycles and becoming slower with increasing separation.

A similar synchronisation is seen for tethered swimmers (pumps) although the behaviour is simpler as the relative positions of the pumps do not vary. Two collinear pumps lock to a phase difference of 0 or π for contractile or extensile flows respectively; three or four reach a limit cycle with relative phases oscillating in a way reminiscent of cilia.

We note that self T-dual swimmers and pumps (such as the three-sphere swimmer with equal arm lengths) are forbidden by symmetry from phase locking. This agrees with the result of Kim and Powers [119] who showed that two rigid helices with parallel axes, driven by the same torque, do not synchronise.

Though in this chapter we have focussed on simple model swimmers, synchronisation has been also been predicted for arrays of rotors on a substrate [117], and observed for physical swimmers such as spermatazoa [48, 91] and pairs of beating eukaryotic flagella [110]. Similarly, the complex phase-locking observed in our multi-swimmer simulations is suggestive of metachronal waves, well established in ciliary dynamics, and thought to be stabilised by hydrodynamic interactions [112, 113, 120, 115]. To model the biological systems more closely, a model would have to include, for example, noise and variable cycle times as well as more complex swimmer geometry and motions. We note, however, that recent experiments on isolated colloidal spheres in optical traps [54] have recently shown antiphase synchronisation between two hydrodynamic oscillators which can be lost through the introduction of noise or detuning of the oscillators, an encouraging finding.

Chapter 7

Conclusions

We have studied the collective behaviour of model microswimmers at the level of pair interactions using a two-sphere colloidal swimmer model. In Chapters 2 and 3, we examined one of the simplest collective microswimmers, a purely reciprocal dumbbell made of two spheres. In isolation, such a dumbbell cannot move, but by examining pair interactions using an expansion of the Oseen tensor, we revealed contributions which could both translate and rotate dumbbells in a suspension, and confirmed our time-averaged analytics through high-speed microscopic time-resolved CUDA simulations. In all cases, from two-dumbbell test cases to suspensions of hundreds of dumbbells, we found very good agreement between our analytics and simulations. The introduction of asymmetry, by making the two spheres of different radii, was enough to dramatically change the nature of the interactions by reducing the order of the interaction scaling with distance. Generalizing recent work by Alexander and Lauga [58, 57], we have derived 3D interactions of asymmetric dumbbells and performed extensive confirmation with independent numeric simulation.

In Chapter 4, we introduced self-motility by allowing the dumbbells' spheres to cyclically vary their radii, leading to an abstract phased dipolar swimmer model, a good mix of flexibility and simplicity. Breaking the internal symmetry of the swimmer

not only decreases the order of the interaction strength with distance, but also makes the interactions passive (relying on net flow) rather than active (relying on a phase difference between swimmers) given appropriate choice of parameters. The phased dipolar swimmer also has much more configurability in that a single model can be used to study both self-motile behaviours as well as those resulting from active nematic particles which are not motile but can generate flow. With a look to the future, this opens a door to explore, by means of a microswimming model, such topics as the defect propagation predicted by Edwards [121].

Because it achieves self-swimming with only two particles, the phased dipolar swimmer is relatively easy and computationally inexpensive to model microscopically. Significantly, the interactions produced are passive at even moderate flow rates, making interswimmer phase differences negligible. Due to the underlying approximations, this model is valid in in regimes where the details of changing resistance and their higher-order flow are not significant (i.e., swimmers tuned for high flow rates and separated enough that the effects of near-field flow can be neglected). Despite its simplicity, it is useful for analysis and simulation, and is the abstract basis for a number of swimming models already studied, such as the three-sphere swimmer [35], pushmepullyou [36], or three-sphere rower [64]. Future extensions could include fixation of one of the resistances to better resemble the biological swimmer *Chlamydomonas reinhardtii*. In a recent talk, Gollub [122] displayed fully time-resolved measurements of the velocity field of individual *C. reinhardtii* with the comment that the velocity field resembled flow from three Stokeselets. This shares features with a phased dipolar swimmer with one resistance (the body) fixed and the other (the flagella) modeled as an oscillating dumbbell oriented transverse to the axis of propulsion.

In Chapter 5 we examined the motion of a tracer particle in the net flow fields of both the phased dipolar swimmer and the classic three-sphere swimmer [35]. The observed loop-shaped tracer trajectories are an interesting consequence of the force-

free swimmer condition and are a first step toward examining quantitatively the anomalous diffusion of tracers in suspensions of swimmers recently observed by Leptos et al. [107]. In examining motions of tracer particles in a suspension of *C. reinhardtii* algae, these authors noticed exponential tails on probability distributions of tracer displacements well beyond usual Gaussian white-noise predictions, requiring extension of existing diffusion theory.

While the time-averaging procedure used in Chapters 2-4 leads to analytical descriptions of simple models, the constraint-force approach employed in Chapter 6 and commonly used in robotics may provide insights into more complex models. The hydrodynamic synchronisation predicted in Chapter 6 is very similar to that seen in other studies of hydrodynamic oscillators [54, 114, 117, 115] and may help to describe the formation and propagation of metachronal waves in cilia, of interest in the creation of artificial microswimmers or microfluidic channels lined with artificial micropumps.

The microscopic time-resolved simulations developed during our research employed CUDA, a technology allowing consumer-level graphics processors to accelerate computations several hundred times. The impact of high-speed parallel simulations running at this speed on inexpensive hardware cannot be underestimated. A new standard, OpenCL, is already seeing some use and the field is progressing rapidly. GPU technology is an ideal tool for speeding up simulations of colloidal microswimmers to a high degree, and is already seeing fruitful use in Lattice-Boltzmann simulations [73]. Having this computational power available at an individual researcher's workstation rather than in a batch-oriented cluster allows rapid iteration in the software development lifecycle, leading to faster results and higher-quality simulations. We look forward to the opportunities these tools present in exploring the future of low Reynolds number hydrodynamics.

Appendix A

Expansions of the Oseen tensor

We present here the first four terms of the expansion of the Oseen tensor along two perturbations at the end of a large displacement vector. The notation here is simplified compared to that used in Chapter 2 for clarity. The results given are for the induced velocity at the target particle h from a force $F\hat{\boldsymbol{N}}$ applied at the position of the source particle n, where $\boldsymbol{D}$ is the vector from near the source to near the target, and $\boldsymbol{N}$ and $\boldsymbol{H}$ are the displacements at each end of $\boldsymbol{D}$ such that $N \ll D$, $H \ll D$, as shown in Fig. A.1

The Oseen tensor, multiplied by a force along the source particle orientation vector $\hat{\boldsymbol{N}}$ (2.11), is repeated here in this simpler notation:

Figure A.1: Geometry of the expansion of the oseen tensor about two small perturbations. The force applied is always aligned with the orientation vector of the source particle, $\hat{\boldsymbol{N}}$.

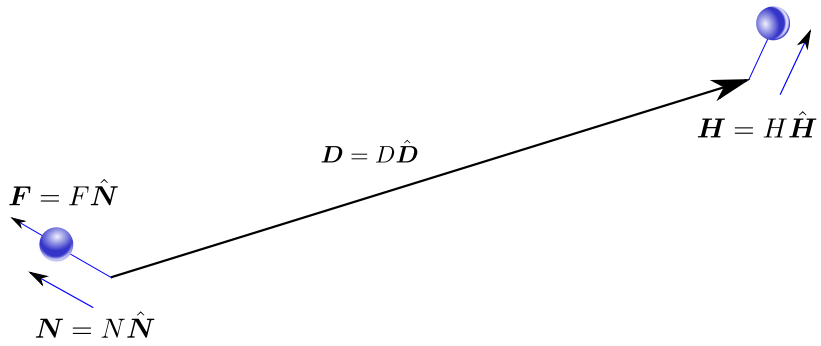

$$\begin{aligned}\boldsymbol{u}^h &= \frac{F}{8\pi\mu}\Big(\hat{\boldsymbol{N}}\left(R^2-3rNR+2sHR+2N^2-3qHN+H^2\right)\\ &\quad +\hat{\boldsymbol{R}}R(rR-N+qH)+\hat{\boldsymbol{H}}H\left(rR-N+qH\right)\Big)\\ &\quad /\left(R^2-2rNR+2sHR+N^2-2qHN+H^2\right)^{3/2},\end{aligned} \tag{A.1}$$

where r, q, s are the projections

$$\hat{\boldsymbol{N}}\hat{\boldsymbol{D}}=r,\ \hat{\boldsymbol{H}}\hat{\boldsymbol{D}}=s,\ \hat{\boldsymbol{N}}\hat{\boldsymbol{H}}=q, \tag{A.2}$$

as in (2.10). We perform a Taylor expansion about the points $N=0, H=0$ to increasing order α

A.1 $\alpha = 0\ (R^{-1})$

$$\boldsymbol{u}^h_{\alpha=0}=\frac{F}{8\pi\mu D}\left(\hat{\boldsymbol{D}}r+\hat{\boldsymbol{N}}\right). \tag{A.3}$$

A.2 $\alpha = 1\ (R^{-2})$

$$\boldsymbol{u}^h_{\alpha=1}=\frac{F}{8\pi\mu D^2}\left(\hat{\boldsymbol{D}}\left(3r^2N-N-3rsH+qH\right)-\hat{\boldsymbol{N}}sH+\hat{\boldsymbol{H}}rH\right). \tag{A.4}$$

A.3 $\alpha = 2\ (R^{-3})$

$$\begin{aligned}\boldsymbol{u}^h_{\alpha=2} = \tfrac{F}{16\pi\mu D^3}\ &\Big\{3\hat{\boldsymbol{D}}\big(5r^3N^2-3rN^2-10r^2sHN+2sHN+4qrHN\\ &\quad +5rs^2H^2-2qSH^2-rH^2\big)\\ &\quad -\hat{\boldsymbol{N}}\left(3r^2N^2-N^2-3s^2H^2+H^2\right)\\ &\quad +2\hat{\boldsymbol{H}}H\left(3r^2N-N-3rsH+qH\right)\Big\}.\end{aligned} \tag{A.5}$$

A.4 $\alpha = 3$ (R^{-4})

$$
\begin{aligned}
\boldsymbol{u}^h_{\alpha=3} = \ \tfrac{F}{16\pi\mu D^4}\Bigg\{ \hat{\boldsymbol{D}}\Big(& \left(35r^4 - 30r^2 + 3\right) N^3 \\
& -3\left(35r^3 s - 15rs - 15qr^2 + 3q\right) HN^2 \\
& +3\left(35r^2 s^2 - 5s^2 - 20qrs - 5r^2 + 2q^2 + 1\right) H^2 N \\
& -\left(35rs^3 - 15qs^2 - 15rs + 3q\right) H^3 \Big) \\
+\hat{\boldsymbol{N}}\Big(& -2r\left(5r^2 - 3\right) N^3 \\
& +3\left(5r^2 s - s - 2qr\right) HN^2 \\
& -s\left(5s^2 - 3\right) H^3 \Big) \\
+\hat{\boldsymbol{H}}\Big(& 3r\left(5r^2 - 3\right) HN^2 \\
& -6\left(5r^2 s - s - 2qr\right) H^2 N \\
& +3\left(5rs^2 - 2qs - r\right) H^3 \Big) \Bigg\}. \qquad \text{(A.6)}
\end{aligned}
$$

As can be seen, the structure and size of the expressions increases dramatically at higher order. When resolving interactions between dumbbells, H, N, and F are replaced with time-resolved expressions for each of the four bead-bead interactions. The resulting expressions are quite cumbersome, necessitating the use of expansions in powers of small parameters to make the results tractable.

Appendix B

Derivation of the translation pair interactions of symmetric dumbbells

We derive the translation portion of the pair interactions of symmetric dumbbells using the same simplified notation as in Appendix A. This is done by examining the effects of a pair of spheres at $\pm N\hat{\boldsymbol{N}}$ with respective applied forces $\mp F\hat{\boldsymbol{N}}$ at the locations of target spheres $\pm H\hat{\boldsymbol{H}}$, as shown in Fig. B.1. The deviations about the centre points are simply half the dumbbell lengths, $N = L_N/2$, $H = L_H/2$, where the lengths fluctuate as

$$L_{N,H} \;=\; L + \xi \sin\left(\omega t + \phi_{N,H}\right). \tag{B.1}$$

The symmetry involved allows many of the low-order terms in the expansion of the Oseen tensor from Appendix A to cancel, so we shall defer time-resolved substitutions until necessary for the integration stages of each step.

Figure B.1: Geometry of the symmetric dumbbell problem; the symmetry will cause many of the low-order terms in the expanded Oseen tensor from Appendix A to cancel.

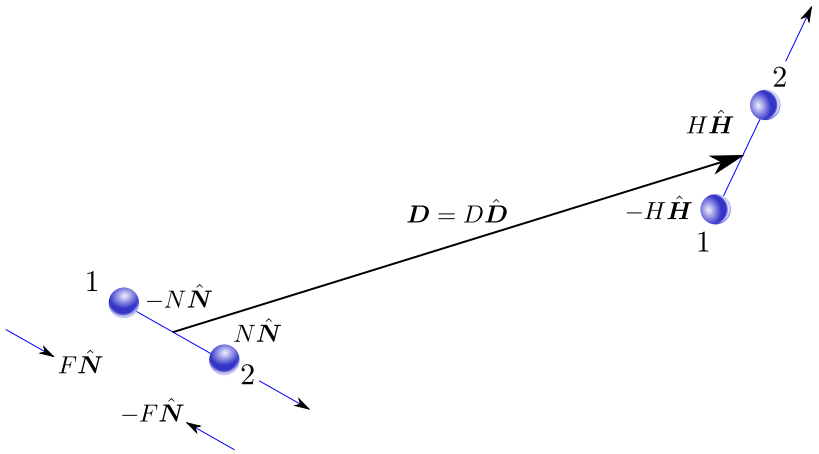

B.1 Translation

The translation of the geometric center of the target dumbbell h from the flow produced by source dumbbell n is given by

$$\frac{\mathrm{d}}{\mathrm{dt}}\boldsymbol{R}_{\mathrm{G}}^{h} = \frac{\frac{\mathrm{d}}{\mathrm{dt}}\boldsymbol{X}_{1}^{h} + \frac{\mathrm{d}}{\mathrm{dt}}\boldsymbol{X}_{2}^{h}}{2}. \tag{B.2}$$

We shall introduce the notation $\boldsymbol{u}_{\alpha}\left(F, N, H\right)$ to denote the velocity of fluid flow produced by a force $F\hat{\boldsymbol{N}}$, applied at the displacement $N\hat{\boldsymbol{N}}$ from the geometric centre of the source dumbbell, at the displacement $H\hat{\boldsymbol{H}}$ of the target dumbbell, corresponding to the expansions $\alpha = 0, 1, 2...$ given in Appendix A. This means that the ends of the target dumbbell move as

$$\frac{\mathrm{d}}{\mathrm{dt}}\boldsymbol{X}_{1}^{h} = \sum_{\alpha}\left(\boldsymbol{u}_{\alpha}\left(F, -N, -H\right) + \boldsymbol{u}_{\alpha}\left(-F, N, H\right)\right), \tag{B.3a}$$

$$\frac{\mathrm{d}}{\mathrm{dt}}\boldsymbol{X}_{2}^{h} = \sum_{\alpha}\left(\boldsymbol{u}_{\alpha}\left(F, -N, H\right) + \boldsymbol{u}_{\alpha}\left(-F, N, -H\right)\right). \tag{B.3b}$$

Combining Eqns. (B.3) and (B.2), we find the motion of the geometric centre to be

$$\begin{aligned}\frac{\mathrm{d}}{\mathrm{dt}}\boldsymbol{R}_{\mathrm{G}}^{h} &= \sum_{\alpha}\frac{\mathrm{d}}{\mathrm{dt}}\boldsymbol{R}_{\mathrm{G}}^{h,\alpha} \\ &= \frac{1}{2}\sum_{\alpha}\Big(\boldsymbol{u}_{\alpha}\left(F,-N,H\right)+\boldsymbol{u}_{\alpha}\left(F,-N,-H\right) \\ &\qquad +\boldsymbol{u}_{\alpha}\left(-F,N,H\right)+\boldsymbol{u}_{\alpha}\left(-F,N,-H\right)\Big). \end{aligned} \tag{B.4}$$

We shall now take each term $\alpha = 0, 1, 2...$ in the expansion, substitute appropriate values, cancel, and time-average.

B.1.1 $\alpha = 0$

The $\alpha = 0$ term (A.3) represents a $1/D$ Oseen interaction and does not involve the small displacements N, H at all. As a result the remaining terms, involving force only, cancel and the result is

$$\frac{\mathrm{d}}{\mathrm{dt}}\boldsymbol{R}_{\mathrm{G}}^{h,\alpha=0} = 0. \tag{B.5}$$

B.1.2 $\alpha = 1$

Here, the symmetric H terms cancel, giving what initially appears to be a dipolar flow

$$\frac{\mathrm{d}}{\mathrm{dt}}\boldsymbol{R}_{\mathrm{G}}^{h,\alpha=1} = -\frac{FN}{4\pi\mu D^{2}}\hat{\boldsymbol{D}}\left(3r^{2}-1\right). \tag{B.6}$$

This is the formula for a stresslet, the instantaneous dipolar flow at the geometric centre of the target dumbbell. However, it should time-average to zero, since reciprocal dumbbells generate no net flow. Substituting in time-varying values for F (2.8)

and N, we find

$$\begin{aligned}\frac{\mathrm{d}}{\mathrm{dt}}\boldsymbol{R}_{\mathrm{G}}^{h,\alpha=1} &= \frac{1}{4\pi\mu D^2}\hat{\boldsymbol{D}}\left(3r^2-1\right) \\ &\times\left\{\frac{6\pi a\mu\omega\cos\left(\phi_N+\omega t\right)\xi\left(\sin\left(\omega t+\phi_N\right)\xi+L\right)^2}{2\sin\left(\omega t+\phi_N\right)\xi+2L-3a}\right\}. \qquad \text{(B.7)}\end{aligned}$$

This quantity is difficult to integrate as it stands, but to order 2 in powers of ξ/L it becomes

$$\begin{aligned}\frac{\mathrm{d}}{\mathrm{dt}}\boldsymbol{R}_{\mathrm{G}}^{h,\alpha=1} &= \frac{3a\omega\xi}{4D^2\left(2L-3a\right)^2}\hat{\boldsymbol{D}}\left(3r^2-1\right)L\cos\left(\omega t+\phi_N\right) \qquad \text{(B.8)} \\ &\times\left(2\xi\left(L-3a\right)\sin\left(\omega t+\phi_N\right)+2L^2-3aL\right), \qquad \text{(B.9)}\end{aligned}$$

which integrates to zero as expected, thus

$$\frac{\mathrm{d}}{\mathrm{dt}}\boldsymbol{R}_{\mathrm{G}}^{h,\alpha=1}=0. \qquad \text{(B.10)}$$

B.1.3 $\alpha = 2$

For $\alpha = 2$, the symmetry of the terms in (A.5) cancel entirely, and the result is

$$\frac{\mathrm{d}}{\mathrm{dt}}\boldsymbol{R}_{\mathrm{G}}^{h,\alpha=2}=0. \qquad \text{(B.11)}$$

B.1.4 $\alpha = 3$

The terms which survive are

$$\begin{aligned}\frac{\mathrm{d}}{\mathrm{dt}}\boldsymbol{R}_{\mathrm{G}}^{h,\alpha=3} &= -\frac{1}{8\pi\mu D^4}\times \\ &\left\{FN^3\left(\hat{\boldsymbol{D}}\left(35r^4-30r^2+3\right)-2\hat{\boldsymbol{N}}r\left(5r^2-3\right)\right)\right. \\ &+FNH^2\Bigg(3\hat{\boldsymbol{D}}\left(35r^2s^2-5s^2-20qrs-5r^2+2q^2+1\right) \\ &\left.\left.-6\hat{\boldsymbol{H}}\left(5r^2s-s-2qr\right)\right)\right\}, \end{aligned} \tag{B.12}$$

which is cumbersome to manage. It now becomes easier to look at the integrals of the time-varying quantities FN^3 and FH^2.

B.1.4.1 FN^3

Expanded, this becomes

$$FN^3 = -\frac{3\pi a\mu\omega\xi\cos\left(\omega t+\phi_N\right)\left(\xi\sin\left(\omega t+\phi_N\right)+L\right)^4}{4\left(2\xi\sin\left(\omega t+\phi_N\right)+2L-3a\right)}, \tag{B.13}$$

which is difficult to integrate. Discarding terms of order $(\xi/L)^3$ and higher, this simplifies to

$$\begin{aligned} FN^3 &= -\frac{3\pi a\mu\omega L^3\xi\cos\left(\omega t+\phi_N\right)}{4\left(2L-3a\right)^2} && \text{(B.14)} \\ &\quad\times\left(6\xi\left(L-2a\right)\sin\left(\omega t+\phi_N\right)+2L^2-3aL\right), && \text{(B.15)} \end{aligned}$$

which integrates to zero. Thus

$$FN^3_{ave} = 0. \tag{B.16}$$

B.1.4.2 FNH^2

Expanded, this becomes

$$FH^2 = -\frac{3\pi a\mu\omega\xi\cos\left(\omega t+\phi_N\right)\left(L+\xi\sin\left(\omega t+\phi_H\right)\right)^2\left(L+\xi\sin\left(\omega t+\phi_N\right)\right)^2}{4\left(2\xi\sin\left(\omega t+\phi_N\right)+2L-3a\right)}, \tag{B.17}$$

which to order $(\xi/L)^2$ and leading order in a/L is

$$FH^2 = -\frac{3\pi a\mu\omega L^2\xi\cos\left(\omega t+\phi_N\right)\left(\xi\left(\sin\left(\omega t+\phi_N\right)+2\sin\left(\omega t+\phi_H\right)\right)+L\right)}{8}. \tag{B.18}$$

Time-averaged over a period, this becomes

$$FH^2_{ave} = \frac{3\pi a\mu\omega L^2\xi^2\sin\left(\phi_N-\phi_H\right)}{8}. \tag{B.19}$$

B.1.4.3 Final $\alpha = 3$ term

Substituting (B.16) and (B.19) into (B.12), we find

$$\begin{aligned}\frac{\mathrm{d}}{\mathrm{dt}}\boldsymbol{R}_{\mathrm{G}}^{h,\alpha=3} &= \frac{9a\omega L^2\xi^2}{64D^4}\times \\ &\quad\Big\{\hat{\boldsymbol{D}}\left(35r^2s^2-5s^2-20qrs-5r^2+2q^2+1\right) \\ &\quad -2\hat{\boldsymbol{H}}\left(5r^2s-s-2qr\right)\Big\},\end{aligned} \tag{B.20}$$

which is the quantity that appears as (2.16).

This process, involving a great many simplifications and substitutions, is best done with a computer algebra system (CAS) to minimize human error in the repetitive integrations. For this thesis this was accomplished using the open-source CAS Maxima.

Appendix C

Resistance of a varying dumbbell

Two collinear spheres of radius a separated by a distance L and subject to forces along the line between them move as

$$\frac{\mathrm{d}}{\mathrm{dt}}x_{1,2} \quad = \quad \frac{F_{2,1}}{4\pi\mu L} + \frac{F_{1,2}}{6\pi a\mu}. \tag{C.1}$$

If the link between the two spheres forces them to move at the same rate, then if a force F is applied to one end, $F_1 = F_2 = F/2$, and the dumbbell moves as

$$\frac{\mathrm{d}}{\mathrm{dt}}x = F\frac{2L+3a}{24\pi a\mu L}, \tag{C.2}$$

giving it a hydrodynamic resistance of

$$R = \frac{24\pi a\mu L}{2L+3a}. \tag{C.3}$$

If the length L is allowed to vary as $L(t) = \ell + \xi\sin(\omega t + \phi)$, Eqn. (C.3) becomes a time-varying resistance. To leading order in ξ/ℓ, we find

$$R(t) = R_0 + \lambda\sin(\omega t + \phi), \tag{C.4}$$

where

$$\begin{aligned} R_0 &= \frac{24\pi a\mu L}{2L+3a}, \\ \lambda &= \frac{72\pi a^2\mu\xi}{(2L+3a)^2}. \end{aligned} \tag{C.5}$$

The quantities R_0 and λ from (C.5), divided by $6\pi\mu$, can be used as an effective radius and variation for spheres in analytics and simulation of colloids to approximate the hydrodynamic resistance of a dumbbell along its length.

Bibliography

[1] J. Toner, Y. Tu, and S. Ramaswamy. Hydrodynamics and phases of flocks. *Ann. Phys.*, 318(1):170–244, 2005.

[2] W. K. Potts. The chorus-line hypothesis of manoeuvre coordination in avian flocks. *Nature*, 309(5966):344–345, 1984.

[3] C. W. Reynolds. Flocks, herds and schools: A distributed behavioral model. *SIGGRAPH Comput. Graph.*, 21(4):25–34, 1987.

[4] T. Vicsek, A. Czirók, E. Ben-Jacob, I. Cohen, and O. Shochet. Novel type of phase transition in a system of self-driven particles. *Phys. Rev. Lett.*, 75(6):1226–1229, 1995.

[5] M. F. Copeland and D. B. Weibel. Bacterial swarming: a model system for studying dynamic self-assembly. *Soft Matter*, 5(6):1174–1187, 2009.

[6] C. Dombrowski, L. Cisneros, S. Chatkaew, R. E. Goldstein, and J. O. Kessler. Self-concentration and large-scale coherence in bacterial dynamics. *Phys. Rev. Lett.*, 93(9):098103, 2004.

[7] F. Ginelli, F. Peruani, M. Bär, and H. Chaté. Large-scale collective properties of self-propelled rods. *Phys. Rev. Lett.*, 104(18):184502, 2010.

[8] R. A. Simha and S. Ramaswamy. Hydrodynamic fluctuations and instabilities in

ordered suspensions of self-propelled particles. *Phys. Rev. Lett.*, 89(5):058101, 2002.

[9] D. C. Guell, H. Brenner, R. B. Frankel, and H. Hartman. Hydrodynamic forces and band formation in swimming magnetotactic bacteria. *J. Theor. Biol*, 135(4):525–542, 1988.

[10] M. J. Carlile and A. W. L. Dudeney. Zonation in migrating magnetococci. *J. Gen. Microbiol*, 139(9):1671–1680, 1993.

[11] I. H. Riedel, K. Kruse, and J. Howard. A self-organized vortex array of hydrodynamically entrained sperm cells. *Science*, 309(5732):300–303, 2005.

[12] T. J. Pedley, N. A. Hill, and J. O. Kessler. The growth of bioconvection patterns in a uniform suspension of gyrotactic micro-organisms. *J. Fluid Mech.*, 195:223–237, 1988.

[13] S. Ghorai and N. A. Hill. Development and stability of gyrotactic plumes in bioconvection. *J. Fluid Mech.*, 400:1–31, 1999.

[14] W. R. DiLuzio, L. Turner, M. Mayer, P. Garstecki, D. B. Weibel, H. C. Berg, and G. M. Whitesides. Escherichia coli swim on the right-hand side. *Nature*, 435(7046):1271–1274, 2005.

[15] K. Drescher, K. C. Leptos, I. Tuval, T. Ishikawa, T. J. Pedley, and R. E. Goldstein. Dancing Volvox: hydrodynamic bound states of swimming algae. *Phys. Rev. Lett.*, 102(16):168101, 2009.

[16] E. Lauga, W. Diluzio, G. Whitesides, and H. Stone. Swimming in circles: motion of bacteria near solid boundaries. *Biophys. J.*, 90(2):400–412, 2006.

[17] T. Feder. Statistical physics is for the birds. *Phys. Today*, 60(10):28–30, 2007.

[18] H. C. Berg. Motile behavior of bacteria. *Phys. Today*, 53(1):24–29, 2000.

[19] E. O. Budrene and H. C. Berg. Complex patterns formed by motile cells of escherichia coli. *Nature*, 349(6310):630–633, 1991.

[20] E. O. Budrene and H. C. Berg. Dynamics of formation of symmetrical patterns by chemotactic bacteria. *Nature*, 376(6535):49–53, 1995.

[21] E. M. Purcell. Life at low Reynolds number. *Am. J. Phys.*, 45(1):3–11, 1977.

[22] A. Shapere and F. Wilczek. Efficiencies of Self-Propulsion at low Reynolds number. *J. Fluid Mech.*, 198:587–599, 1989.

[23] A. Shapere and F. Wilczek. Geometry of Self-Propulsion at low Reynolds number. *J. Fluid Mech.*, 198:557–585, 1989.

[24] A. Shapere and F. Wilczek. Self-Propulsion at low Reynolds number. *Phys. Rev. Lett.*, 58(20):2051–2054, 1987.

[25] M. Doi and S. F. Edwards. *The theory of polymer dynamics*. Clarendon press, Oxford, 1986.

[26] J. Rotne and S. Prager. Variational treatment of hydrodynamic interaction in polymers. *J. Chem. Phys.*, 50(11):4831–4837, 1969.

[27] H. Yamakawa. Transport properties of polymer chains in dilute solution: hydrodynamic interaction. *J. Chem. Phys.*, 53(1):436–443, 1970.

[28] P. Mazur and W. van Saarloos. Many-sphere hydrodynamic interactions and mobilities in a suspension. *Phys. A*, 115(1-2):21–57, 1982.

[29] Y. Hatwalne, S. Ramaswamy, M. Rao, and R. A. Simha. Rheology of active-particle suspensions. *Phys. Rev. Lett.*, 92(11):118101, 2004.

[30] J. P. Hernandez-Ortiz, C. G. Stoltz, and M. D. Graham. Transport and collective dynamics in suspensions of confined swimming particles. *Phys. Rev. Lett.*, 95(20):204501, 2005.

[31] T. J. Pedley and J. O. Kessler. Hydrodynamic phenomena in suspensions of swimming microorganisms. *Annu. Rev. Fluid. Mech.*, 24(1):313–358, 1992.

[32] G. K. Batchelor. The stress system in a suspension of force-free particles. *J. Fluid Mech.*, 41(03):545–570, 1970.

[33] J. G. Kirkwood and J. Riseman. The intrinsic viscosities and diffusion constants of flexible macromolecules in solution. *J. Chem. Phys.*, 16(6):565–573, 1948.

[34] J. F. Brady and G. Bossis. Stokesian dynamics. *Annu. Rev. Fluid. Mech.*, 20(1):111–157, 1988.

[35] A. Najafi and R. Golestanian. Simple swimmer at low Reynolds number: three linked spheres. *Phys. Rev. E*, 69(6):062901, 2004.

[36] J. E. Avron, O. Kenneth, and D. H. Oaknin. Pushmepullyou: an efficient micro-swimmer. *New J. Phys.*, 7:234, 2005.

[37] R. Golestanian. three-sphere low-Reynolds-number swimmer with a cargo container. *Eur. Phys. J. E*, 25(1):1–4, 2008.

[38] G. P. Alexander, C. M. Pooley, and J. M. Yeomans. Hydrodynamics of linked sphere model swimmers. *J. Phys.: Condens. Matter*, 21(20):204108, 2009.

[39] G. P. Alexander, C. M. Pooley, and J. M. Yeomans. Scattering of low-Reynolds-number swimmers. *Phys. Rev. E*, 78(4):045302, 2008.

[40] C. M. Pooley, G. P. Alexander, and J. M. Yeomans. Hydrodynamic interaction between two swimmers at low Reynolds number. *Phys. Rev. Lett.*, 99(22):228103, 2007.

[41] R. Golestanian and A. Ajdari. Analytic results for the three-sphere swimmer at low Reynolds number. *Phys. Rev. E*, 77(3):036308, 2008.

[42] F. Alouges, A. DeSimone, and A. Lefebvre. Optimal strokes for axisymmetric microswimmers. *Eur. Phys. J. E*, 28(3):279–284, 2009.

[43] T. Ishikawa, M. P. Simmonds, and T. J. Pedley. Hydrodynamic interaction of two swimming model micro-organisms. *J. Fluid Mech.*, 568:119–160, 2006.

[44] T. Ishikawa, J. T. Locsei, and T. J. Pedley. Development of coherent structures in concentrated suspensions of swimming model micro-organisms. *J. Fluid Mech.*, 615:401–431, 2008.

[45] T. Ishikawa and T. J. Pedley. The rheology of a semi-dilute suspension of swimming model micro-organisms. *J. Fluid Mech.*, 588:399–435, 2007.

[46] A. M. Leshansky, O. Kenneth, O. Gat, and J. E. Avron. A frictionless microswimmer. *New J. Phys.*, 9(5):145–145, 2007.

[47] A. A. Evans, S. E. Spagnolie, and E. Lauga. Stokesian jellyfish: viscous locomotion of bilayer vesicles. *Soft Matter*, 6:1737–1747, 2010.

[48] G. Taylor. Analysis of the swimming of microscopic organisms. *Proc. R. Soc. A*, 209(1099):447–461, 1951.

[49] J. Lighthill. Flagellar hydrodynamics: The John von Neumann Lecture, 1975. *SIAM Review*, 18(2):161–230, 1976.

[50] J. P. Hernandez-Ortiz, P. T. Underhill, and M. D. Graham. Dynamics of confined suspensions of swimming particles. *J. Phys.: Condens. Matter*, 21(20):204107, 2008.

[51] A. Baskaran and M. C. Marchetti. Statistical mechanics and hydrodynamics of bacterial suspensions. *Proc. Natl. Acad. Sci. U.S.A.*, 106(37):15567–15572, 2009.

[52] M. Leoni, J. Kotar, B. Bassetti, P. Cicuta, and M. C. Lagomarsino. A basic swimmer at low Reynolds number. *Soft Matter*, 5(2):472–476, 2009.

[53] R. Dreyfus, J. Baudry, M. L. Roper, M. Fermigier, H. A. Stone, and J. Bibette. Microscopic artificial swimmers. *Nature*, 437(7060):862–865, 2005.

[54] J. Kotar, M. Leoni, B. Bassetti, M. C. Lagomarsino, and P. Cicuta. Hydrodynamic synchronization of colloidal oscillators. *Proc. Nat. Acad. Sci.*, 107(17):7669 –7673, 2010.

[55] P. Tierno, R. Golestanian, I. Pagonabarraga, and F. Sagués. Controlled swimming in confined fluids of magnetically actuated colloidal rotors. *Phys. Rev. Lett.*, 101(21):218304, 2008.

[56] P. Tierno, R. Golestanian, I. Pagonabarraga, and F. Sagues. Magnetically actuated colloidal microswimmers. *J. Phys. Chem. B*, 112(51):16525–16528, 2008.

[57] E. Lauga and D. Bartolo. No many-scallop theorem: collective locomotion of reciprocal swimmers. *Phys. Rev. E*, 78(3):030901, 2008.

[58] G. P. Alexander and J. M. Yeomans. Dumb-bell swimmers. *Europhys. Lett.*, 83(3):34006, 2008.

[59] P. Hänggi and F. Marchesoni. Artificial Brownian motors: controlling transport on the nanoscale. *Rev. Mod. Phys.*, 81(1):387–442, 2009.

[60] T. J. Murphy. Brownian motion of N interacting particles. I. extension of the

Einstein diffusion relation to the N-particle case. *J. Chem. Phys.*, 57(5):2098, 1972.

[61] B. Dünweg and A. Ladd. Lattice Boltzmann simulations of soft matter systems. In *Advanced Computer Simulation Approaches for Soft Matter Sciences III*, pages 89–166. Springer Berlin/Heidelberg, 2009.

[62] M. Bixon. Polymer dynamics in solution. *Annu. Rev. Phys. Chem.*, 27(1):65–84, 1976.

[63] J. Dunkel and I. M. Zaid. Noisy swimming at low Reynolds numbers. *Phys. Rev. E*, 80(2):021903, 2009.

[64] D. J. Earl, C. M. Pooley, J. F. Ryder, I. Bredberg, and J. M. Yeomans. Modeling microscopic swimmers at low Reynolds number. *J. Chem. Phys.*, 126(6):064703, 2007.

[65] V. Lobaskin and B. Dünweg. A new model for simulating colloidal dynamics. *New J. Phys*, 6:54, 2004. New J. Phys. 6, 54 (2004).

[66] K. Stratford and I. Pagonabarraga. Parallel simulation of particle suspensions with the lattice Boltzmann method. *Computers & Mathematics with Applications*, 55(7):1585–1593, 2008.

[67] M. T. Downton and H. Stark. Simulation of a model microswimmer. *J. Phys.: Condens. Matter*, 21(20):204101, 2009.

[68] J. Kajtar and J. J. Monaghan. SPH simulations of swimming linked bodies. *J. Comput. Phys.*, 227(19):8568–8587, 2008.

[69] A. Sierou and J. F. Brady. Accelerated Stokesian Dynamics simulations. *Journal of Fluid Mechanics*, 448:115–146, 2001.

[70] L. Genovese, M. Ospici, T. Deutsch, J. Méhaut, A. Neelov, and S. Goedecker. Density functional theory calculation on many-cores hybrid central processing unit-graphic processing unit architectures. *J. Chem. Phys.*, 131(3):034103, 2009.

[71] T. Preis, P. Virnau, W. Paul, and J. J. Schneider. GPU accelerated Monte Carlo simulation of the 2D and 3D Ising model. *J. Comput. Phys.*, 228(12):4468–4477, 2009.

[72] A. C. Thompson, C. J. Fluke, D. G. Barnes, and B. R. Barsdell. Teraflop per second gravitational lensing ray-shooting using graphics processing units. *New Astronomy*, 15(1):16–23, 2010.

[73] M. Januszewski and M. Kostur. Accelerating numerical solution of stochastic differential equations with CUDA. *Comput. Phys. Commun.*, 181(1):183–188, 2010.

[74] D. Saintillan, E. Darve, and E. S. G. Shaqfeh. A smooth particle-mesh Ewald algorithm for Stokes suspension simulations: the sedimentation of fibers. *Phys. Fluids*, 17(3):033301–21, 2005.

[75] U. Essmann, L. Perera, M. L. Berkowitz, T. Darden, H. Lee, and L. G. Pedersen. A smooth particle mesh Ewald method. *J. Chem. Phys.*, 103(19):8577–8593, 1995.

[76] C. W. J. Beenakker. Ewald sum of the Rotne-Prager tensor. *J. Chem. Phys.*, 85:1581–1582, 1986.

[77] M. Deserno and C. Holm. How to mesh up Ewald sums. II. an accurate error estimate for the particle–particle–particle-mesh algorithm. *J. Chem. Phys.*, 109(18):7694–7701, 1998.

[78] M. Deserno and C. Holm. How to mesh up Ewald sums. I. a theoretical and numerical comparison of various particle mesh routines. *J. Chem. Phys.*, 109(18):7678–7693, 1998.

[79] H. Hasimoto. On the periodic fundamental solutions of the Stokes equations and their application to viscous flow past a cubic array of spheres. *J. Fluid Mech.*, 5(02):317–328, 2006.

[80] L. Nyland, M. Harris, and J. Prins. Fast N-Body simulation with CUDA. In *GPU Gems 3*, pages 677–696. Addison-Wesley Professional, 2007.

[81] P. Majander and Timo Siikonen. A comparison of time integration methods in an unsteady low-Reynolds-number flow. *Internat. J. Numer. Methods Engrg.*, 39(5):361–390, 2002.

[82] A. Greiner, W. Strittmatter, and J. Honerkamp. Numerical integration of stochastic differential equations. *J. Stat. Phys.*, 51(1):95–108, 1988.

[83] G. Denk and S. Schaffler. Adams methods for the efficient solution of stochastic differential equations with additive noise. *Computing*, 59(2):153–161, 1997.

[84] T. M. Han and Y. Han. Solving implicit equations arising from Adams-Moulton methods. *BIT Numerical Mathematics*, 42(2):336–350, 2002.

[85] K. Burrage and P. M. Burrage. High strong order explicit Runge-Kutta methods for stochastic ordinary differential equations. *Appl. Numer. Math.*, 22(1-3):81–101, 1996.

[86] I. T. Famelis, F. Xanthos, G. Papageorgiou, T. E. Simos, G. Psihoyios, and C. Tsitouras. Runge Kutta families for additive noise stochastic differential equations. In *AIP Conference Proceedings*, pages 182–185, Psalidi, Kos (Greece), 2008.

[87] A. Tocino and R. Ardanuy. Runge-Kutta methods for numerical solution of stochastic differential equations. *J. Comput. Appl. Math.*, 138(2):219–241, 2002.

[88] P. Wang. Three-stage stochastic Runge-Kutta methods for stochastic differential equations. *J. Comput. Appl. Math.*, 222(2):324–332, 2008.

[89] J. H. Jung. Cholesky decomposition and linear programming on a GPU. Technical report, Department of Computer Science, University of Maryland, 2006.

[90] V. Volkov and J. Demmel. LU, QR and Cholesky factorizations using vector capabilities of GPUs. Technical report, EECS Department, University of California, Berkeley, 2008.

[91] Y. Yang, J. Elgeti, and G. Gompper. Cooperation of sperm in two dimensions: synchronization, attraction, and aggregation through hydrodynamic interactions. *Phys. Rev. E*, 78(6):061903, 2008.

[92] N. A. Hill and T. J. Pedley. Bioconvection. *Fluid Dynam. Res.*, 37(1-2):1–20, 2005.

[93] H. Brenner. The Stokes resistance of an arbitrary particle. *Chem. Engr. Science*, 18:1–25, 1963.

[94] D. Tam and A. E. Hosoi. Optimal stroke patterns for Purcell's three-link swimmer. *Phys. Rev. Lett.*, 98(6):068105, 2007.

[95] L. E. Becker, S. A. Koehler, and H. A. Stone. On self-propulsion of micromachines at low Reynolds number: Purcell's three-link swimmer. *Journal of Fluid Mechanics*, 490(-1):15–35, 2003.

[96] R. Dreyfus, J. Baudry, and H. A. Stone. Purcell's rotator: mechanical rotation at low Reynolds number. *Eur. Phys. J. B*, 47(1):161–164, 2005.

[97] D. A. Fletcher and J. A. Theriot. An introduction to cell motility for the physical scientist. *Phys. Biol.*, 1(1):T1, 2004.

[98] D. L. Ringo. Flagellar motion and fine structure of the flagellar apparatus in Chlamydomonas. *J. Cell Biol.*, 33(3):543–571, 1967.

[99] R. M. Kirby, H. Marmanis, and D. H. Laidlaw. Visualizing multivalued data from 2D incompressible flows using concepts from painting. In *Proceedings of the conference on Visualization '99: celebrating ten years*, pages 333–340, San Francisco, California, United States, 1999. IEEE Computer Society Press.

[100] J. J. van Wijk. Image based flow visualization. In *Proceedings of the 29th annual conference on Computer graphics and interactive techniques*, pages 745–754, San Antonio, Texas, 2002. ACM.

[101] G. Turk and D. Banks. Image-guided streamline placement. In *Proceedings of the 23rd annual conference on Computer graphics and interactive techniques*, pages 453–460. ACM, 1996.

[102] B. Cabral and L. C. Leedom. Imaging vector fields using line integral convolution. In *Proceedings of the 20th annual conference on Computer graphics and interactive techniques*, pages 263–270, Anaheim, CA, 1993. ACM.

[103] R. S. Laramee, H. Hauser, H. Doleisch, B. Vrolijk, F. H. Post, and D. Weiskopf. The state of the art in flow visualization: dense and texture-based techniques. *Computer Graphics Forum*, 23(2):203–221, 2004.

[104] D. Laidlaw, R. M. Kirby, J. S. Davidson, T. S. Miller, M. da Silva, W. H. Warren, and M. Tarr. Quantitative comparative evaluation of 2D vector field visualization methods. In *Visualization Conference, IEEE*, Los Alamitos, CA, USA, 2001. IEEE Computer Society.

[105] A. Sokolov, I. S. Aranson, J. O. Kessler, and R. E. Goldstein. Concentration dependence of the collective dynamics of swimming bacteria. *Phys. Rev. Lett.*, 98(15):158102, 2007.

[106] Z. Gitai. New fluorescence microscopy methods for microbiology: sharper, faster, and quantitative. *Curr. Opin. Microbiol.*, 12(3):341–346, 2009.

[107] K. C. Leptos, J. S. Guasto, J. P. Gollub, A. I. Pesci, and R. E. Goldstein. Dynamics of enhanced tracer diffusion in suspensions of swimming eukaryotic microorganisms. *Phys. Rev. Lett.*, 103(19):198103, 2009.

[108] M. Polin, I. Tuval, K. Drescher, J. P. Gollub, and R. E. Goldstein. Chlamydomonas swims with two "gears" in a eukaryotic version of run-and-tumble locomotion. *Science*, 325(5939):487–490, 2009.

[109] R. Golestanian and A. Ajdari. Stochastic low Reynolds number swimmers. *J. Phys.: Condens. Matter*, 21(20):204104, 2009.

[110] R. E. Goldstein, M. Polin, and I. Tuval. Noise and synchronization in pairs of beating eukaryotic flagella. *Phys. Rev. Lett.*, 103(16):168103, 2009.

[111] K. M. Jansons and G. D. Lythe. Stochastic Stokes drift. *Phys. Rev. Lett.*, 81(15):3136, 1998.

[112] S. Gueron and K. Levit-Gurevich. Energetic considerations of ciliary beating and the advantage of metachronal coordination. *Proc. Natl. Acad. Sci. U.S.A.*, 96(22):12240–12245, 1999.

[113] S. Gueron, K. Levit-Gurevich, N. Liron, and J. J. Blum. Cilia internal mechanism and metachronal coordination as the result of hydrodynamical coupling. *Proc. Natl. Acad. Sci. U.S.A.*, 94(12):6001–6006, 1997.

[114] M. C. Lagomarsino, P. Jona, and B. Bassetti. Metachronal waves for deterministic switching two-state oscillators with hydrodynamic interaction. *Phys. Rev. E*, 68(2):021908, 2003.

[115] M. C. Lagomarsino, B. Bassetti, and P. Jona. Rowers coupled hydrodynamically. Modeling possible mechanisms for the cooperation of cilia. *Eur. Phys. J. B*, 26(1):81–88, 2002.

[116] M. Reichert and H. Stark. Synchronization of rotating helices by hydrodynamic interactions. *Eur. Phys. J. E*, 17(4):493–500, 2005.

[117] N. Uchida and R. Golestanian. Synchronization and collective dynamics in a carpet of microfluidic rotors. *Phys. Rev. Lett.*, 104(17):178103, 2010.

[118] J. Shewchuk. An introduction to the conjugate gradient method without the agonizing pain. Technical report, Carnegie Mellon University, 1994.

[119] M. Kim and T. R. Powers. Hydrodynamic interactions between rotating helices. *Phys. Rev. E*, 69(6):061910, 2004.

[120] B. Qian, H. Jiang, D. A. Gagnon, T. R. Powers, and K. S. Breuer. Minimal model for hydrodynamic synchronization. *Phys. Rev. E*, 80(6):061919, 2009.

[121] S. A. Edwards and J. M. Yeomans. Spontaneous flow states in active nematics: a unified picture. *Europhys. Lett.*, 85(1):18008, 2009.

[122] J. Gollub. Space and time-resolved studies of 2D flows induced by swimming algae. Conference talk, Individual and collective fluid mechanics of swimming microorganisms, 2010.